Quantum Turbulence Generated by Moving Grids

Lydia L.E. Munday MPhys (Hons)

Department of Physics

Lancaster University

A thesis submitted for the degree of

Doctor of Philosophy

May 2014

I would like to dedicate this thesis to my brother and sister, their belief in me has never faltered...

I would also like to dedicate this work to my Uncle, Paul Martin. Each time we spoke he always had a thought-provoking question and was my scientific inspiration, even though he was only an engineer!

Acknowledgements

I would like to, first and foremost, thank my supervisors, Professor Shaun Fisher, Professor Gary Ihas, and Professor Peter McClintock, for their invaluable expertise, guidance and encouragement. On this note I would also like to thank Professor William Vinen for his expert opinions, comments and explanations throughout my PhD studies.

I especially want to thank my lab partner for the majority of the data taking portion, Jihee Yang, who was with me for the long nights and frustrating days and yet still talks to me! I would also like to acknowledge Kyle Thompson, my predecessor; without Kyles insight and suggestions I would not have got where I am today.

I wish to thank Malcolm Poole and Mukesh Kumar who helped me obtain all of the data in my first year of study, along with assisting the steep learning curve that was my first year!

A massive thank you goes out to all of the engineers and technicians who have helped me through the past four years. In particular I would like to thank Greg Labbe, who is not only a good friend, but someone who has taught me the subtleties and 'tricks of the trade' of cryogenic engineering.

I would like to thank my friends and family, including my friends from my undergraduate as well as the ones I have made along the way. I have wanted to quit a couple of times throughout my studies, and they have always been there to push me in the right direction. My family have always been a source of inspiration and reassurance, as well as a shoulder to cry on when needed. I also want to thank my boyfriend,

for the patience to wait for me during the writing of this dissertation, and for the incentive to finish, and finish it well.

Finally I would like to acknowledge the grant which made it all possible - *Materials World Network: Collaborative research on simple forms of quantum turbulence - production, decay and visualisation; EPSRC grant number EP/H04762X/1 and NSF grant number DMR-1007937.*

Abstract

We present experimental results on quantum grid turbulence produced by moving grids within superfluid ^{4}He, both at millikelvin temperatures, with an oscillating grid, and at temperatures above 1.4 K with a linearly moving grid.

Floppy devices were used at millikelvin temperatures to produce quantum turbulence. We investigated the frequency dependence of the turbulent drag on an oscillating grid. At high velocities, the turbulent drag is independent of frequency and similar to what was measured in liquid helium-4 in its normal phase. We also present measurements of the inertial drag coefficient for grid turbulence, which is significantly reduced by turbulence produced in both superfluid and normal fluid ^{4}He.

To produce (approximate) homogeneous and isotropic grid turbulence in a quantum liquid, with little to no extraneous heating in the fluid, a new linear 'control motor' has been designed and tested. The motor consists of a drive coil, surrounded by three control coils. A linear current ramp is passed through the drive coil, which lifts a superconducting armature placed in the centre of the solenoid. The control coils are designed, when a steady DC current is applied to them, to have constant magnetic field derivative. The control motor performs adequately, having smooth motions with no oscillations, and with peak velocities up to approximately 30 cm/s. The velocity is not, however, very uniform during the motion of the motor.

Decaying turbulence is investigated using the attenuation of second sound. We produce turbulence inside a short channel totally submersed

in liquid helium-II. The turbulence is produced by a superconducting, magnetically levitated linear motor, with a grid attached to the top of the armature. The theory applied, for calculating vortex line density decay from second sound attenuation, is taken from *Stalp, S. (1998) Decay of Grid Turbulence in Superfluid Helium. Ph.D. Thesis.* We investigate the effects of different grid meshes on the vorticity decay curve, in particular the time at which the turbulence becomes saturated. We present comparisons of three separate meshes.

We observe a shorter saturation time, and therefore a longer inertial regime with a $t^{-3/2}$ dependence, for the turbulent decay produced by the smallest mesh grid. It has been suggested elsewhere that there is a $t^{-11/10}$ dependence at early times in the vorticity decay curves, we observe no such dependence. Finally, we present measurements of the effective kinematic viscosity, and saturation time and their dependence on grid mesh size.

Declaration

The work presented in this thesis was a collaborative effort between members of the Lancaster University Low Temperature group, and the University of Florida Quantum Turbulence group. This thesis has been written solely by me and has not been submitted in substantially the same form for the award of a higher degree elsewhere.

The Control Linear Motor, discussed in chapter 4, was designed in conjunction with Kyle Thompson at the University of Florida, US. The data presented in chapter 5 were recorded and analysed in close collaboration with Jihee Yang, also from the University of Florida, US; therefore, in the work following, figures which were created jointly are annotated "(LM + JY)", and figures which are presented courtesy of Jihee Yang are annotated "(JY)".

Contents

List of Figures

Chapter 1

Introduction

Turbulence is defined by the English Oxford dictionary as a "violent or unsteady movement of air or water, or of some other fluid". This statement is purposefully quite vague, as 'some other fluid' could mean anything from flowing water through a pipe to interstellar plasma (Elmegreen & Scalo [2004]) - and indeed turbulence is found in all of these cases (Sreenivasan [1999]), and yet remains an unsolved problem in classical physics. In all cases of turbulence, vortices are present and are usually the precursor. Figure 1.1 shows two common forms: turbulence from the wake of an aeroplane and turbulence surrounding a tornado (a giant vortex).

(a) Turbulence caused by an aeroplane (b) A Tornado, a natural large scale vortex

Figure 1.1: Photos depicting turbulent systems
Pictures from free internet media

The understanding of turbulence is a crucial part to our understanding of almost every fluid system, including technological applications. To understand turbulence in general, the first steps are to produce the simplest form, with known

initial conditions.

The simplest form of turbulence is one which is homogeneous and isotropic. One way to produce this relatively simple turbulence, approximately, is by having a fluid pass sufficiently fast through a grid. Grid turbulence has been studied in many different ways, and for many different applications: Mydlarski & Warhaft [1996], Couder [1984], and Roach [1986] provide a few examples. Two different types of grid motion have been investigated in this dissertation; one is an oscillating 'floppy device' which swings a grid mesh back and forth through the liquid, and the other is a linear motor which pushes and pulls a grid mesh linearly through it.

The medium on which this dissertation is focused is liquid helium, in particular superfluid liquid helium-4. When cooled below a temperature of 2.17 K, liquid helium undergoes a transition into a quantum liquid known as a superfluid. Superfluid ^{4}He has the lowest kinematic viscosity of any known substance, it can therefore produce highly turbulent flows. Turbulence produced in a superfluid is known as quantum turbulence, the vortices which comprise the turbulence are quantised, and therefore their interactions are easier to interpret than their classical counterparts. The theory of turbulence, and other relevant theory, are discussed in chapter 2.

This thesis is split into three sub-topics, research areas, representing the three, quite distinct, projects that I have been involved with. Chapter 3 discusses the use of an oscillating floppy device, which produces turbulence through a range of oscillating frequencies, as well as on resonance. Oscillating objects have been used by a number of different groups, including (but my no means limited to) Bradley *et al.* [2005], Charalambous *et al.* [2006], Luzuriaga [1997], and Nichol *et al.* [2004]. All of these have used oscillating objects driven on resonance to produce quantum turbulence. Bradley *et al.* [2011] present a new, oscillating device which includes an incorporated grid mesh to a goal-post shaped oscillating wire, as opposed to a sphere or a small vibrating wire. Chapter 3 therefore, discusses the results obtained from the use of this new device, and its corresponding position detection

technique, to investigate the dependence on oscillation frequency and amplitude.

The floppy device, however, is only approximately linear over small distances. A new linear motor was therefore designed and manufactured; this is discussed in chapter 4. There have been previous motors which have worked both at very low temperatures, for example Ihas *et al.* [2008] and Liu *et al.* [2007], and at temperatures >1 K, for example Stalp *et al.* [1999] and Niemela *et al.* [2005]. The linear motor discussed in this dissertation was designed to work at very low temperatures on the principle of superconducting magnetic levitation. The operational theory and practice, manufacturing techniques, and test results are all presented in chapter 4.

The new linear motor was then utilised for a number of turbulence experiments, described in chapter 5, in which the decay of the vortex line density was observed through the attenuation of second-sound. second-sound is a propagating entropy-temperature wave (see chapter 2), which can be produced, and detected, by two vibrating superleak transducers. The transducers are placed so to face each other across an experimental channel. The turbulence produced, from a motion of the linear motor with a grid attached, will interact with the second-sound wave, causing an attenuation in the measured signal. It is possible to calculate the vortex line density from this signal attenuation Stalp *et al.* [1999], and record the decay over time. The main goal of this set of experiments were to investigate dependency of the vorticity decay on the grid mesh size and design. Previous work carried out in this subject area, has only included the use of one grid mesh - Stalp [1998], Niemela *et al.* [2005], and Smith *et al.* [1993]. The design of the transducers, the operation practice, and all of the results for these second-sound experiments are presented in chapter 5.

Finally, at the end of this dissertation, a summary of all aspects discussed is presented in chapter 6. Also presented are suggestions and recommendations for further work, to continue the investigation into quantum grid turbulence.

Chapter 2

Theoretical Background

There are a number of different theoretical concepts that the reader will need as a background to the experimentation and results discussed in the later chapters of this thesis. These are described in the sections below.

2.1 Helium-4 and Superfluidity

Helium is the second most abundant element in the universe and yet it was not discovered on Earth until 1895, by the Scottish chemist Sir William Ramsey (Enss & Hunklinger [2005]); it was then liquefied for the first time in 1908 and along with it came the birth of low temperature physics. Helium has the lowest boiling point of all the known elements. This is due to the extremely small inter-atomic forces and large zero-point energy. Zero point energy, otherwise known as vacuum energy, is the energy of a quantum mechanical system's ground state; it is the lowest amount of energy an atom can have, even at absolute zero temperature. It is derived from the Heisenberg uncertainty principle and is an intrinsic quantum property of every atom, it is the energy left when all other energy has been removed from the system. This large zero point energy results in the fact that the liquid state of helium, at pressures below 25 bar, is always more energetically favourable than the solid phase, even at absolute zero.

Liquid helium itself also has some unique properties, in particular the plot of the specific heat of liquid helium has a large rise at 2.17 K, which is attributed to a 2nd

order phase transition. This transition is known as the *lambda transition*, named so as the graph resembles the Greek letter λ, as can seen in figure 2.1. The two liquid phases of helium are named helium-I and helium-II, although helium-II is more often than not referred to as *superfluid* helium due to its analogous properties with superconductivity. This superfluid phase also means that the phase diagram for helium, shown in figure 2.2, is unusual, especially considering that there is no triple point as solid helium requires a fairly large amount of pressure to be produced.

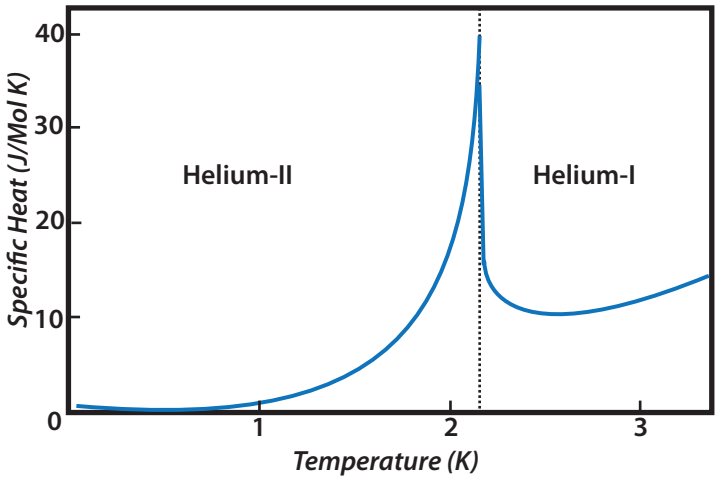

Figure 2.1: The specific heat of helium-4 as a function of temperature

^{4}He atoms are bosons with nuclear spin = 0, and therefore obey Bose-Einstein statistics; if it is assumed that helium is an ideal Bose gas then the transition to Bose-Einstein condenate is rpedicted to be at 3.1 K Enss & Hunklinger [2005]. The discrepancy in the transition temperature is due to the fact that liquid helium is not a non-interacting ideal Bose gas; there is a lower concentration of particles in the ground state. Superfluidity has a explained by a single condensate wave function, or collective excitations instead of separate ones for each individual particle. These collective excitations are known as *phonons* and *rotons* and they are depicted in the dispersion relation shown in figure 2.3. The critical velocity of the superfluid, depicted as a dotted line, is the lowest velocity for which a moving particle can cause excitations in the superfluid, thus dissipating kinetic energy. This is the Landau critical velocity and is described as $v_L = \frac{\Delta}{p_0}$.

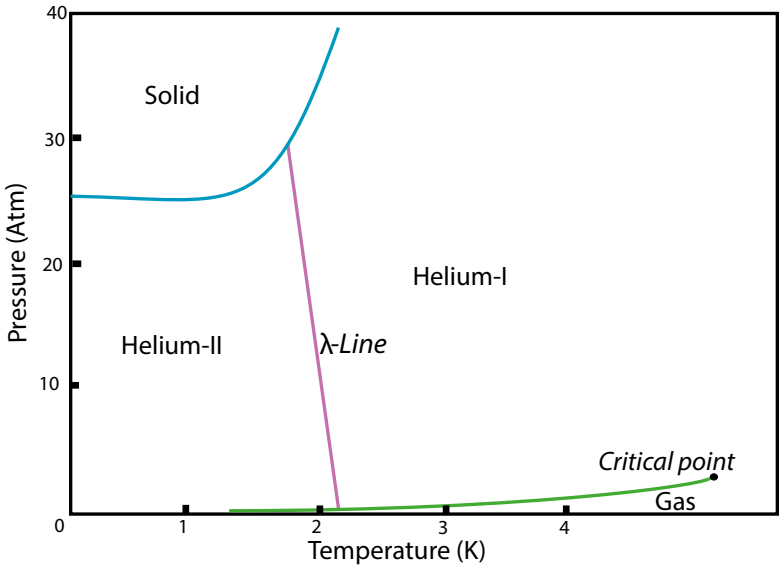

Figure 2.2: The phase diagram of helium-4, as a function of pressure and temperature

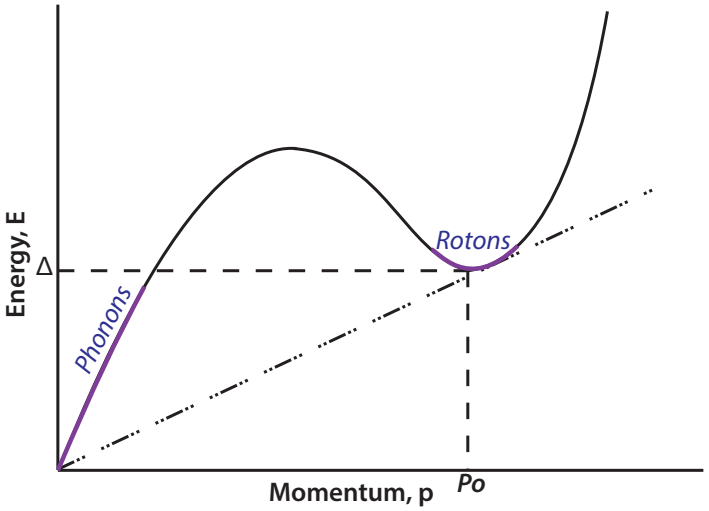

Figure 2.3: The dispersion curve for helium-4, the energy curve of particles as a function of momentum

[The straight line depicts the critical velocity]

2.1.1 Two Fluid Model

Superfluid helium has a vanishingly small kinematic viscosity, so when an experiment such as the one described in Kapitza [1938] is undertaken, it can be observed that the fluid flows through very small capillaries as though there is no viscosity in the system. However, when a rotary viscometer experiment like the one described

in Heikkila & Hallet [1955] is undertaken, a non-zero viscosity at temperatures well below the λ-transition is observed. These seemingly contradictory results are explained by the *two fluid* model, first suggested by Tisza in 1938. The liquid acts as though it is made up of two completely inter-penetrating fluids: the normal fluid component (with density ρ_n and velocity field $\mathbf{v_n}$) and the superfluid component (with density ρ_s and velocity field $\mathbf{v_s}$). It is important to note that there are not physically two separate fluids, and nor can you say that a particular atom is either 'normal' or 'superfluid'. However the model does explain the experimental data seen with helium-II. These two components carry different properties within the liquid, for example the normal fluid contains all of the entropy in the system, along with all of the viscosity. The ratio of superfluid to normal fluid in helium-II is temperature-dependent, as shown in figure 2.4, and below about 1 K the fluid can be well approximated as completely superfluid with zero entropy and viscosity.

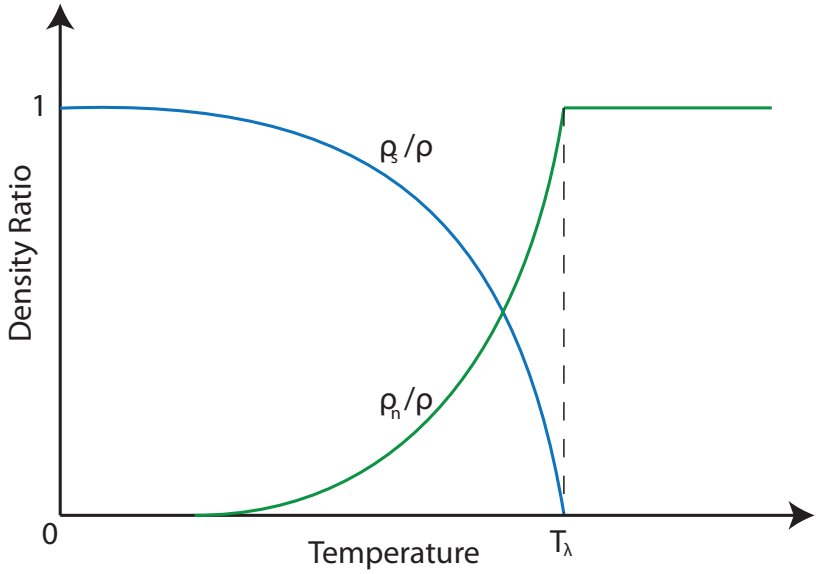

Figure 2.4: Temperature dependence of the normal fluid and superfluid densities, ρ_n and ρ_s, with respect to the total density, rho, for helium II

2.1.2 Vortices in Superfluids

The superfluid component can be described by a single macroscopic wave function:-

$$\Psi(\mathbf{r}) = |\psi_0|e^{i\phi(r)}, \tag{2.1}$$

where ψ_0 is the amplitude and the phase, $\phi(r)$, is a real function of position $\mathbf{r}$, i.e $(k\mathbf{r} - \omega t)$, where k is the wave number. Using this, and momentum $\mathbf{p} = k\hbar$, you can show that

$$\frac{\hbar\nabla\phi(r)}{m_4} = \frac{\hbar k}{m_4} = v \tag{2.2}$$

where m_4 is the mass of a helium atom. As $\nabla \times (\nabla \mathbf{f}) = 0$ it is clear that $\nabla \times v = 0$; superfluid is irrotational and therefore cannot undergo solid body rotation. However, we know that there is quantum turbulence in the superfluid, even at T$\rightarrow$0 and so there must be circulation. This problem is solved by having quantised vortices in the liquid (Feynman [1955]). If an annular, multiply connected region within the superfluid is imagined (think of a doughnut shape of helium-II), and using Stoke's theorem, we can write an equation for the flow pattern (or circulation)of a line within this region, κ :-

$$\kappa = \oint \mathbf{v_s} \cdot d\mathbf{l} \tag{2.3}$$

Using this with equation 2.2 we arrive at

$$\kappa = \frac{\hbar\Delta\phi}{m_4} \tag{2.4}$$

It is also known that the phase is a real function of $\mathbf{r}$, and the wave function is singular. This means that ϕ has to be in multiples of 2π and consequently the circulation is quantised:-

$$\kappa = \frac{nh}{m_4}, \qquad \text{where } n = 0, 1, 2, ... \tag{2.5}$$

The only way to have circulation in superfluids is with quantised vortices, which means there has to be something in the centre, the core of the vortex. The first time quantum vortices were observed was in 1961 by W.F. Vinen (Vinen [1961]) using a thin wire as the core. However without the presence of something like a thin wire, what is inside these quantum objects? Using equation 2.5 with equation 2.2 the velocity of the superfluid can be shown to go as $1/r$, where r is the radius from the centre of the vortex:-

$$v_s(r) = \frac{k}{2\pi r} \tag{2.6}$$

This means that at some small radius, the velocity of the superfluid exceeds the Landau critical velocity and will therefore cause the superfluidity to break down, this is shown in figure 2.5.

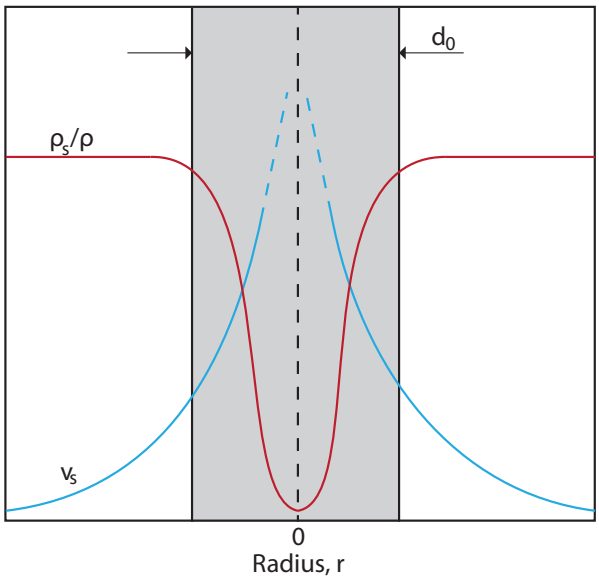

Figure 2.5: A diagram of the vortex core with respect to the radius from the centre. The shaded area depicts the normal fluid vortex core.

An approximation of the radius of the vortex core can be calculated from equation 2.6; using 58 m/s as the critical velocity and the unit of circulation as h/m_4, the core radius is approximately 2.7×10^{-10} m.

The energy of the vortex can be calculated by integrating over the kinetic energy per unit volume, E_v where the volume is the 'doughnut shape' of the

superfluid density that is rotating (Enss & Hunklinger [2005]) :-

$$E_v = \int_{a_0}^{b} \frac{\rho_s v_s^2}{2} 2\pi r \; dr \tag{2.7}$$

where a_0 is the radius of the core and b is half the distance between vortices. Integrating and using equations 2.5 and 2.6, it can be shown that:-

$$E_v = \frac{\rho h^2}{m_4^2} n^2 \ln \frac{b}{a_0} \tag{2.8}$$

Consequently, it is more energetically favourable for $n = 1$ than any other number, physically this means that the vortices will want to be singular.

2.2 Turbulence

Fluid systems are normally described in terms of conservation of momentum, energy, and mass. The Navier-Stokes equation is derived from these principles, in the form of Newton's second law:

$$\rho \left(\frac{\delta \mathbf{v}}{\delta t} + \mathbf{v} \cdot \nabla \mathbf{v} \right) = -\nabla p + \mu \nabla^2 \mathbf{v} + \mathbf{F} \tag{2.9}$$

where ρ is the fluid density, $\mathbf{v}$ is the flow velocity, p is the pressure, μ is the dynamic viscosity, and $\mathbf{F}$ is 'other' body forces (such as gravity). An analytical solution to this equation without some severe boundary conditions can be very difficult to compute, and for turbulent systems it is almost impossible. This results in the understanding of turbulence largely relying on experimentation.

2.2.1 Classical Turbulence

Turbulence is a flowing system characterised by time-dependent chaotic property changes; it is random and the fluid motion within is stochastic. It was first documented by Leonardo da Vinci in the 15th century, seen in figure 2.6, and has been investigated and discussed ever since.

As turbulence is inherently unpredictable, it is useful to introduce a dimen-

Figure 2.6: A photo of turbulence drawn by da Vinci in 1507. Photo taken from free media on the internet.

sionless quantity which can be used to characterise different flow regimes; the Reynolds number, Re. The Reynolds number is defined as the ratio of inertial forces to viscous forces:

$$\mathrm{Re} = \frac{UL}{\nu} \tag{2.10}$$

where U is the characteristic speed, L is the characteristic length, and ν is the kinematic viscosity. In a simple, incompressible flow around a smooth surface the Reynolds number is the only parameter involved in the transition to turbulence. A small Reynolds number means that viscous forces are dominant and therefore the flow is more likely to be laminar. A large Reynolds number indicates a large non-linear inertial term, leading to an unstable laminar flow and eventually turbulence (Vinen & Niemela [2002]).

Turbulent flow involves eddy (rotational) motion, on the characteristic length scale, L. However, as the Navier-Stokes equation (2.9) has a non-linear inertial term, motions on many different length scales are coupled together, as long as the Reynolds number is large. This results in no turbulent energy dissipation from larger scale eddy motion. Instead the energy 'cascades' to smaller scale eddies until $Re \to 1$, where viscosity becomes important again and dissipation occurs. The length scale at which this happens is known as the *Kolmogorov length scale*, K_ν. The range of length scales before viscous forces take effect is known as the *inertial range*.

In experiment, it is beneficial to simplify turbulence as much as possible, and

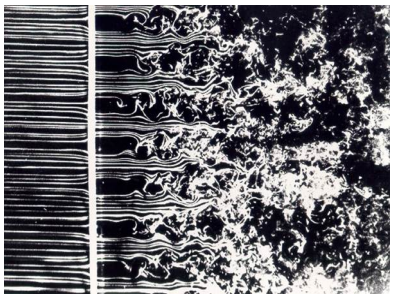

Figure 2.7: Photo of grid turbulence taken in a wind tunnel, photo taken from free media on the internet.

one such way is to create spatially homogeneous and isotropic turbulence by steady flow through a grid, as shown in figure 2.7. This results in an ideal case where energy only flows in k-space (Batchelor [1953]). At a distance away from the grid, much larger than the size of the mesh holes (M), the statistical properties of the turbulence are locally independent of position, making it essentially homogeneous. In reality the turbulence is decaying in time, though as a rule this decay takes seconds to occur and so has a negligible effect on the instantaneous local properties of the turbulence. As previously discussed, a range of different length scales must be considered for homogeneous turbulence. This is done through the use of the Fourier transform, $\mathbf{v}(k)$, of the velocity field, with a length scale k^{-1}. The fluid flow through a grid, at a speed U, will initially generate turbulence on the length scale M. The energy will then cascade though to smaller length scale eddies, known as the *Richardson cascade*. The energy also flows through to larger length scale eddies, saturating at the size of the container/flow channel, D; however the mechanism through which this occurs is as yet unknown. The energy cascade will continue without dissipation and with conservation of energy, until it reaches the aforementioned Kolmogorov length scale.

An important statistical property of grid turbulence is the energy spectrum, $E(k)$, such that $E(k)dK$ is the average turbulent energy per mass within the range of wavenumbers dk. The energy spectrum within the inertial range can only depend on the wavenumber, k, and the rate at which the energy flows through the cascade, denoted as ϵ. Through dimensional arguments, this leads to a distribution

of energy given by the *Kolmogorov* spectrum:

$$E(k) = C_K \epsilon^{2/3} k^{-5/3} \tag{2.11}$$

where C_K is the Kolmogorov constant which experimentally has proven to be of order unity for classical fluids, Sreenivasan [1995]. Even though Kolmogorov's theory of the inertial range is considered as one of the success stories of turbulence, it does not explain the large scale eddies. It is accepted that for small wavenumber, the energy spectrum is of the form $E(k) = Ak^n$, where A is positive number. n is either assumed to be 2 (see Saffman [1967]), or 4 (see Batchelor & Proudman [1956]); though it is generally accepted that the early time turbulence is Saffman turbulence (Krogstad & Davidson [2009]). The full energy distribution is shown in figure 2.8.

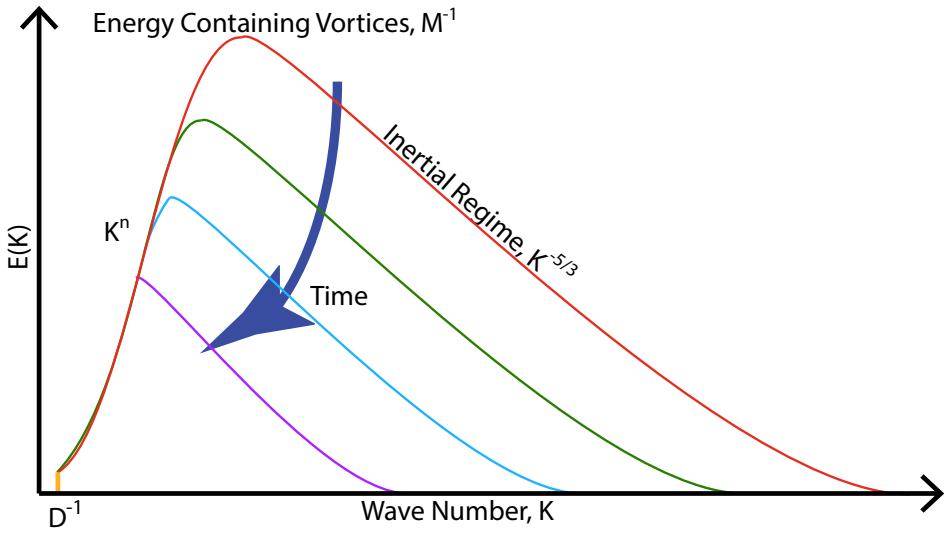

Figure 2.8: Energy decay spectrum of quantum turbulence, energy as a function of wavenumber. The separate curves represent the curve decay path over time.

At zero time, the energy containing vortices are at M^{-1}, and the energy containing scale then shifts towards the larger length scales over time, before saturating at the size of the experimental container. This suggests that if the energy injection scale, the mesh size, is small, then it will take a long period of time for the energy containing vortices to reach saturation.

2.2.2 Quantum Turbulence

Quantum turbulence is the name given to the turbulent flow of quantum liquids, for example superfluid helium or a Bose-Einstein condensate. However it is the tangle of quantised vortices (as explained earlier in section 2.1.2), as opposed to eddies, of which quantum turbulence is comprised. As in classical turbulence, it is important to consider the energy spectrum to try to explain the turbulence. In pure superfluids the dynamics of the motion is completely dependent on the vortices, and so the energy spectrum should yield a true insight into vortex dynamics in the Richardson cascade.

In homogeneous and isotropic quantum turbulence, there are two characteristic length scales; the mean intervortex spacing, $l = L^{1/2}$, where L is the vortex line density, and the coherence length corresponding to the vortex core, ξ. These length scales have corresponding characteristic wavenumbers; $k_l = 2\pi/l$ (which is equivalent to k_ν in classical turbulence), and $k_\xi = 2\pi/\xi$.

With k-values smaller then k_l (but larger than M^{-1}), the quantum turbulence dynamics are dominated by the collective vortex tangle (Bennemann & Ketterson [2013]). This means that the quantised circulation is not relevant and the dynamics is similar to that in classical turbulence; this region is referred to as the classical region and therefore the energy spectrum follows the Kolmogorov law (2.11).

Quantum vortices will transfer energy down from large length scales without dissipation through the Richardson cascade, just like eddies in classical turbulence. At temperatures above 1 K, once the wavenumber is sufficiently large (k_l), the dissipation will then occur through mutual friction, however at ultra low temperatures there is no normal fluid, and so the energy has to dissipate in some other way. Mutual friction is an interaction between the normal fluid and superfluid components, specifically an interaction between the superfluid vortex lines and the classical vortex tangle within the normal fluid.

An important and unique aspect in the Richardson cascade in quantum turbulence is *vortex reconnection*; two antiparallel vortices approaching each other will reconnect (Koplik & Levine [1993]). Such reconnections will cause 'kinks' in

the vortex line, in turn causing helical oscillations, or distortion waves, known as *Kelvin waves*. Self-reconnections will also occur, causing fission of vortex loops (Leadbeater *et al.* [2001]). At ultra low temperatures, all of these mechanisms will dominate in the region $k_l < k < k_\xi$, causing energy to cascade towards smaller length scales (through a *Kelvin wave cascade*), this region on the energy spectrum is known as the *quantum region*. It is predicted that the quantum region will obey a Kolmogorov-like power law: $E(k) \propto k^\eta$, where the exponent η is yet to be determined (Kozik & Svistunov [2004]). The dissipation of quantum turbulence after the quantum range is not yet completely understood, and is beyond the scope of this thesis.

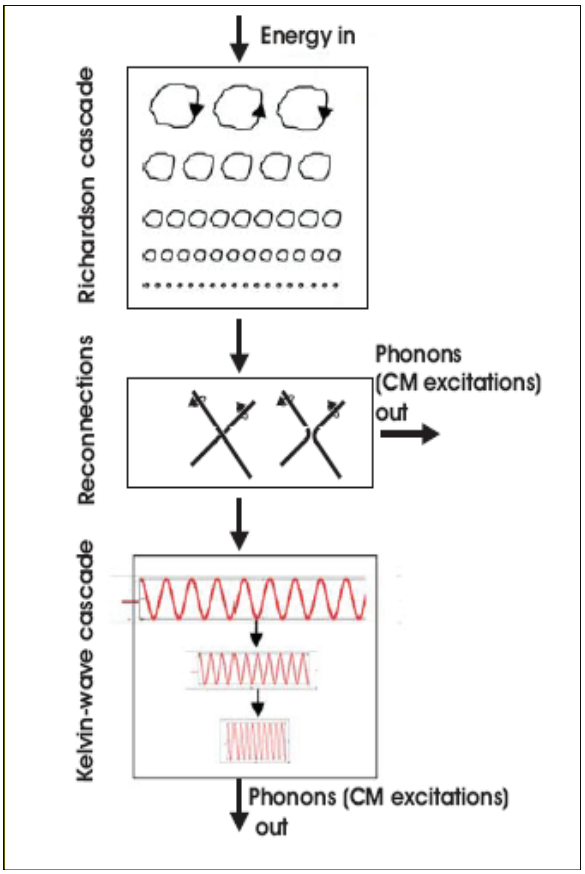

Figure 2.9: Cartoon depicting the energy cascade over time, through smaller length scales and three distinct regions, starting as large vortices and cascading down to phonons and rotons.

2.3 Cryostats and Dilution Refrigerators

In chapters 4 and 5 the experiments did not require anything below 1 K, and were therefore carried out in a cryostat, which is essentially a large Thermos flask. Using a rotary vacuum pump, you can pump the helium bath down to temperatures close to 1 K with the process of evaporative cooling. The pump creates a lower vapour pressure above the surface of the liquid, this means that the helium particles with higher energies can escape resulting in the energy of the system decreasing, and therefore the temperature. The cooling power of this set-up relies on the pumping speed of the pump and usual base temperatures are in the range of 1 2 - 1.3 K. This method of cooling is not good for helium consumption as you lose about 45 % of the bath through evaporation. However if there is a good helium recovery system, like the ones at Lancaster University or at the University of Florida, this helium is saved and re-liquifed, so a minimal amount is actually lost to the atmosphere.

For the experiments discussed in chapter 3 however, milli-Kelvin temperatures were needed, leading to the use of a dilution refrigerator. The concept and science of a dilution refrigerator was suggested by F. London in 1951, though it was not published for another 10 years, in London *et al.* [1962]. A schematic of a dilution fridge is shown in figure 2.10. One of the main ideas of a dilution fridge is that only a small volume of helium has to be cooled, and then the use of heat exchangers and good thermal contact is utilised to cool other areas.

The 1 K bath (sometimes known as the 1 K pot), does not actually reach 1 K, it is cooled using evaporative cooling and so gets down to about 1.2 K. Once the fridge is in thermal equilibrium with the pot, a ^{3}He-^{4}He mixture is added in gaseous form. It will will cool and condense before it reaches the mixing chamber. This liquid mixture has some unique properties, mainly due to the fact that ^{3}He particles are fermions (with integer spin = 1/2) and therefore obeying Fermi statistics. At low temperatures, it becomes more energetically favourable for the mixture to separate into two phases; a light, ^{3}He rich phase on top, and a heavy, mostly ^{4}He phase at the bottom. This can be seen in the phase diagram shown in

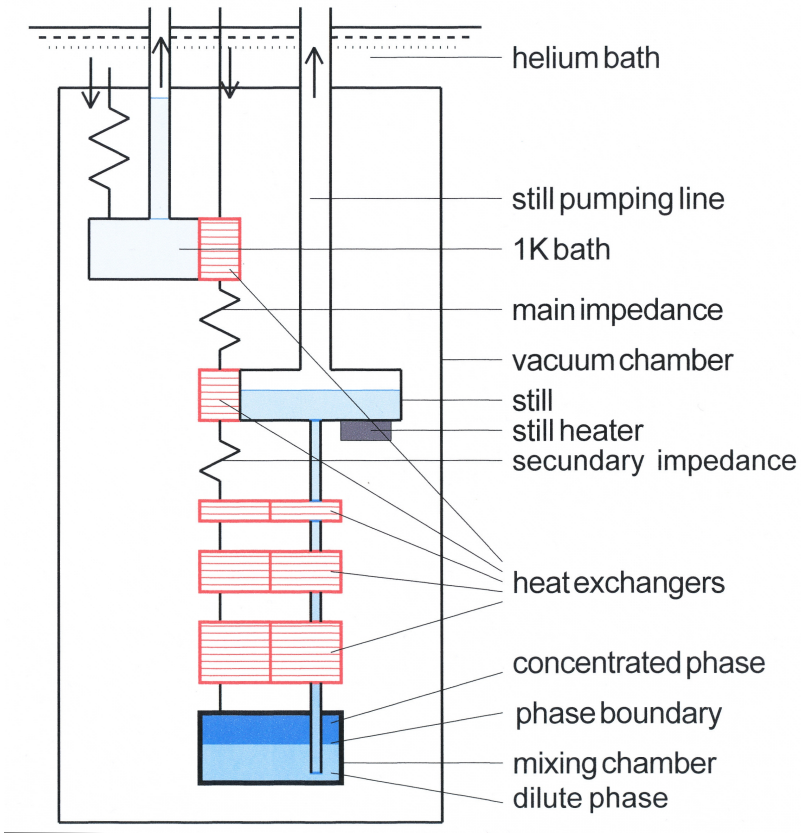

Figure 2.10: A schematic of a typical dilution refrigerator, without a demagnetisation stage.

figure 2.11. Basically when the ^{3}He particles cross the phase boundary from the concentrated to dilute phase, for entropy to be conserved the process has to be endothermic(for a more in-depth explanation into why this occurs, please refer to Lounasmaa [1974] , pages 18-22). So in practice, if you can cause ^{3}He atoms from the light, concentrated phase to move into the heavier, dilute phase you produce a cooling effect (analogous to normal evaporative cooling with the dilute phase corresponding to a vapour).

For the fridge to operate in continuous mode, the helium mixture is condensed and sent through the heat exchanger next to the 1 K pot, bringing it's temperature down to about 1.2 K. After this it will flow through the heat exchangers next to the still where the temperature drops to about 0.7 K, the liquid is then cooled further through the lower heat exchangers before finally reaching the concentrated phase in the mixing chamber. As there is an osmotic pressure gradient, the ^{3}He atoms

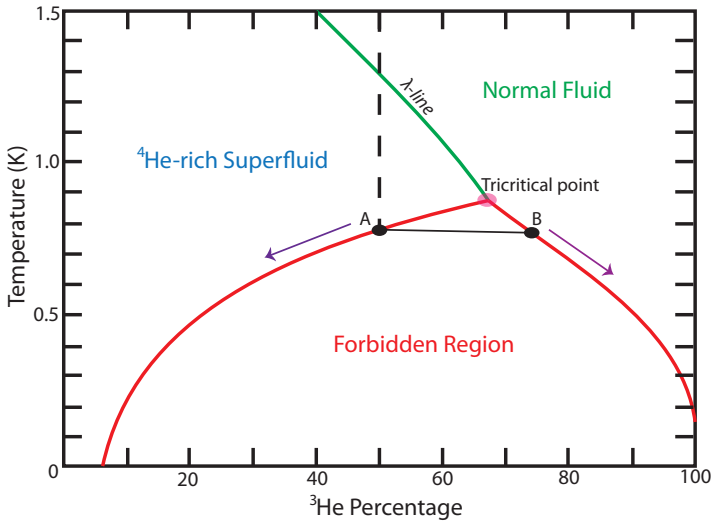

Figure 2.11: A diagram of ^{3}He percentage with respect to temperature, showing the theoretically determined forbidden region of ratio and temperature.

will cross the phase boundary into the dilute phase and travel up to the still. The vapour in the still is pumped out, the vast majority of which is ^{3}He. This is then circulated back to the beginning and the process starts again, a heater is placed in the still to ensure a sufficient gas circulation. When starting this process, the gas circulation is started using a rotary pump, and then a diffusion pump. Of course the mixing chamber has to be a cold enough temperature for separation to occur before the heater is switched on (Lounasmaa [1974]).

It should be noted that through the use of a dilution refrigerator temperatures of about 2 mK can be reached. To get below this a magnetic cooling stage may be added, for example a *nuclear de-magnetisation stage*, which can bring the experimental cell down to the μK range. However this technique is not pertinent to this dissertation and will therefore not be discussed, the reader is again recommended to read Lounasmaa [1974] for further information.

2.4 Magnetic Levitation and Superconductivity

Magnetic levitation is a method of suspending an object with no support other than magnetic fields. This can be done using diamagnetic materials, eddy currents or with superconductive materials; this thesis concentrates on the latter.

A superconducting material, once cooled below a characteristic *critical temperature*, T_C, will exhibit zero resistance and the expulsion of magnetic fields. For a full review on this subject the reader is directed to Tilley & Tilley [1974], a brief review is described below.

An electron moving through a lattice will cause a slight deformation in the charge density, causing another electron to to move into an area of higher positive charge. These electrons become 'bound', or paired; these paired electrons are known as *Cooper Pairs* (Cooper [1956]). Once below T_C, the binding energy of a pair of electrons causes a gap in the energy spectrum at the Fermi energy, separating the paired states from the 'normal' single-electron states. The quantum mechanical effect keeping the electrons together is a very weak, pairing interaction energy, and so only at low temperatures are there a significant number of Cooper pairs for superconductivity to occur.

The fact that there is a gap in the energy spectrum means that low energy excitations which would cause the electrons to disperse, or scatter, are forbidden. According to *Bardeen-Cooper-Schrieffer theory, or BCS theory*, (Bardeen *et al.* [1957]), the paired electrons can move throughout the lattice without hindrance, carrying with them the current.

The act of expelling magnetic fields from a superconducting material is known as the *Meissner Effect*. Given that the resistance is zero, supercurrents are generated within the material which will perfectly cancel out any exterior magnetic field brought near. The supercurrents will also mirror the magnetic poles causing a repulsion force which can often be enough to levitate either the superconductor or the external magnet.

When describing a superconducting material there are two important factors;

the *London penetration depth*, λ_L, and the *superconducting coherence length*, ξ_s. An external magnetic field is not expelled from the whole superconducting material, in fact it falls off exponentially past the surface boundary. The distance at which the magnetic field reaches a value of $1/e$ times the original field is the London penetration depth (Hook & Hall [1991]):

$$\lambda_L = \left(\frac{m}{\mu_0 n q^2}\right)^{1/2} \tag{2.12}$$

where m is the charge carrier mass, n is the number density and q is the charge. The superconducting coherence length is the mean distance between the Cooper pair electrons; it is dependent on the Fermi velocity, v_f, and the superconducting energy gap, Δ:

$$\xi_s = \frac{2\hbar v_f}{\pi \Delta} \tag{2.13}$$

There are two types of superconductors; Type-I and Type-II. In a Type-I the superconductivity will be abruptly destroyed when an external magentic field exceeds a characteristic critical field, H_C, via a first order phase transition. A Type-II superconductor has two critical fields; H_{C1} and H_{C2}. H_{C1} is when magnetic vortices first appear within the superconductor as the external magnetic field is increased, and H_{C2} is when the superconductivity is completely destroyed. The ratio of λ_L/ξ_s determines whether or not a superconductor is a Type-I or Type-II, though generally speaking pure metallic elements are Type-I and metallic alloys are Type-II (with pure Nb being one of the exceptions).

2.5 second-sound

As previously discussed, the two separate helium-II components each carry different properties of the liquid. One result from this phenomena is the fact that several different sound modes can be found, the second of which is of particular interest for this dissertation. When the superfluid and normal fluid components oscillate 180° out of phase with each other, a longitudinal wave with temperature (or entropy) propagating is produced; this is known as second-sound. The wave can be created using an AC voltage across a resistive heater with the temperature distribution being measured by a thermometer moving with respect to the heater [Enss & Hunklinger, 2005]. However there is another method which uses a superleak membrane mechanically oscillating to produce the second-sound wave, this is the method used and described in chapter 5. second-sound velocity, u_2, is temperature dependant, a plot of second-sound velocity as a function of temperature is shown in figure 2.12.

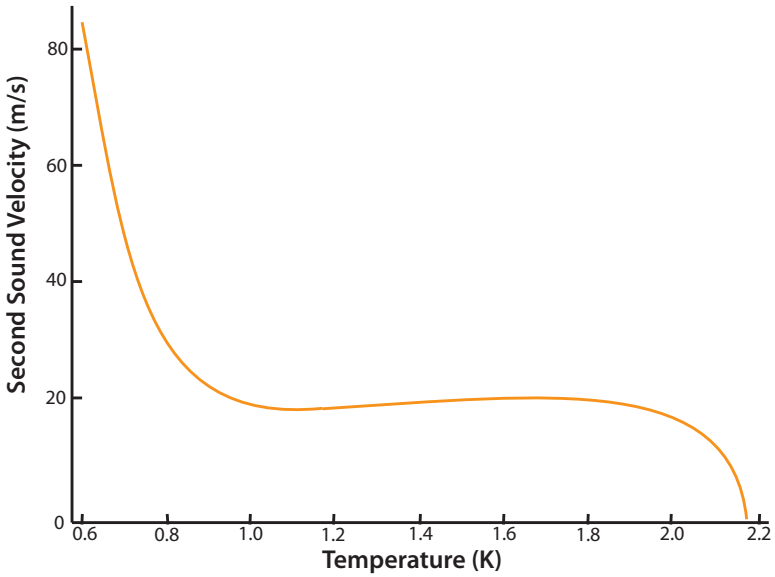

Figure 2.12: second-sound velocity as a function of temperature, in liquid helium-4

2.5.1 Attenuation

A second-sound (SS) signal will be attenuated by any vortices or quantum turbulence it encounters. The main cause of this attenuation is an extra thermal conductivity due to the drift motion of excitations [Tilley & Tilley, 1974]. The quantised vortex is in the superfluid, with a normal fluid core. SS involves normal fluid/superfluid counterflow, and will therefore be dissipated by the drag on the normal fluid core. The attenuation of SS can be used to determine the vortex line density, L, in a volume of quantum turbulence, the line density is then related to the vorticity, ω, of the turbulence with equation 2.14:-

$$\omega = \kappa L \tag{2.14}$$

where κ is the circulation.

The attenuation of the signal cannot simply and solely be attributed to the line density of the turbulence. Other factors that can cause it are the experimental cell dimensions along with properties contained within the liquid [Hanson & Pellam, 1954], and viscous surface losses [some citation that I can't find]. Therefore the total attenuation of the second-sound is $\alpha_T = \alpha_B + \alpha_L$, where α_B and α_L are the background attenuation (due to all experimental factors) and the attenuation due to vortices, respectively. The *bulk liquid* attenuation is considered to be a constant throughout as the experimental cell does not change, also it is completely submersed in the liquid helium at all times during runs, the attenuation due to surface losses is assumed to be negligible.

The bulk attenuation is given by equation 2.15:-

$$\alpha_b = \frac{f_{ss}^2}{2\rho u_2^3}\left[\left(\frac{4}{3}\eta + \zeta_{II}\right)\frac{\rho_s}{\rho_n} + \frac{K}{C_p}\right] \tag{2.15}$$

where f_{ss} is the frequency of the SS wave, ρ is density, η is viscosity, ζ_{II} is a second viscosity coefficient, K is a constant parameter analogous to the ordinary

thermal conductivity coefficient, and C_p is the ordinary specific heat capacity of liquid helium II [Hanson & Pellam, 1954].

A full derivation of the attenuation due to quantised vortex lines can be found in Stalp [1998], pages 53-62; the principle steps of which are described below. It should also be noted that the author has opted to only concentrate on the analytic solution for arbitrary vorticity and bulk attenuation. It is assumed that a porous, superleak vibrating membrane is used as the SS wave transmitter with a similar membrane directly opposite used as a receiver.

To begin, the SS wave is approximated as a plane wave with wavelength λ, frequency $f_s s$, phase ϕ, and amplitude A_{T^0}. Therefore at some time D/u_2 (where D is the width of the channel), the wave can be described as:-

$$A(f_s s, D/u_2) = A_{T^0} e^{-\alpha D} e^{i(kD - f_{ss} D/u_2 + \phi)} \tag{2.16}$$

where α is an attenuation coefficient $\alpha = \alpha_r + i\alpha_i$, the real part of which is assumed to be the total physical attenuation; $\alpha_r = \alpha_T = \alpha_B + \alpha_L$. Defining N as half the number of reflections and R as the reflection constant, the received signal of the wave, A_r, at infinite time (and therefore $N \to \infty$) can be described as:-

$$A_r(f_{ss}, \infty) = \frac{A_T}{e^{(a-ib)} - e^{(-a+ib)}} \tag{2.17}$$

where

$$A_T = A_{T^0} e^R, \tag{2.18}$$

$$a = \alpha_T D + R, \tag{2.19}$$

and

$$b = (f_{ss}/u_2 - \alpha_i) D. \tag{2.20}$$

Experimentally, the wave will be measured using a lock-in amplifier and will therefore be the magnitude of A_r:-

$$A(f_{ss},\infty) = [A_r(f_{ss},\infty)A_r^*(f_{ss},\infty)]^{1/2} = A_T[2\cosh(2a) - 2\cos(2b)]^{-1/2} \quad (2.21)$$

From this, the resonance frequency (i.e. when $\cos(2b) = 1$) for the n^{th} mode can be given by:-

$$f_{ss}^n = \frac{nu_2}{2D} + \frac{\alpha_i u_2}{2\pi} \quad (2.22)$$

Using this, with equation 2.20, and solving equation 2.21 for b gives:-

$$b = \frac{2\pi D}{u_2}(f_{ss} - f_{ss}^n) + n\pi \quad (2.23)$$

Take the half power frequency, f_h, as the frequency at which $A^2(f_n) = 2A^2(f_h)$, and define the 'full width half max' as $\Delta = 2 \mid f_{ss}^h - f_{ss}^n \mid$. Taking the situation where there are no vortices, $\alpha_L = 0$, and using the relationship $\text{arcosh}(x) = \ln(x + \sqrt{x^2 - 1})$, it can be shown that

$$2\alpha_B D + 2R = \ln\left[1 + C + \sqrt{(2C + C^2)}\right] \quad (2.24)$$

where

$$C = 1 - \cos\left(\frac{2\pi D\Delta_0}{u_2}\right). \quad (2.25)$$

The amplitude of a SS wave at resonance with no vortices present can be written as

$$A_0 = A(f_{ss}^n, \infty, \alpha_L = 0) = A_T[2\cosh(2\alpha_B D + 2R) - 2]^{-1/2} \quad (2.26)$$

Using this along with equation 2.21, the attenuation due to vortices is shown to be

$$\alpha_L = \frac{1}{2D} \ln \left[\frac{1 + \left(\frac{A}{A_0}\right)^2 C + \sqrt{2\left(\frac{A}{A_0}\right)^2 C + \left(\frac{A}{A_0}\right)^4 C^2}}{1 + C + \sqrt{2C + C^2}} \right] \tag{2.27}$$

Hall & Vinen [1956] gives a now well established equation for vorticity, ω, of homogeneous and isotropic vorticity with respect to SS attenuation:-

$$\omega = \frac{16 u_2}{\pi B} \alpha_L \tag{2.28}$$

where B is the temperature dependant mutual friction parameter. Therefore, the use of equation 2.27 with equation 2.28 gives the final, and desired, equation for vorticity:-

$$\omega = \frac{8 u_2}{\pi B D} \ln \left[\frac{1 + \left(\frac{A}{A_0}\right)^2 C + \sqrt{2\left(\frac{A}{A_0}\right)^2 C + \left(\frac{A}{A_0}\right)^4 C^2}}{1 + C + \sqrt{2C + C^2}} \right]. \tag{2.29}$$

It has been argued (for example Chagovets *et al.* [2007]) that the pre-factor in equation 2.29 is different to that described here, substituting 3 for the $8/\pi$. This would have no effect to any of the data presented here, or conclusions made, other than shifting the effective kinematic viscosity values up or down by this factor. As the author is only discussing trends, the correct pre-factor is unimportant to this thesis.

Chapter 3

Turbulent Drag from Oscillating 'Floppy Devices'

Mechanical oscillators have been used to investigate the decay of quantum turbulence in liquid helium by a number of different groups; for example Yano [2009] and Bradley *et al.* [2005] with small vibrating wires, or Blažková *et al.* [2007] and Ahlstrom *et al.* [2013] with vibrating forks. A variant of the mechanical oscillator described here, known as the 'floppy device', was first introduced in Berent & Polturak [1998] where it was used to study solid helium. This device can produce large amplitudes of motion with an extensive range of velocities. It also allows for low frequency motion to be investigated with high precision (Bradley *et al.* [2011]).

As any macroscopic object is cooled down to superfluid temperatures, remnant vortices are left trapped on the roughness of the surface. Once a critical velocity is reached these vortices can grow; the vortices will interact and reconnect with each other producing quantum turbulence. The moving object, or floppy device, will then feel a measurable extra drag force due to this turbulence.

It is possible to model the floppy devices, or any oscillating object, as a mass on a spring with simple harmonic motion via a driving force, F:

$$F = F_0 e^{ift} \tag{3.1}$$

The natural frequency of which will be $f_0 = \sqrt{K/m}$, where K is the spring

constant, and m is the mass of the object in vacuum.

It is then possible to write the equation of motion; taking into account the velocity dependent fluid damping force, D_F, and the effective mass of the object (due to both clamped fluid on the object, and the fluid back-flow due to the displaced mass), $m + \delta m$:

$$(m + \delta m)\ddot{x} + D_F\dot{x} + f_0^2 = F_0 e^{ift} \tag{3.2}$$

The steady state solution to equation 3.2 is:

$$\dot{x} = \dot{X}e^{ift} \tag{3.3}$$

Substituting this into equation 3.2 leads to:

$$\dot{X} = \frac{F_0 if}{-f^2(m + \delta m) + ifD_F + K} \tag{3.4}$$

which is comprised of real and imaginary parts:

$$\Re\{\dot{X}\} = \frac{F_0 f^2 D_F}{f^2 D_F^2 + (f^2(m + \delta m) - K)^2} \tag{3.5}$$

and

$$\Im\{\dot{X}\} = \frac{F_0 f(k - f^2(m + \delta m))}{f^2 D_F^2 + (f^2(m + \delta m) - K)^2} \tag{3.6}$$

The real and imaginary parts are in and out-of-phase with the driving force, respectively. Figure 3.1 graphically depicts the in and out-of-phase parts of a resonance.

3.1 Construction and Operation

Two different and separate floppy devices were used in the experiment discussed in this chapter, one of which has a rectangular piece of copper mesh attached, this is so it can produce large quantities of quantum turbulence at once; this device is

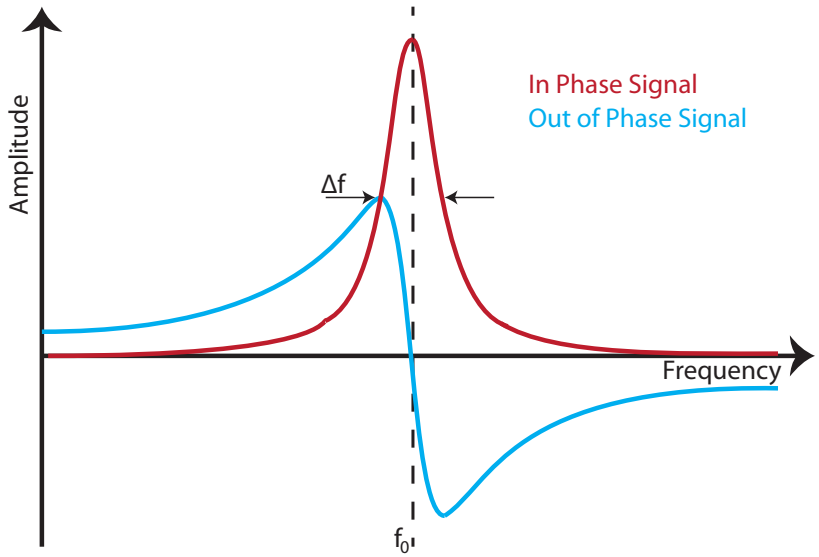

Figure 3.1: A diagram showing the ideal in and out of phase components of the Lorentzian peak, for a simple harmonic oscillator

known as the 'floppy grid'. Pick up coils are also used to detect the position, as described below.

The floppy devices were made from a single-filament NbTi Copper clad insulated wire, of 100 μm diameter. The wire was bent over a 10 mm wide rectangular former to make a goalpost shape. The 20 mm long legs of this goalpost were attached to a small rectangular piece of paper hardened with Stycast 1266. For the floppy grid, a 5 $\times$ 10 mm piece of fine copper grid mesh is attached to the top of the goalpost using very minute amounts of Stycast. The mesh is approximately 1 μm thick with 23 μm square holes separated by 11 μm thick copper strips, shown in the insert of figure 3.2. Two pick up coils were positioned above and to either side of the floppy device, these coils are made from 135 turns of 140 μm single core NbTi copper clad insulated superconducting wire. Figure 3.2 shows the floppy grid with the pick up coils positioned above.

Two cells were constructed for this experiment; one with a floppy wire sans grid and one with a floppy grid in. Both cells also contained very small vibrating wires (with 3 mm leg spacing), and a 2 $\times$ 8 $\times$ 12 mm silver sinter for thermal contact. A schematic of the floppy wire cell is shown in figure 3.3; both cells have two pick up coils set approximately 1 mm above the top of the cell. Once in the

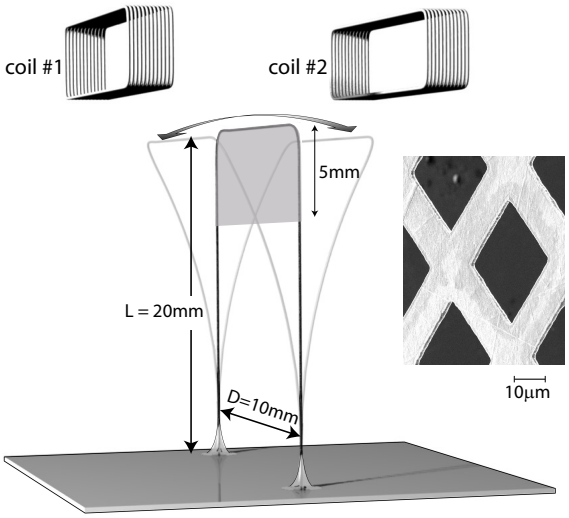

Figure 3.2: The floppy grid device with pick-up coils
Insert shows an image of the copper mesh taken with an electron microscope.

dilution refrigerator, both devices were operated in an 82 mT vertical magnetic field provided by a large superconducting magnet, which is located in the 4.2 K helium bath surrounding the refrigerator (Bradley *et al.* [2012]).

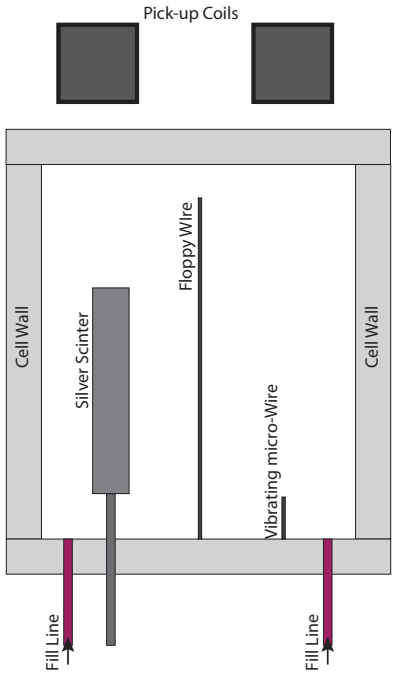

Figure 3.3: A 'side view' schematic showing the cell layout for the 'floppy wire'

The floppy devices are driven into oscillation by the Lorentz force when an AC

'drive current', $I_0 e^{ift}$, is passed through the wire, the amplitude of this driving force is:

$$F_0 = BD_l I_0 \tag{3.7}$$

where B is the magnetic field, and D is the leg spacing of the floppy device. As the crossbar moves, it produces a Faraday voltage, V, proportional to its velocity, v:

$$V = BD_l v \tag{3.8}$$

This voltage is measured by a phase-sensitive lock-in amplifier referenced to the function generator providing the drive current. The voltage from the function generator is converted to the drive current using a home made 'drive box'. The box has a range of resistors in series with a 100 Ω resistor, this allows for the range of currents needed. Driving the floppy device over a range of frequencies produces the expected Lorentzian peak at the resonant frequency, such as that in figure 3.1. The resonant frequencies in vacuum at 4.2 K for the floppy wire and floppy grid were found to be 95.82 Hz and 59.55 Hz respectively. Once the resonance is found, a LabView programme is used to keep the floppy device on resonance by keeping the out of phase signal to zero. By using this method, the amplitude of the drive force can be increased and the resulting velocity recorded.

The drag force can be described in terms of the drag coefficient (Morison *et al.* [1950]):

$$F = \frac{1}{2}\rho v^2 A_x C_d \tag{3.9}$$

where ρ is the density of the helium, and A_x is the cross sectional area of the object perpendicular to the motion; for the floppy grid this is the solid area of the mesh. When on resonance, the drive force balances the drag force on the floppy device. Using equation 3.7 with equation 3.9, the drag coefficient is then calculated and presented.

3.1.1 Low Frequency Measurements

The pick up coils are used to measure the position of the crossbar of the floppy devices. They can detect small perturbations in the position to a high precision. A high frequency alternating 'probe' current is linearly superimposed on the AC drive current using a custom-made current source. The result is an induced voltage in the pick up coils due to the mutual inductance between the wire and the coils. The probe current is set to a much higher frequency to that of the resonance, about 90 kHz, to ensure it does not induce any additional motion in the floppy device. Two separate lock-ins record the induced voltage for each coil, a third is used to record the voltage across a high power standard resistor placed in series with each of the floppy devices; all three lock-ins are referenced to the high frequency probe current.

The induced voltage in the coils is dependent on the relative position of the cross bar of the floppy device. When the floppy device is directly beneath the coils, it is assumed that it will result in a peak in the signal recorded from the coil. Likewise, it is assumed that when the floppy device is directly between both coils, both lock-ins measuring the coil voltages will show the same value. In reality this is not quite the case because, due to the arcing motion of the floppy device, when the cross-bar moves directly below the coils it has slightly shifted down, and therefore this position may not result in the maximum measured signal. The effect of this, however, is assumed to be negligible. The signal change with respect to position is demonstrated in figure 3.4, which is used for the calibration.

The distance between the coils is designed, and measured, as 6 mm. It is defined that ΔI_S is the change in steady drive current, I, needed to move the floppy device from the midpoint of the coils, I_m to directly underneath one of them, I_c; the displacement corresponding to this is ΔX_0, a distance of 3 mm (shown in figure 3.4). The drive force on the crossbar will then generate a deflection due to the effective spring constant k:

$$F = K\Delta x \tag{3.10}$$

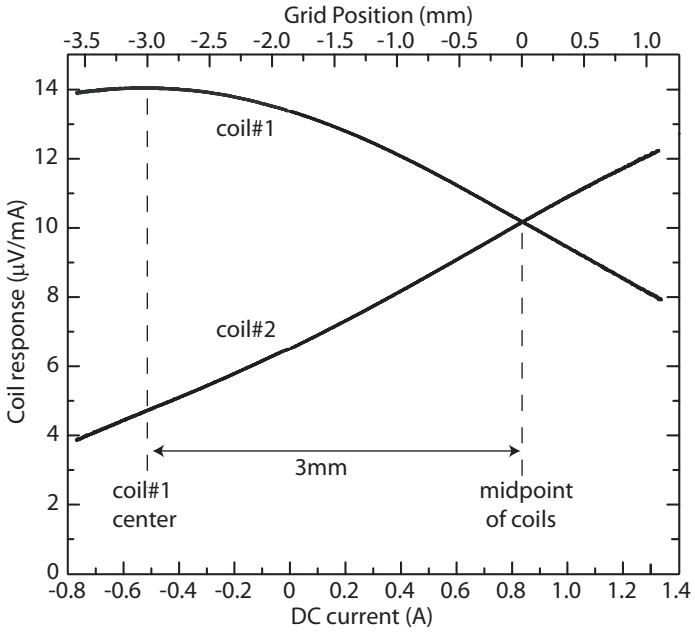

Figure 3.4: A plot showing the induced voltage in the two pick-up coils with respect to high frequency DC current. The curves represent slow movements of the floppy device, moving towards, and away from, coil 1.

where Δx is the horizontal displacement of the floppy device crossbar, relative to its equilibrium position. Equating equations 3.10 and 3.7, it is possible to calculate the distance the floppy device moves, x, from the equilibrium position (the mid point between the coils) due to the steady state current, I, is:

$$x = \frac{\Delta X_0}{\Delta I_S}(I - I_m) \tag{3.11}$$

The calibration of the pick up coils, to determine position, can then be used to investigate the frequency dependence of the drag forces on the floppy device, as it is no longer necessary to work on resonance. A steady drive current is chosen so that the crossbar is at a position where the coil response is linear. In practice this is close to the midpoint between the two coils, where the response is linear over a range of about 1 mm in displacement. The drive current, I_0, is oscillated around the chosen position with any arbitrary frequency, f, producing a sinusoidal modulation of the coil signal. An additional lock-in amplifier, referenced to the drive current generator, is used to measure the amplitude and phase of the oscillating coil. The

oscillating position can be described as:

$$x_0 = xe^{i(wt)} \tag{3.12}$$

where x is the amplitude of the equilibrium position, using equation 3.11, and θ is the phase shift with respect to the drive current. Particular care is needed to account for the finite time-constants of the lock-in amplifiers, as these can introduce additional phase shifts. As the frequency tends towards resonance, the phase shift tends towards 90° and x_0 goes through a maximum. At higher frequencies, the x_0 drops and the phase shift tends towards 180° (Bradley *et al.* [2012]).

The dissipative drag force on the floppy device produces an average power dissipated, $\dot{Q}$:

$$\dot{Q} = \frac{1}{2} F_0 v_0 \sin\theta \tag{3.13}$$

where $v_0 = f x_0$ is the velocity resulting from the small oscillations around x_0. The dissipation itself is caused by the dissipative drag force, F_{d^0}; therefore the energy dissipated can also be written as:

$$\dot{Q} = \frac{1}{2} F_{d^0} v_0 \tag{3.14}$$

giving the amplitude of the drag force on the floppy device for arbitrary frequencies as:

$$F_{d^0} = F_0 \sin\theta. \tag{3.15}$$

3.2 Results and Conclusions

3.2.1 Floppy Wire

The measured response, on resonance, for the floppy wire is presented in figure 3.5. These measurements were taken by slowly ramping up the amplitude of the drive current, at 4.2 K in a vacuum, 4.2 K in normal liquid helium, and at approximately 4 mK in superfluid helium. The latter temperature could not be verified as there as no independent thermometer in the experimental cells; however, it has been shown (Schoepe [2004]) that the response of vibrating objects below 100 mK become temperature independent.

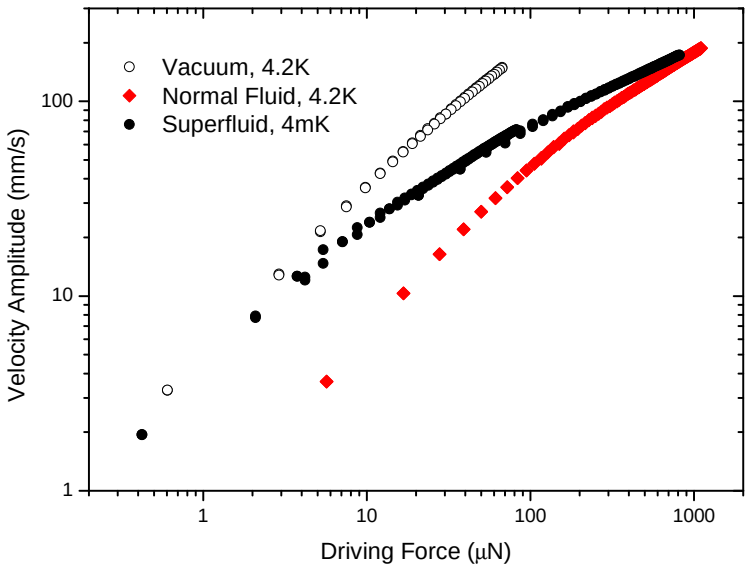

Figure 3.5: A plot showing the velocity amplitude of the floppy wire, on resonance, as a function of driving force

At low velocities, the response curve at millikelvin temperatures is similar to that found in a vacuum. This is as expected; before a critical velocity, the wire does not interact with the superfluid (there is no measurable viscous damping). After a critical velocity, there is a transition into the non-linear, turbulent regime. The curve eventually joins the curve measured in the normal fluid, becoming non-

linear, which is attributed to vortices and turbulence.

Using equation 3.9, and subtracting the internal drag forces of the wire, it is possible to show the fluid drag force as a function of velocity; this is presented in figure 3.6. The internal drag force for the data obtained in normal fluid, at 4.2 K, was assumed to be the drag force calculated from vacuum data, taken at the same temperature. However, it is very difficult to measure the vacuum damping at the low temperature limit due to the lack of thermal coupling. It was assumed that the response for mechanical oscillators does not change substantially below 4 K, and therefore the vacuum measurements taken at 4.2 K were subtracted from the values taken at the low temperature limit. To ensure a precise value was used however, a multiplicative factor of 0 65 was used, to ensure that the fluid forces vanish at low velocities.

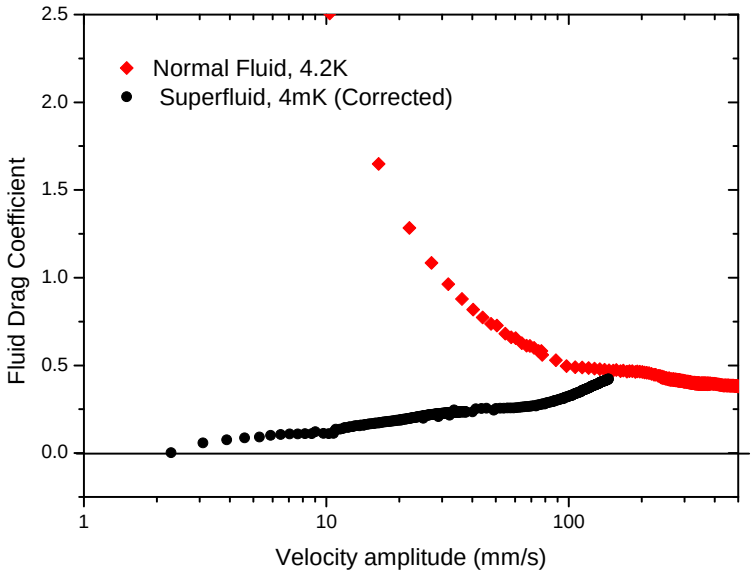

Figure 3.6: A plot showing the fluid drag coefficient (the total drag coefficient after subtracting the vacuum, internal drag), as a function of velocity, for the floppy wire.

This plot, along with figure 3.5, shows an approximate critical velocity, for the onset of turbulnce, of 11 mm/s. The fluid drag coefficient, at 4.2 K, is shown to tend towards a constant of approximately 0 35. This is far from the order unity expected from classical experiments, though it does agree with results presented

in Bradley *et al.* [2009] which were obtained from tuning forks in superfluid at low and very low temperatures.

Using the method outlined in the previous section, the floppy wire was then driven at various frequencies; the drag force, inferred from equation 3.15, as a function of velocity for various frequencies within the range of 9 to 100 Hz. It was found that there is no significant dependence on the oscillation frequency. Although, there is a larger spread in the data than originally expected. It is believed that this is mainly due to remnant vortices left on the wire. The drag force seems to remain proportional to the squared velocity, up to velocities of approximately 200 mm/s.

3.2.2 Floppy Grid

All of the results presented in this this section can also be found in Bradley *et al.* [2012]. Figure 3.7 shows the velocity of the floppy grid, as a function of driving force. As with the floppy wire, the plot shows curves taken in vacuum at 4.2 K, in normal fluid at 4.2 K, and in superfluid at the low temperature limit.

Also as before, the curve representing millikelvin temperatures follows a linear regime at low velocities, as the vacuum curve does throughout. At a critical velocity, the curve then becomes non-linear, joining with the normal fluid curve, indicating the production of vortices and turbulence.

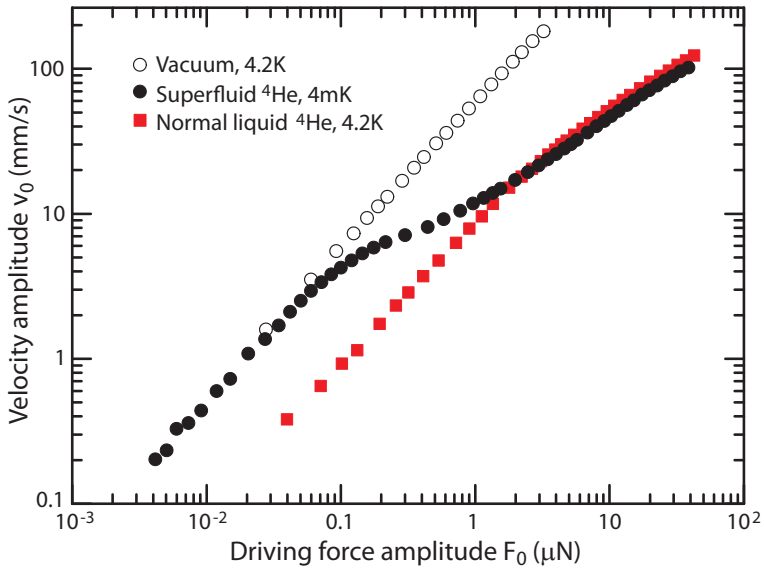

Figure 3.7: A plot showing the amplitude velocity of the floppy grid, on resonance, as a function of driving force

Using equation 3.9, the drag coefficient (for the normal fluid at 4.2 K and for superfluid at the low temperature limit) as a function of velocity is presented in figure 3.8. This shows more clearly the transition from the linear to the turbulent regime for the floppy grid at millikelvin temperatures. At low velocities, the drag in the normal fluid is dominated by viscosity. The drag coefficient curve for the low temperature limit, at high velocities, seems to be similar to that in normal fluid. This indicates that the dissipative turbulent drag for fully developed quantum turbulence is similar to that of classical turbulence.

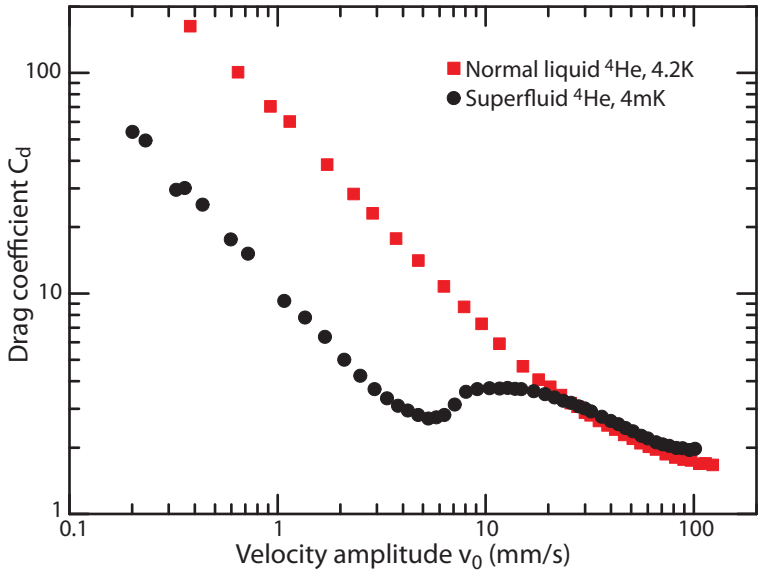

Figure 3.8: A plot showing the (total) drag coefficient of the floppy grid as a function of velocity amplitude, for helium in the normal phase and superfluid phase.

The internal drag forces can be subtracted from the data of figure 3.8, to leave just the fluid drag forces. For the measurements taken at 4.2 K this is straight forward: the measured response taken in vacuum at the same temperature (figure 3.7), can be subtracted. As before, it was assumed that the response for mechanical oscillators does not change substantially below 4 K, and therefore the vacuum measurements taken at 4.2 K were subtracted from the values taken at the low temperature limit. A multiplicative factor of 1.19 was used, to ensure that the fluid forces vanish at low velocities.

The drag coefficient of the grid, at 4.2 K and at the low temperature limit, as a function of velocity, with the internal drag forces subtracted are presented in figure 3.9. The fluid drag coefficient in normal fluid, at 4.2 K, is shown to tend towards a constant of approximately 1.6, which is associated with turbulent drag.

The critical velocity, for the sudden onset of turbulence, is shown to be approximately 3 mm/s, in the low temperature limit. The critical velocity, v_c, of an oscillating sphere has been theoretically shown to be $v_c \approx \sqrt{8\kappa f}$ (Hänninen & Schoepe [2008]). For the floppy grid discussed here, this equation results in a calculated critical velocity of approximately 17 mm/s; this is much higher than the

value shown in figure 3.9. However, there is most likely a geometry dependence; the maximum relative velocity between the surface of the oscillating object and the superfluid is an important factor. The grid mesh used in these experiments was very thin compared to it's width and distance travelled; this means that the local superfluid flow around the edges of the grid will be enhanced, reducing the measured critical velocity.

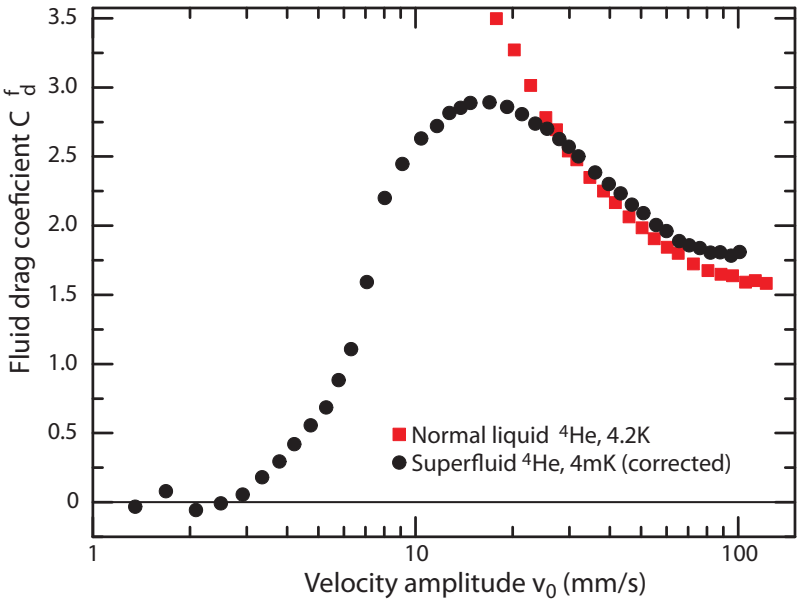

Figure 3.9: A plot showing the drag coefficient of the floppy grid after subtracting the vacuum drag, as a function of velocity amplitude

With the use of the pick-up coils, and the method described in section 3.1.1, figure 3.10 shows the velocity of the floppy grid as a function of the amplitude of the (averaged) drag force for arbitrary driving frequencies. The open circles represent the floppy grid driven on resonance. The data show reasonable agreement between the on-resonance response and the response from the position measurements taken at a range of frequencies. As the drag force remains roughly proportional to the squared velocity, it can be inferred that the drag coefficient remains constant, up to approximately 200 mm/s. The main result taken from this plot is that the response of the grid in the turbulent regime is independent of frequency, over the range from 9 to 100 Hz.

As previously discussed, at higher frequencies the phase shift of the oscillating

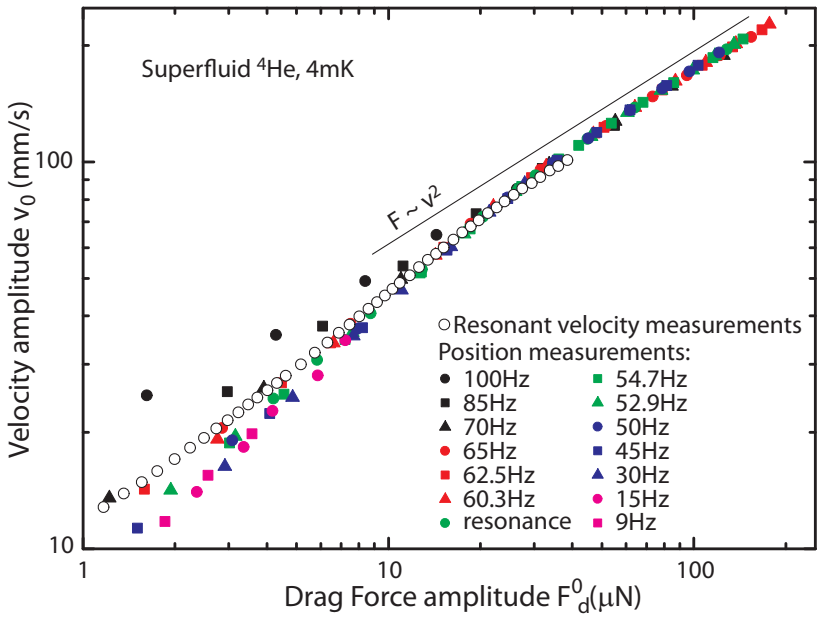

Figure 3.10: A plot showing the velocity of the floppy grid, with varying frequencies between 9 and 100 Hz, with respect to the dissipative drag force, in superfluid helium-4 at very low temperatures.

grid position tends towards 180 °. This results in the small errors in the phase measurement generating large errors in the inferred drag force. Therefore it was not possible to take any measurements using higher frequencies than the ones presented in figure 3.10.

Chapter 4

Linear Motor

The simplest form of turbulence is homogeneous, isotropic turbulence. The closest approximation to this is grid turbulence. In classical fluid grid turbulence experiments, the grid is held stationary with the fluid flowing through it, mostly within a wind tunnel (for examples see Roach [1986] and Hideharu [1991]). Superfluid liquid helium has a very low kinematic viscosity, therefore it is incredibly hard to have fluid flow of any significant velocity and not produce turbulence, with or without a grid present. To stop the helium from flowing past any objects, including the walls of the channel, and therefore producing unwanted turbulence, the grid is moved and the superfluid kept stationary.

A constant hurdle in low temperature experimentation is temperature control; when working at milli-Kelvin temperatures, a very small increase in heat will change the temperature of the cell/experiment by a large percentage. It is therefore desirable that any moving apparatus in superfluid helium does not have any significant frictional forces involved, as these can produce heat. For small scale motion and grids with very small mesh sizes, oscillating devices have been used, such as what was discussed in Chapter 3 (see also Bradley *et al.* [2012], Bradley *et al.* [2011], and Yano [2005]). However if larger mesh values are required, a larger motion is needed to ensure a sufficient distance from the grid ($\gg M$) is available for homogeneous turbulence to develop. The main motivation for using a linear grid however, is the hope that it will produce turbulence which is more

homogeneous and isotropic.

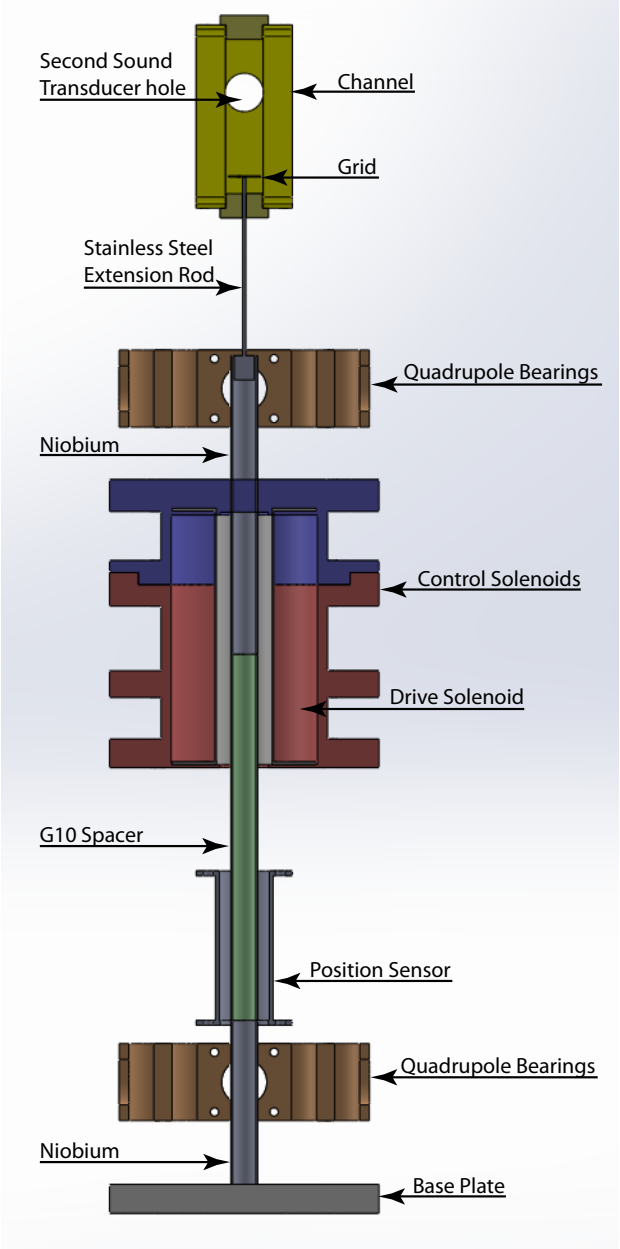

Figure 4.1: SolidWorks drawing of the motor, including the channel, the quadrupole bearings, the position sensor, and the niobium actuator with the extension rod and grid attached. The Second sound transducers and channel are shown, but not discussed in this chapter.

For experiments done at 1 K and higher, a linear motor attached to a pulley system outside of the cryostat has been used (Stalp [1998]), the heat from which is negligible at these relatively high temperatures. However at milli-Kelvin temperatures this type of machinery is likely to create too much of a heat leak. Therefore a linear motor was designed with a levitating superconducting rod which is moved

via electromagnetic repulsion from a magnetic field produced by a solenoid, precluding any mechanical dissipation. The rod, or armature, has a grid attached to one end and is centred using *quadrupole magnetic bearings*; a full schematic of the motor is shown in figure 4.1. The details of this motor are described below.

The channel and second sound transducers are included in figure 4.1, these are discussed in chapter 5; the channel is the experimental volume in which turbulence is produced by the grid, the turbulence decay is then observed using a second sound resonance. The second sound wave and decaying turbulence is discussed in the next chapter.

4.1 Principles of Operation

Superconducting linear motors were developed through a collaboration between Lancaster University and the University of Florida (the details of which can be found in Giltrow *et al.* [2009] and Liu *et al.* [2006]). Both of these motors operate through the same basic principles; magnetic levitation using a superconducting armature, and one or more spatially fixed field coils. Though the practical operations were subtly different, neither of these systems gave the amount of control and velocity stability needed. The earlier linear motors used short solenoids to maximise the field gradient, the next iteration of motor design, known as the *inertial motor*, used one long solenoid achieving a substantial sustained force over time. The principles and theory of the final *control motor* design are a direct continuation from the inertial motor; it is therefore pertinent to discuss the latter before the former.

4.1.1 Inertial Motor

The inertial motor, described fully in Thompson [2012], maintained a magnetic contact with the armature throughout the entire motion. The single solenoid, or the *drive coil*, was 55 mm in length, had a radius of 7.55 mm, and had 4 wound layers of Cu clad NbTi wire. The armature was made up of two pieces of supercon-

ducting material, of lengths 78.6 mm and 43.2 mm (the red parts of the rod shown in figure 4.2), spaced apart by a 96.4 mm piece of fibreglass epoxy material known as G-10 (the blue part of the rod in figure 4.2). The superconductor used was in the form of hollow tubes of 99.9 % pure niobium. The top piece of Nb was placed within the drive coil and used to move the armature. Two quadrupole magnets were used at the ends to centre the Nb and an inductive position sensor was placed at the bottom end, surrounding the lower, second piece of Nb (the position sensor is discussed further on in this chapter). The set-up is shown in figure 4.2.

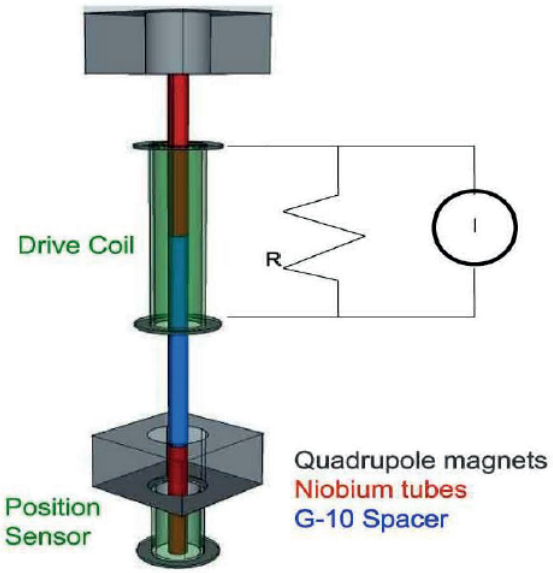

Figure 4.2: Diagram of the Inertial Motor, including a schematic of the shunt resistor placed in parallel.

This was the previous motor used, and the basis for the Control Motor.

The magnetic field, B, generated by the drive coil is approximated by an infinite solenoid approximation:

$$B = \mu_0 n I \tag{4.1}$$

where μ_0 is the permeability of free space, n is the turn density, and I is the current in the coil. The assumed B-field, for an infinitely this solenoid, as a function of z-position is shown in figure 4.3. In reality the end effects of the solenoid will result in a curve to the corners of the field depicted here.

As the Nb armature will already have been cooled well below the critical tem-

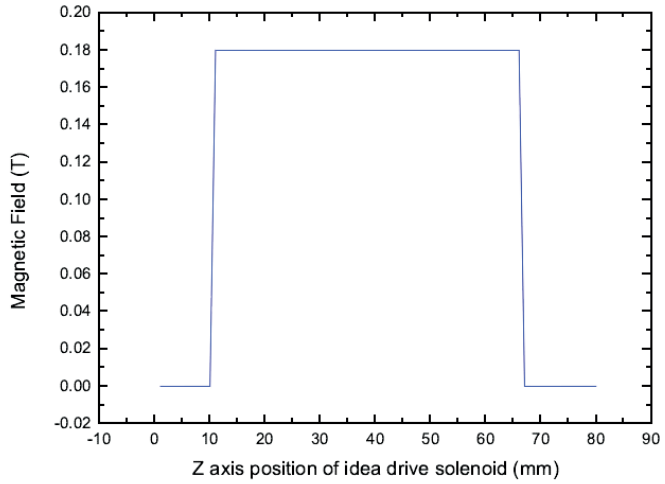

Figure 4.3: Diagram showing the theoretical B-field for the inertial motor, for an ideal case with a perfect, infinite solenoid. Thompson [2012]

perature, T_c, once a current is passed through the drive coil, and therefore producing a magnetic field, the magnetic flux within the armature will be expelled. Through this repulsion, the armature feels a driving force in the z-direction due to the Meissner effect. The magnetic energy displaced by a superconductor is dependent on the magnetic field, the volume of the expelled field, V, and the permeability of free space:

$$E_B = \frac{B^2 V}{2\mu_0} = \frac{B^2 A_x z}{2\mu_0} \tag{4.2}$$

where A_x is the cross sectional area of the superconducting armature, and z is the displacement of the armature within the coil. Given that force, $F = -\frac{d}{dz}E_B$, and integrating along the length of the superconductor, it is possible to show the total force on the armature due to the Meissner effect, assuming that the B-field inside of the superconducting tube is always zero and the upper Nb tube is part way through the drive coil:

$$F_M = \frac{A_x}{2\mu_0} B^2 \tag{4.3}$$

The only dissipative force on the armature is the fluid drag. This cannot be relied upon to sufficiently damp the motion, therefore an additional damping mechanism

is introduced: a shunt resistor, depicted as R in figure 4.2. The fluid drag force, dependent on the cross sectional area (or the area of the attached grid), the density of the fluid, ρ, and the velocity, v, will contribute to the total force; although this is negligible compared to the shunt resistor dissipation. Substituting equation 4.1 into equation 4.3 and including gravity, the final equation for the force on the armature is:

$$F = \frac{1}{2} A_x \mu_0 (nI)^2 - mg \tag{4.4}$$

The Faraday voltage, or EMF, ϵ, caused by the armature moving through the coil will cause a retarding force, directly opposite to the upward force due to the Meissner effect. The EMF is defined as the rate of change of flux:

$$EMF = -\frac{d\Phi}{dt} \simeq -BA_x n \left(\frac{dz}{dt}\right) \tag{4.5}$$

where n is the turn density of the solenoid. Therefore, the power dissipated, $\dot{Q}$, which is equal to the work done, W, of the armature can be written as:

$$\dot{Q} = \frac{\epsilon^2}{R} \simeq \frac{B^2 A_x^2 n^2 v^2}{R} \tag{4.6}$$

where v is the velocity of the armature, and R is the resistance of the circuit. The work done of the system is defined as $W = F_D \cdot v$, and hence the drag force, F_D, can be described as:

$$F_D \simeq \frac{B^2 A_x^2 n^2}{R} \cdot v \tag{4.7}$$

If the resistance of the circuit is small enough, for example by adding a shunt resistor in parallel like the one shown in figure 4.2, then the system will be critically damped.

With no current in the drive coil, the armature rests on a bottom plate. At the start of the motor motion, enough current is sent through the solenoid so that the Meissner force exactly cancels out gravity, i.e. on the brink of motion. After this

is established, the drive coil current is increased to produce a lifting force. By the design of the motor, the armature will accelerate until the Faraday drag exactly cancels out the applied force, after which the motor should move with constant velocity.

Experimental tests were done at 1K, by K.J. Thompson, of single movements of the inertial motor, there was no grid attached to the armature (Thompson [2012]). However the inertial motor could only obtain speeds of about 8 cm/s before oscillations were routinely observed at the end of the motion. This was attributed to a very weak magnetic potential well, as in practise the magnetic profile is not a perfect 'goalpost' shape, in fact there is a very small physical position when the profile is completely straight. Therefore a new design was developed which has a well defined magnetic field gradient, rather than the field itself - the *control motor*.

4.1.2 Control Motor

To have a controllable, variable velocity the new motor needed to allow for a constant rate of change in the drive coil current, while maintaining a large enough potential well so the armature will move smoothly.

The magnetic field inside of an arbitrary coil is defined as:

$$B(z) = \mu_0 n I_C(t) P(z) \tag{4.8}$$

where $I_C(t)$ is the current in the drive coil and $P(z)$ is a function of z describing the strength of the magnetic field. It is now possible to write equation 4.4 in terms of an arbitrary B-field:

$$F = \frac{1}{2} A_x \mu_0 n^2 I_C^2(t) P^2(z) - mg. \tag{4.9}$$

The desired design of the coil is one which $P^2(z) = a_c - b_c z$, where a_c and b_c are approximate constants set by the construction of the coil, the force becomes:

$$F = \frac{1}{2} A_x \mu_0 n^2 I_C^2(t)(a_c - b_c z) - mg \tag{4.10}$$

By integrating the force, it can be shown that the energy is a positive parabolic potential well as a function of z, as opposed to the previous Inertial motor design.

Using the boundary conditions of $z = 0$ and $t = 0$, it can be shown that:

$$I_C(0) = \sqrt{\frac{2mg}{\mu_0 A n^2 a_c}} \tag{4.11}$$

where $I_C(0)$ is the current in the drive coil such that F_M and gravity are in perfect balance. A small increase is current is then applied to the motor such that:

$$I_C(t) = I_C(0) + \gamma t \tag{4.12}$$

The equation of motion, without damping, then becomes:

$$m\ddot{z} = \frac{1}{2}\mu_0 A_x n^2 (I_C(0)^2 + 2\gamma t I_C(0) + \gamma^2 t^2)(a_c - b_c z) - mg \tag{4.13}$$

By ignoring higher order terms, equation 4.13 becomes:

$$m\ddot{z} + \frac{1}{2}\mu_0 A_x n^2 b_c I_C(0)^2 \cdot z = \mu A_x n^2 \gamma a_c I_C(0)^2 \cdot t \tag{4.14}$$

The solution to the above equation is:

$$z(t) = \frac{2a_c\gamma}{b_c I_C(0)} \cdot t + C_1 \sin(ft) + C_2 \cos(ft) \quad \text{where} \quad f = \sqrt{\frac{\mu_0 A_x n^2 b_c I_C(0)^2}{2m}} \tag{4.15}$$

and C_1 and C_2 are constants dependent on the initial conditions; setting the initial conditions $z(t = 0) = 0$ and $\dot{z}(t = 0) = 0$ the solution to the equation of motion becomes:

$$z(t) = \frac{2\gamma a_c}{b_c I_0}\left(t - \frac{\sin ft}{f}\right) \tag{4.16}$$

This describes a linear ramp in z with a sin wave superimposed. The natural equilibrium oscillation frequency, f, defined in equation 4.15, can be matched using a dissipative shunt resistor in parallel with the drive coil, so that the sinusoidal

motions are critically damped. The frequency of the dissipation circuit, R/L, is matched to the mechanical oscillation frequency of the armature. It was found through trial and error that a shunt resistance of $0.1\,\Omega$ critically damped the system.

4.2 Design and Construction

It was decided two solenoids with opposing magnetic fields, coiled around the existing drive solenoid, would give the desired magnetic field profile and therefore the energy potential well needed for stable motor movements.

Using trial and error with multiple calculations in Mathematica, varying the turn density, length and the radius of the outer coils, an ideal arrangement was determined. This arrangement included a centre *adjustment coil*. The arrangement decided upon is shown schematically in figure 4.4, with the drive solenoid in the centre; hereafter the outer coils shall be referred to as *the control coils*. The control solenoids were wound using a coil winder to the specifications described in figure 4.4; the previous 'inertial motor' solenoid was used as the drive solenoid. The three control coils are connected in series and are designed to have the same, constant current.

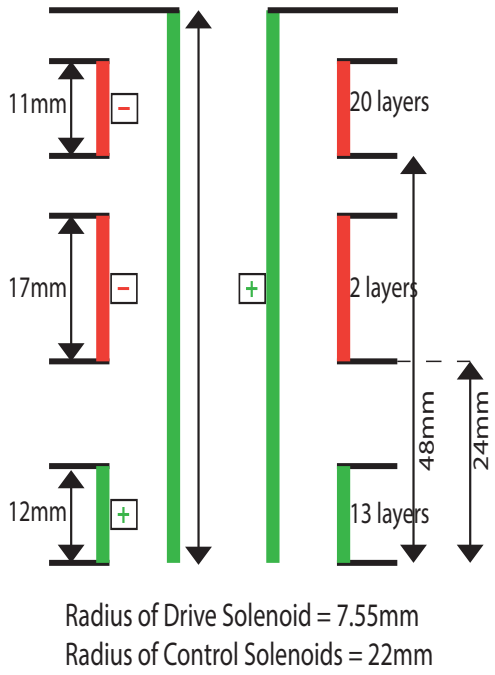

Figure 4.4: A cartoon for the control and drive solenoids design, including dimensions and number of layers in each coil.

Figures 4.5 and 4.6 show the magnetic field profiles for the three separate coils, and the total theoretical magnetic field, respectively. The latter plot shows an

almost constant gradient for approximately 40 mm; the length within the channel, within which the grid can move, is 1.6 in (40.6 mm). Therefore, with a slight allowance for the curve at the ends, a linear input current profile should provide a constant velocity throughout the movement of the armature. Care was taken to ensure that the bottom of the upper piece of niobium was placed so that the actuator only moved within the linear region.

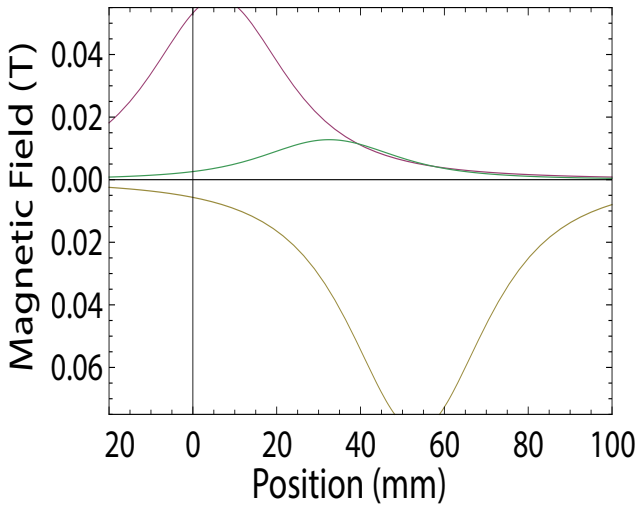

Figure 4.5: A plot from mathematica showing theoretical magnetic fields from each outer coil separately, as a function of z-position.

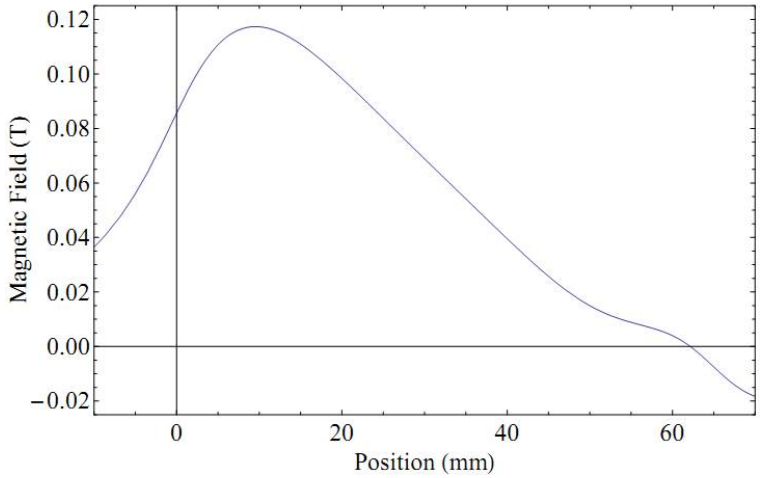

Figure 4.6: Computed magnetic field from all outer, control coils with respect to position, assuming a constant applied current

With this design, the control coils are kept at a constant current and the current

through the drive coil is changed at a linear rate. This results in the Nb armature constantly lying at the bottom of the potential well, while the well itself moves up and down the z-axis, in accordance with the current in the drive coil. Figure 4.7(a) shows a photograph of the fully constructed motor; the drive coil cannot be seen as it is surrounded by the control coils. Figure 4.7(b) is a schematic of the Nb actuator, showing the two superconducting parts, the G-10 spacer, the *extension rod*, and the grid on top. The extension rod is a cylindrical piece of G-10, which attaches the actuator to the grid while still being thin enough to slip through a small hole in the bottom cap of the channel.

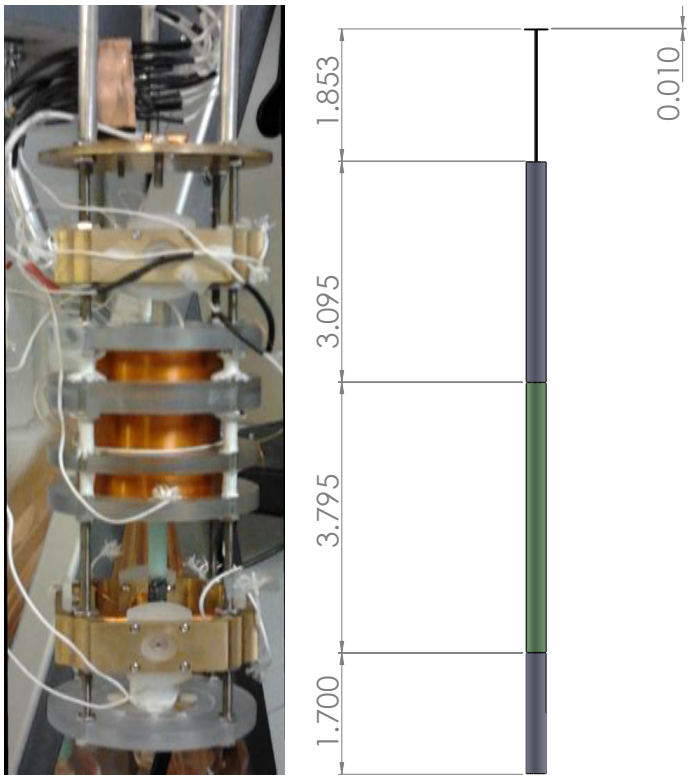

(a) A photograph of the motor, sans channel

(b) The Nb actuator with the extension rod and grid

Figure 4.7: A photograph of the constructed motor (from top to bottom: heat exchanger plate, quadrupole bearing, control coils, bottom quadrupole bearing, position sensor, and bottom plate) and the Nb actuator with dimensions, including the extension rod and grid.

4.2.1 Quadrupole Bearing Magnets

Above and below the coils are the *quadrupole bearings*, each one is comprised of four coils connected in series arranged in such a way so that each opposite coil have the same polarity, as shown in figure 4.8.

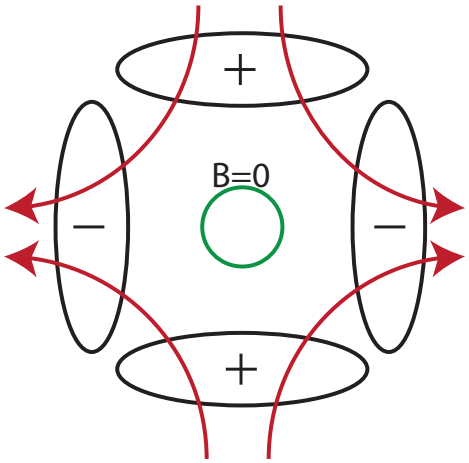

Figure 4.8: A schematic of the quadrupole bearing magnets, with field lines. The positive and negative signs represent polarity.

The purpose of these bearings is to centre the Nb actuator; the magnetic field lines are so that the energetic minimum is in the centre. This means that the superconducting tube will expel the field laterally from the centre, in all directions; resulting in no movement of the actuator in the x or y-axis. Figure 4.9 shows a photograph of the quadrupole bearing magnets used.

4.2.2 The Position sensor

Also shown, at the bottom, of figures 4.7(a) and 4.1 is the inductive position sensor. The position sensor is a 1.5 in superconducting coil, figure 4.10 shows a photograph of the inductive coil. As the niobium moves into, or out of, the centre of the position sensor, the magnetic susceptibility, χ, of the coil changes resulting in a change of the inductance, L:

$$L = (1 + \chi)A\frac{\mu_0 N^2}{l} \tag{4.17}$$

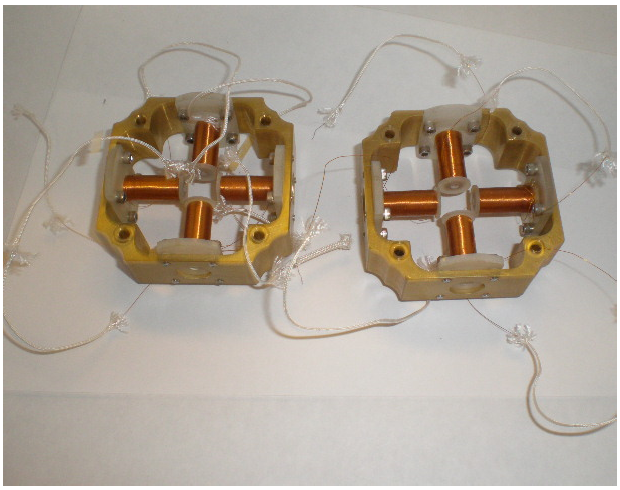

Figure 4.9: A photograph of the quadrupole magnets used to centre the niobium actuator, each coil is screwed into a single brass holder for each set of bearings.

Figure 4.10: A photograph of the 1.5" inductive position sensor, wound with a covering of GE varnish.

where N is the number of turns, A is the cross sectional area, and l is the length of the coil. The change in inductance is then measured and, using a calibration, the position calculated. For the calibration, the inductance was measured using an Agilent 4263B LCR bridge; the calibration data for the inductive position sensor is presented in figure 4.11. The calibration was taken by attaching the armature to a winch with a known turn to length conversion. The winch was turned incrementally, and the inductance of the position sensor recorded.

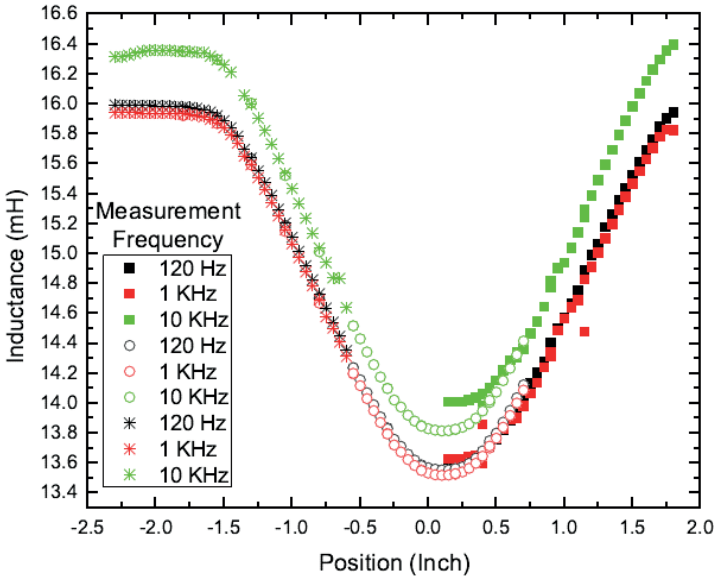

Figure 4.11: The calibration data for the 1.5" inductive position sensor Thompson [2012].
This data was taken by Kyle Thompson using an LCR bridge, three separate frequencies were recorded for each point on the z-axis.

The armature started at the bottom of the position sensor, with the top of the upper piece of Nb in line with the bottom of the coil. As the armature moves further into the coil, the magnetic field inside decreases, and therefore the inductance decreases. Once the armature is completely inside the position sensor, there is a minimum in the inductance, as observed in figure 4.11. As the armature continues to move up, and out of the coil, the magnetic field and inductance return to their initial values.

After the calibration had been recorded, the inductance was measured using a (variation of a) Wheatstone bridge. The reason for this is that a Wheatstone bridge

records the inductance, and therefore the position, to a much higher precision. The electrical circuit for recording the position via the Wheatstone bridge is shown in figure 4.12

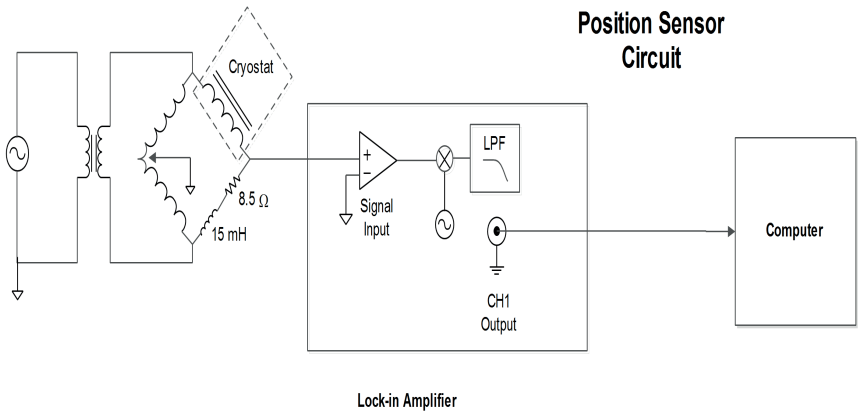

Figure 4.12: The electrical circuit for the inductive position sensor, LPF is a low pass filter.

4.3 Experimental Tests

The motor and other components were submerged in liquid helium inside of a cryostat; using evaporative cooling the cryostat has a base temperature of about 1.2 K. The tests described below were done at this base temperature, without any extension rod or grid attached to the Nb actuator.

The quadrupole magnetic bearings and the control solenoids were supplied with a current using two Harrison 6203B power supplies, the current of which was measured as a voltage across a 0.1 Ω resistor in parallel and recorded using a NI LabView programme, via a National Instruments USB 6009 box. The drive solenoid current supply was controlled manually through the computer and amplified by a Kepco 36-5M B.O.P, again the voltage was measured across a 0.1 Ω resistor and recorded by the software. The output voltage from the Wheatstone bridge, measuring the position sensor, was recorded using the circuit shown in figure 4.12, a Stanford Research Systems SR830 lock-in with a probe frequency of 1 kHz.

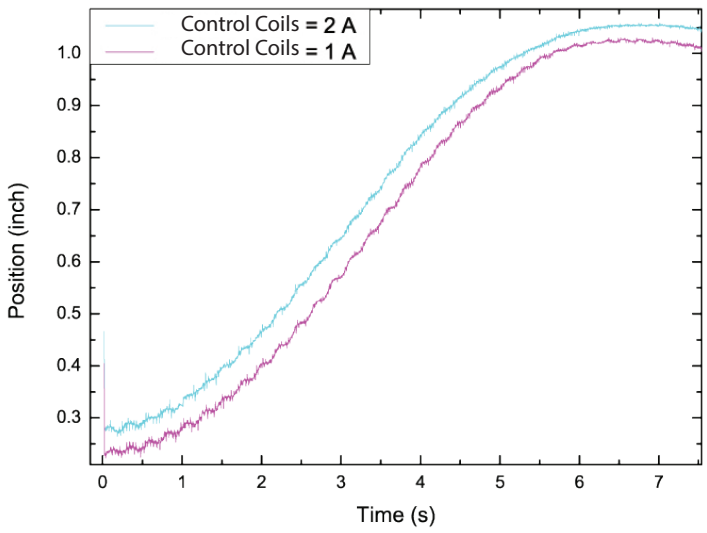

Figure 4.13: A plot showing two similar motions of the motor with 2 different currents through the control solenoids.

A number of different control coil currents and quadrupole currents were in-

vestigated to determine the optimal combination for motor motions. An example of such a test is presented in figure 4.13, for this test a current of 1.5 A was passed through the quadrupole bearings and the same drive coil current linear ramp was used. Through numerous tests and trial and error, it was determined that a quadrupole bearings current of 1.5 A, and a control coils current of 2.8 A were the ideal values for motor motions. A selection of different values for the shunt resistor were also tested; it was determined that a resistance of 0.1 Ω critically damped the system.

Presented in figure 4.14 are different velocities, plotted as position as a function of time, achieved by the motor using the ideal current values discussed above. This plot shows that the motor motion is very smooth, with no oscillations. The highest velocity of 32 cm/s presented here shows oscillations at the end of the motion.

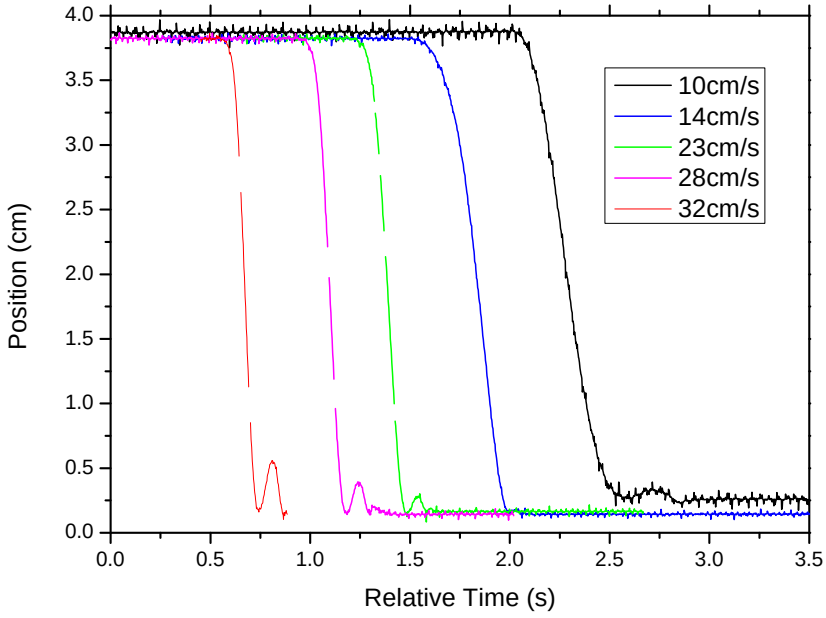

Figure 4.14: A plot showing five different velocities achieved using the control motor, as a position as a function of time. The current applied to the control coils and quadrupole bearing were kept constant at 2.8 A and 1.5 A, respectively.

Figure 4.15 shows the velocity as a function of position for the motions presented in figure 4.14. This plot shows that, even though the motions are smooth and without oscillations, the velocity is not constant for a substantial distance.

The acceleration and deceleration periods are too long.

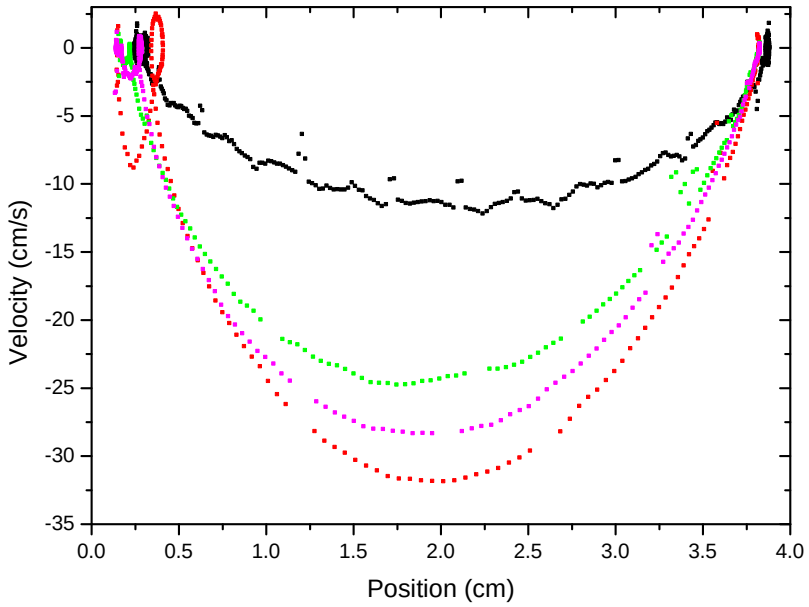

Figure 4.15: A plot showing different velocities achieved using the control motor, as a velocity as a function of position.

These results show that the control motor design produces smooth motor motions with little to no oscillations; although the velocity is not constant throughout. Compared to results presented in Liu *et al.* [2006] and Thompson [2012], it is concluded that the control motor is a better design.

Chapter 5

Second-sound Attenuation

The turbulence is produced in a $1\,\mathrm{cm}^2$ cross-sectional channel within stationary helium-II, by means of a gird moved by the control motor described in the previous chapter. The attenuation of second-sound (SS) is used to calculate the vortex line density, and therefore vorticity, of the decaying turbulence following a single pass of the grid. The SS is excited, and detected, by using oscillating, superleak, capacitive transducers. The channel and transducers are home-made, the detailed drawings for the channel can be found in Appendix A.

5.1 Second-sound Transducers

The inspiration for the basic design of the transducers were found in 1970, Sherlock & Edwards [2003]: an exploded schematic of the final design is shown in figure 5.1. A length of copper clad wire is soldered onto the base of the brass electrode, as can be seen in 5.1, and secured using Stycast 1280 in the protruding part of the channel connection plate. This wire is then attached to the inner core of a coaxial cable, the earth of which is electrically connected to the outer wall of the channel. The channel with the SS transducers installed, including the coaxial cable, is shown in figure 5.2. The inside of the channel (the experimental volume) is 4.1 cm long with a $1\,\mathrm{cm}^2$ cross-sectional area.

The oscillating part of the transducers is a 0.2 mm thick, slightly larger than the brass ring, piece of Sterlitech polycarbonate membrane filter, with $0.2\,\mu$m pores

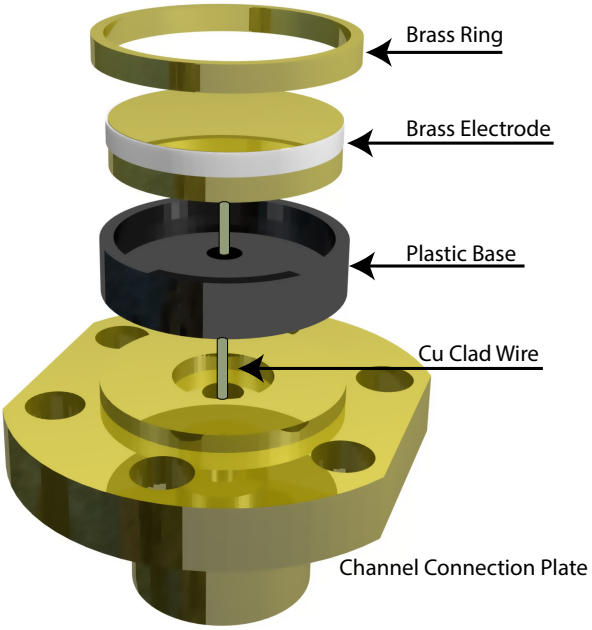

Figure 5.1: An exploded view of the SS transducer design.
From top to bottom: The brass ring, the brass electrode with teflon tape around to insulate from the brass ring, the plastic base, and the channel connection plate.

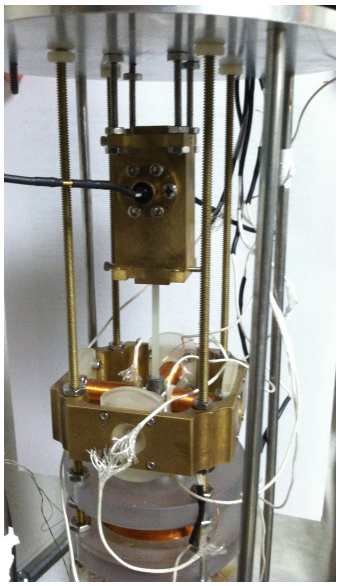

Figure 5.2: A photograph of the channel with SS transducers installed. Shown in this photo is the channel, with the home-made coaxial cable protruding, and the top of the top quadrupole bearing.

and a 500 Å coating of gold. The membrane is attached to the brass ring with Stycast 1266; a slight overlap of membrane is left around the outside of the brass ring which presses against, and therefore electrically connects, to the channel wall once the transducers are inserted. Once the channel and transducers are fully constructed, the membrane is in-line with the inner wall of the channel. When the first set of experiments were carried out, there was a 1 mm gap between the channel wall and the membrane, as in Stalp [1998], though it was found that this caused distortions in the SS wave and therefore the design was changed.

The membrane pressed against the brass electrode along with the outer gold-plated side pressed against the channel wall, create a capacitor. Oscillations of one of the superleak membranes (the transmitter) is induced by applying an AC signal to the brass electrode. As the normal fluid flow is governed by viscosity, this results in the excitation of a second-sound wave propagating across the channel. The second-sound wave induces an oscillation in the second membrane (the receiver), which is situated directly opposite. The AC voltage from the receivers brass electrode is recorded and therefore the SS wave measured. To ensure the membranes only oscillate at the desired AC frequencies, a DC bias voltage is applied to the gold side of both membranes, keeping the membranes taught.

Figure 5.3 shows the full experimental insert, including the motor. The insert is then completely submersed in liquid helium and cooled to the desired temperature by pumping on the free surface. The channel has caps on the top and the bottom, though it is not leak tight; this is to ensure that there is no large scale turbulence which may affect the data. Inside the dewar, all wires used are twisted pairs of teflon coated copper wire, with exception to the transducer wires which are home-made coaxial cables. Outside of the dewar all electrical signals are carried through standard coaxial cables of varying length. Great care was taken to ensure that all grounds were accounted for and sufficient.

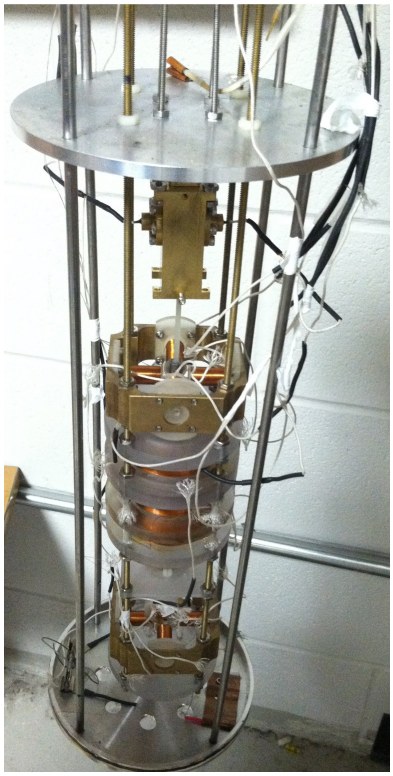

Figure 5.3: A photograph of the complete experimental cell, including the channel with SS transducers installed, the control motor, the quadrupole bearings and the heater base plate.

5.2 Experimental Operation

To be able to record the attenuation of the SS signal, it is first apropos to scan through a set of AC frequencies to find an appropriate SS resonance peak. An AC signal is sent from a function generator to the transmitter, inducing oscillations and therefore a SS wave within the liquid. The receiver then oscillates in response to the induced SS wave, the resulting AC signal from which is picked up by a lock-in, via a pre-amplifier, referenced to the original AC signal from the function generator. A computer records the modulus of the SS signal. Figure 5.4 shows the circuit described, the lock in amplifier used was a Princeton Applied Research 124A and the function generator used was a Hewlett Packard 3325A. The pre-amplifier is home-made.

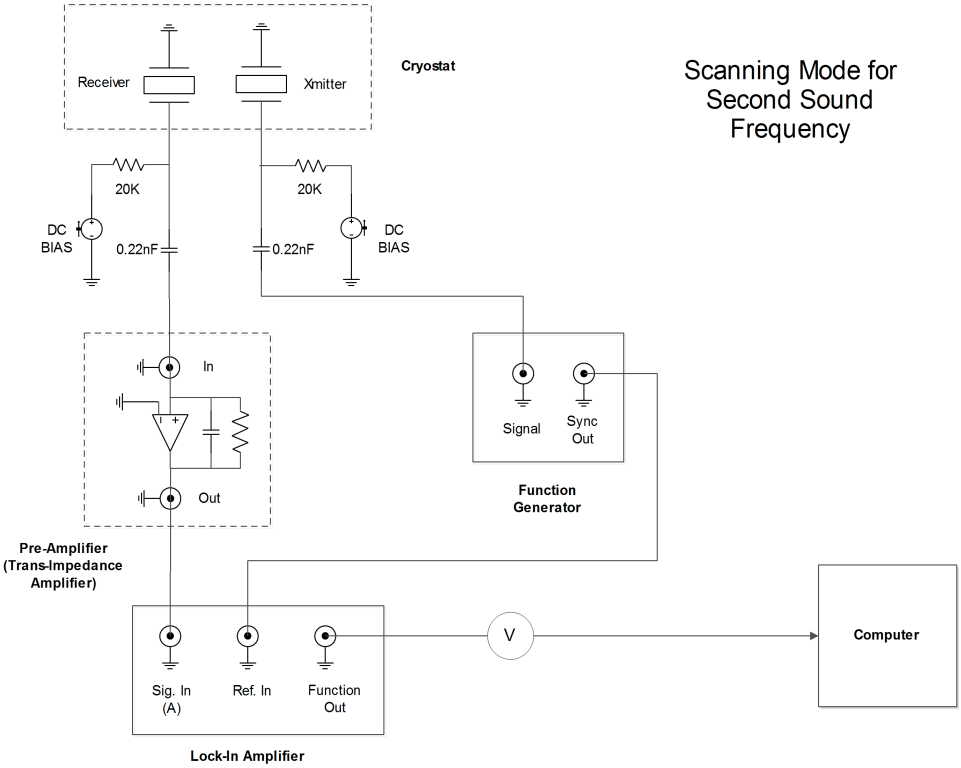

Figure 5.4: Frequency scanning electrical circuit, used to find a resonance SS peak. (JY)

A frequency sweep is controlled remotely using a LabView programme. A plot like the one shown in figure 5.5 is produced and an appropriate peak, the peak within the sweep with the largest *Q-value*, is chosen(for all data taken, the reso-

nance chosen was $23kHz < f_s s < 28kHz$). Another sweep is then taken starting just before, and ending just after, the desired resonance peak. The resulting plot is fitted to a Lorentzian, care is taken to ensure that the phase is correct, and therefore the errors on the fit are small. A single resonance peak and Lorentzian fit are shown in figure 5.6. The centre peak frequency, the *full width at half max* (FWHM), Δ_0, and the correct phase (found through trial and error) are noted from the Lorentzian fit. These values are needed for the SS *tracking* (which is explained in the next section), and for the vorticity calculation described in the last section of chapter 2. The resonances are well reproduced through all temperatures.

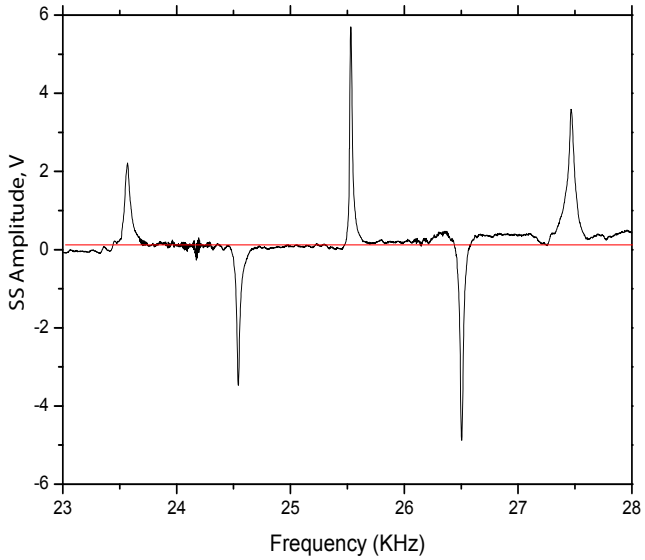

Figure 5.5: A plot of a SS amplitude as a function of frequency showing several SS resonance peaks around the 25^{th} harmonic.

A range of DC bias-voltages and AC voltages were examined, and their resulting SS amplitudes measured to determine the optimal settings. A DC value of 125 V and an AC voltage of 6 V were shown to produce the largest signal, while remaining in the linear regime of the SS amplitude. Figure 5.7 presents the measured SS amplitudes for different AC signals, showing that 6 V is the optimum AC value.

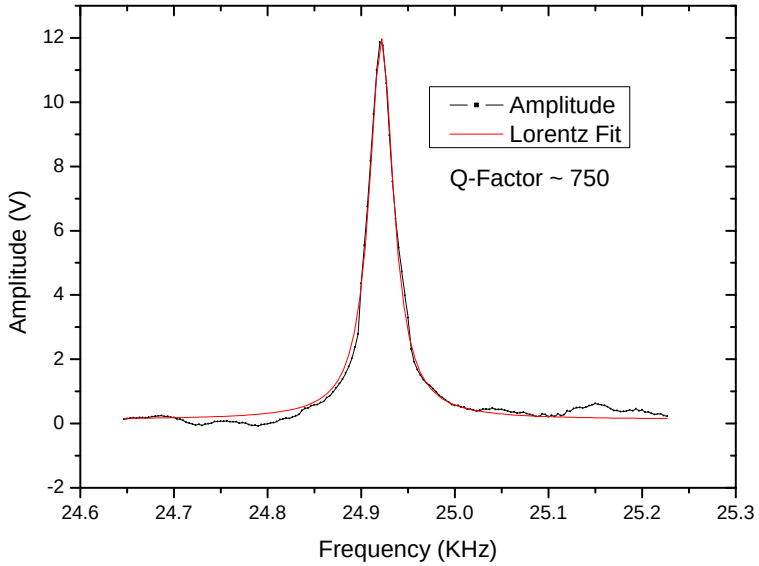

Figure 5.6: A plot of a second-sound resonance, shown as amplitude as a function of frequency, with a theoretically calculated Lorentzian fit over-laid

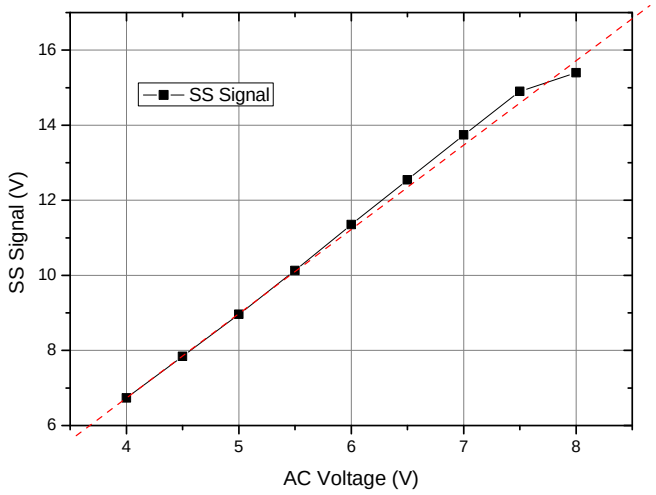

Figure 5.7: SS signal as a function of AC voltage applied to the transmitter transducer, by the function generator. This plot shows a linear relationship upto $\approx 6\,\mathrm{V}$.

It is quite important in any low temperature experiment to have an effective mechanism for controlling and stabilising the temperature to a high degree of accuracy. A heater plate is suspended at the bottom of the apparatus, wound around the diameter of the plate is 15 m of 12.2 Ω/m resistance wire Yang *et al.* [2014]. A platinum RTD 100 resistance thermometer is thermally connected to the top side of the plate; the heater plate can be seen at the bottom of figure 5.3. There is also a ruthenium oxide resistance thermometer placed at the *half way plate*, as is shown at the top of figure 5.3, directly above the channel. The heater plate was also used to hasten the warm-up of the dewar, the mechanism for which is fully described in Yang *et al.* [2014].

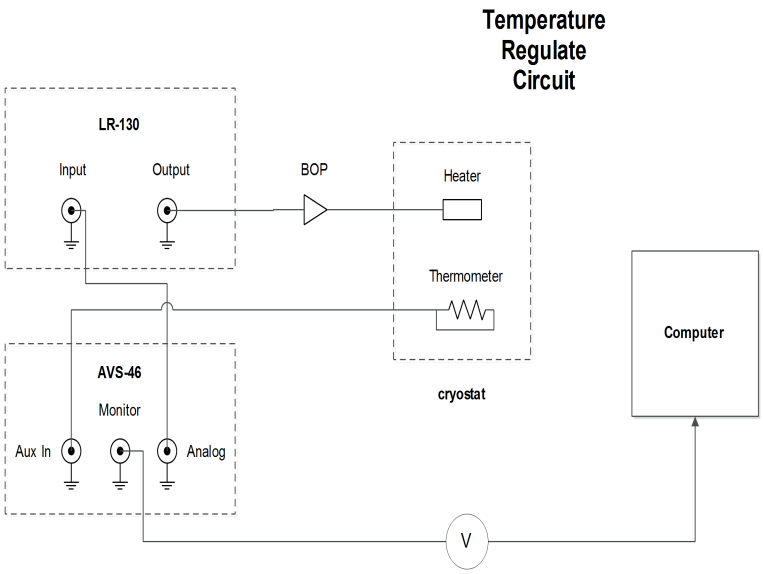

Figure 5.8: The electrical circuit used to regulate the temperature in the helium bath, within the cryostat. (JY)

To achieve and sustain a certain temperature, the electrical circuit shown in figure 5.8 was implemented. The thermometer's resistance is recorded by a RV Elektroniikka Oy resistance bridge AVS-46, the bridge sends an analogue DC signal of the temperature (in K) to a home-made PID LR-130. A Kepco Bipolar Operational Power (BOP) 36-5M receives a DC signal and releases a (adjustable) portion of the current to the heater. The PID is calibrated and the value of the time constant set to optimise the correction of the temperature should it change; it is important to have a quick reaction time as the temperature can change due

to turbulence during experiments. The temperature can also be recorded using a computer as well as simply monitored using the digital screen on the resistance bridge. When the grid is stationary, the temperature is stable to 1 mK precision. During and directly after a motor movement, the temperature fluctuations become larger (up to 10 mK variance) due to ohmic heating from the motor coils; the correction time for these fluctuations vary with the initial temperature due to the temperature dependence of the thermal conductivity of helium-II.

5.2.1 Feedback Circuit

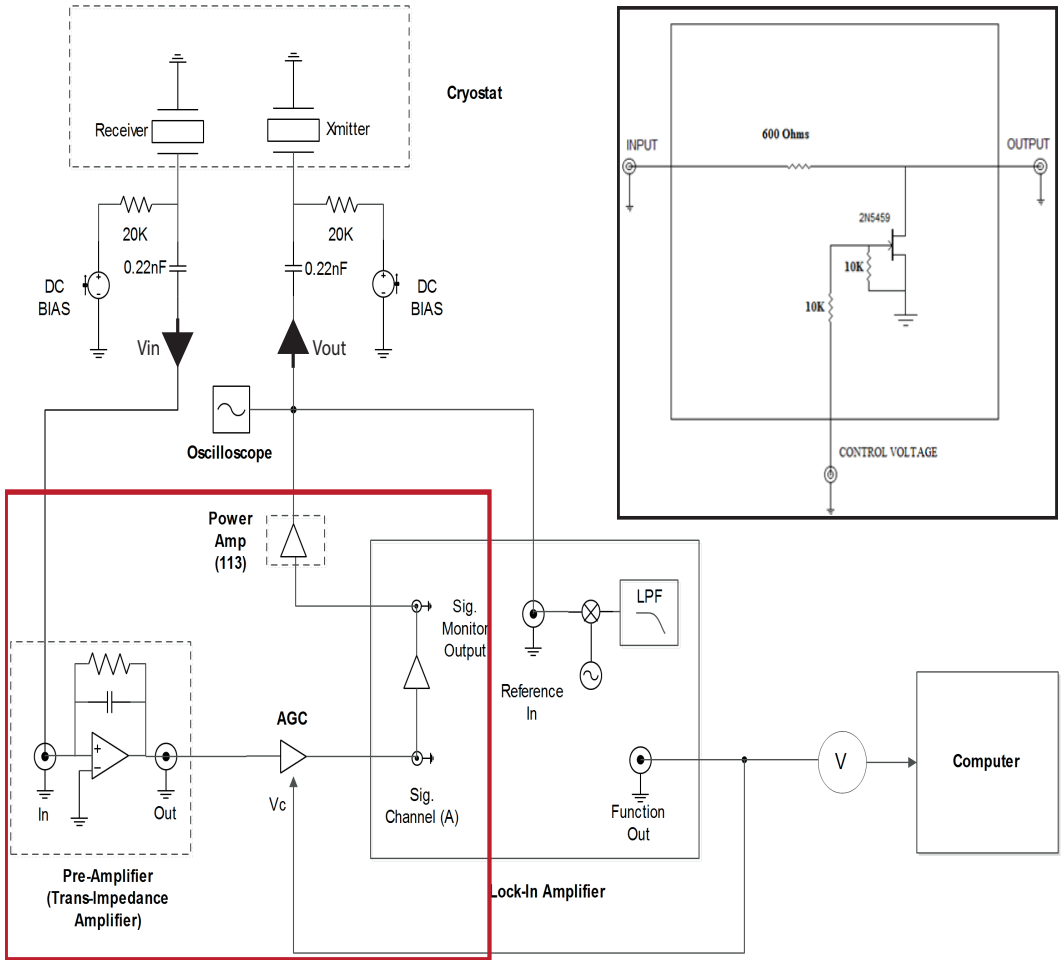

Figure 5.9: second-sound signal feedback circuit, insert shows the circuit within the AGC box. Dotted area represents the cryostat, the red box indicates the gain of the circuit. (LM+JY)

Phenomena which result in a change in second-sound (SS) amplitude can sometimes cause a shift in the resonant frequency of the SS peak, whether it is due to

the slight amount of heat input from moving the motor, or due to the turbulence generated. Therefore it is critical to track the resonance through any increase or decrease in SS attenuation due to turbulence. To do this a frequency-tracking feedback circuit was designed by Dan Ekdahl, an electrical engineer at the University of Florida. The diagram for the electrical circuit is shown in figure 5.9. The lock-in amplifier used is a Princeton Applied Research, PAR 124A, the power amplifier is a PAR 113, and the pre-amplifier and automatic gain control (AGC) are home-made boxes (the circuits for each are shown in the main diagram and the insert of figure 5.9, respectively).

The circuit works by exploiting the two *Barkhausen conditions* for oscillation, with the SS resonance being the source of the oscillations in the circuit. The reader is advised to read Millman & Halkias [1972] for a full understanding on Barkhausen criteria for an analogue circuit; a brief description is given below.

The Barkhausen criterion states that if $G(f)$ is the proportional function (gain) of a circuit, and $H(f)$ is the transfer function of the feedback part of the circuit, then the circuit will sustain steady-state oscillations only if:

- The magnitude of the loop gain is equal to unity: $|H(f)G(f)| = 1$, and
- The phase shift around the loop is zero, or an interger multiple of 2π.

If either of these criteria is violated, the the circuit will correct itself by an increase or decrease in the gain of an amplifier. This means that any loss or attenuation in the system, H, will be exactly compensated for by the proportional error term, G. Both G and H are functions of frequency, f. In practical linear control systems, the ratio of the output voltage, **Vout**, to the input voltage, **Vin**, describes a closed loop process, with the feedback inverted and summed with the input. This is shown mathematically in figure 5.10 and by equation 5.1

$$V_{Out}/V_{In} = \frac{G(f)}{1 + H(f)G(f)} \tag{5.1}$$

In the diagram shown in figure 5.9, $G(f)$ is the area within the red box and $H(f)$ is the dotted box, the second-sound cavity in the helium-II. It should be

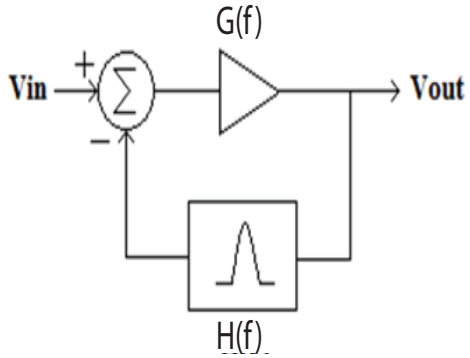

Figure 5.10: Mathematical representation for an electrical circuit with steady-state oscillations

noted that G comprises all of the amplifiers, including the lock-in signal channel. **Vin** and **Vout** are also indicated in figure 5.9 by arrows. Therefore, if the total gain of all the amplifiers exactly equal the inverse of the SS attenuation in the liquid helium-II, such that the product $|H(f)G(f)| = 1$, and the output signal is inverted from the input (180 °), then the Barkhausen criteria for oscillation are both met.

The closed loop circuit that has been set-up has a very high *Q-value* (ratio of resonance peak frequency to bandwidth), resulting in the system always oscillating on a resonance peak. The desired resonance peak is first determined using a frequency sweep, as described previously, and the resulting ideal frequency set on the signal channel dials of the lock-in. The signal channel Q-value is then set to its highest value (100), so the neighbouring peaks are excluded from the loop. If the resonance peak frequency is found to shift substantially, then the signal channel Q-value may need to be lowered once the oscillations are initiated, to allow for adequate frequency tracking; however it was found that this was not necessary. Care is also needed to ensure that the other components of G, such as the pre-amplifier and the power amplifier, do not restrict the bandwidth of the loop in any way.

To initiate oscillations, the lock-in signal channel sensitivity is gradually increased until an appropriate level of gain is found to sustain stable oscillations. It is noted that the oscillations would not start at all without noise or random

fluctuations in the system; the system is designed to find the noise at the desired frequency and amplify it. An oscilloscope is placed just after the power amplifier, to determine when there are steady state oscillations. To ensure a large signal to noise ratio, the loop is operated within the linear regime of the SS signal (the linear regime is explained in the next section). This is ensured by first calibrating the AGC to match the function output of the lock-in amplifier when running within the linear regime.

Turbulence introduced into the helium-II will cause an attenuation in the SS signal, as well as a slight frequency shift; as the turbulence dissipates the SS signal returns to its original value. The output of the lock-in, the value that the computer records, is the DC value of the peak to peak amplitude of the SS resonance; so when there is turbulence, the SS DC signal will be the attenuation. This signal is also fed back to the AGC, which in turn will adjust the gain such that the loop gain always remains unity. This process is separate from the frequency tracking, which is done simply by appropriate settings of the lock-in sensitivity, reference frequency, and Q-value.

5.2.2 Experimental 'run' Procedure

All of the data presented in the next section are averages, mostly over 5 motor movements (or sweeps of the grid). The current in the control coils and in the quadrupole bearings were kept at a constant 2.8 A and 1.5 A, respectively. A complete motor motion consisted of increasing the current in the drive coil, at a set rate, until the grid was as close to the top of the channel as limitations allowed (unless otherwise stated). The motor was held stationary for a set time, at which point the current was decreased at the same rate until the grid had reached its initial position, which is always resting on the base plate. A number of different wait times were investigated for three separate grid mesh designs. The motor was moved using the procedure outlined in chapter 4.

The SS signal and the grid position from one sweep down of the motor is shown in figures 5.11(a) and 5.11(b), respectively. For the purpose of calculating

vorticity and plotting the resulting graphs, a correct and precise zero time, t_0, is very important. t_0 is calculated from the a position as a function of time, it is taken as the physical position within the channel when the grid is at the bottom of the transducers. Therefore all of the attenuation of the SS signal after t_0 is assumed to be only due to quantum turbulence. The zero time with respect to the position and the SS attenuation is indicated on both figures in 5.11 by a red arrow. Care was taken to ensure that the slight variations of the resting position of the grid, both at the top and bottom of the channel, was noted and considered when calibrating the position of the grid, and therefore the zero time point. These variations could be due to shifting resting positions from a warm-up/cool-down or any slight change to the gain on the signal current to the drive coil.

Figure 5.12(b) shows a plot of SS signal against position; figure 5.12(a) shows the raw data of the SS signal and the position as a function of time, the average velocity is 0.4 cm/s. At this speed it is explicitly assumed that there is no turbulence produced by the moving grid. This is done as a verification that the t_0 is taken at the correct position as it shows that once the grid has passed the transducers, any attenuation to the SS signal will not be due to the grid/motor. It also verifies the assumption that there is no attenuation to the SS signal from the grid position before it reaches the transducers, in fact not until the grid is about half way through them. While the grid is up, and past the transducers, the extension rod is attenuating the second-sound signal, as it is physically between the transducers.

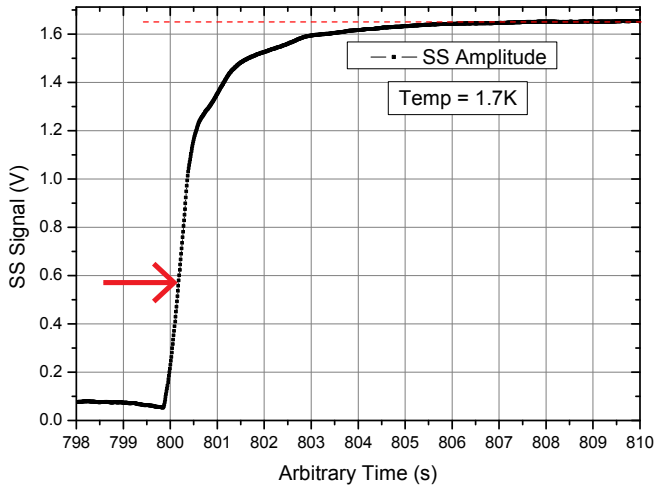

(a) A typical SS signal as a function of time, showing raw attenuation data

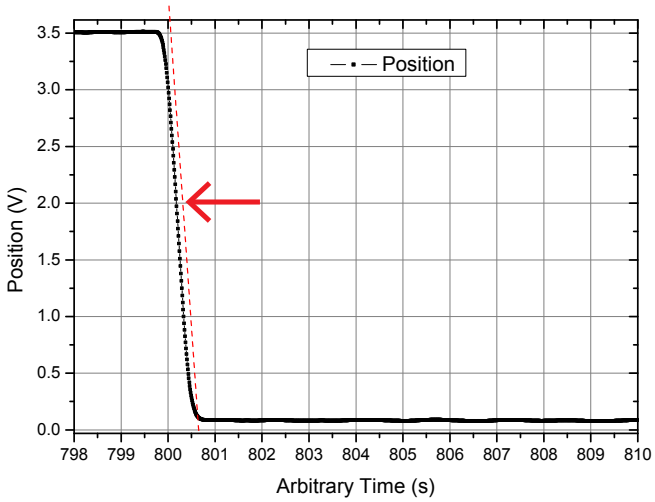

(b) A typical position as a function of time, showing raw motor position data.

Figure 5.11: Typical SS attenuation data with corresponding motor movement. The motor was swept down, past the transducers.

Red dotted lines showing straight lines on both plots, Red arrow indicates t_0

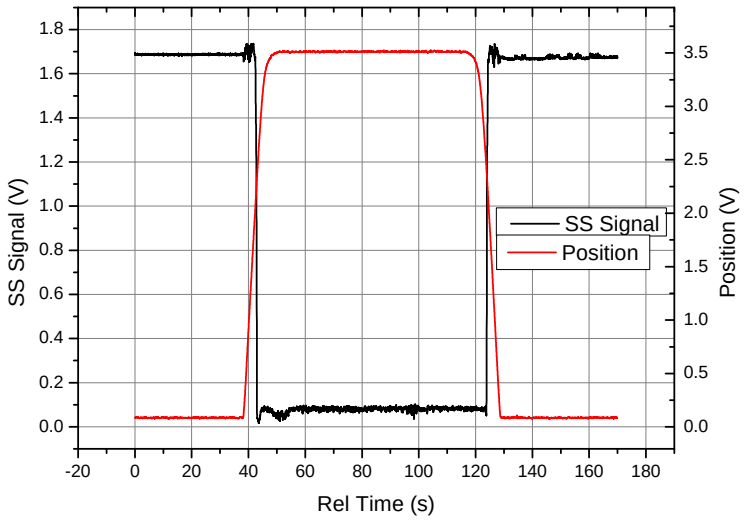

(a) The SS signal and position as a function of time.

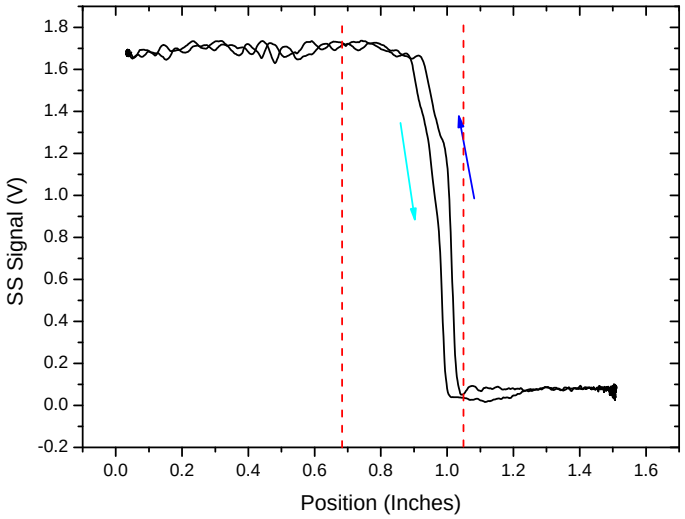

(b) The SS attenuation as a function of position.

Figure 5.12: The SS attenuation as a function of position, with corresponding SS signal and position as functions of time, for a motor sweep up, held for two minutes, then swept back down past the transducers.

Red dotted lines indicating the transducer position, the arrows indicate the direction of the attenuation, for the up sweep and down sweep of the grid, respectively.

5.3 Results and Discussion

Presented in this section are the experimental results for the decay of quantum turbulence. The three different grid meshes used are shown in figure 5.13 (for a photograph of the grid frame with the Lancaster fine mesh attached, please see figure 5.20), the results for each are discussed separately with comparisons made at the end of this chapter. All three grids have an $8.4\,\mathrm{mm}^2 \times 8.4\,\mathrm{mm}^2$ cross sectional area. The distance between the edges of the grid and the inner wall of the channel is 1.6 mm, for each separate grid. The extension rod is connected perpendicularly to the centre of the grids in such as way so that no grid holes were covered or hidden (for Mesh 1, the top of the extension rod fitted into the centre circle). The vorticity has been calculated from the attenuation of the SS signal, using equation 2.29 discussed in section 2.5, the constants for which are taken from Donnelly & Barenghi [1998]. The attenuation at zero vorticity, A_0, also needed for the vorticity calculation 2.29, is calculated by averaging over 1 minute before each separate set of motor motions.

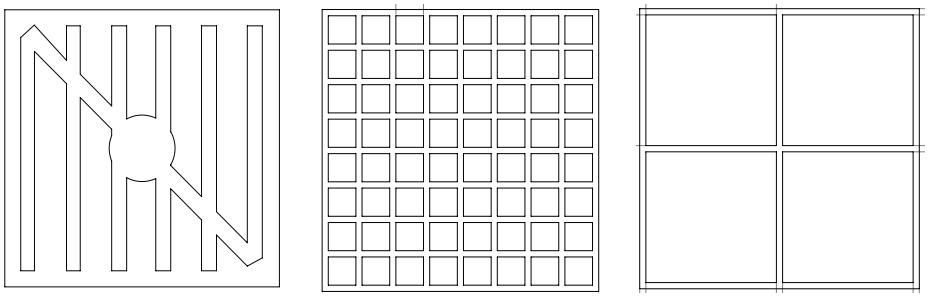

(a) 'Stalp Grid' - Mesh 1 (b) 8x8 Grid - Mesh 2 (c) Frame to hold Lancaster mesh - Mesh 3

Figure 5.13: The three grids used in the second-sound experiments

All vorticity graphs are plotted in log-log scale to appreciate the power law dependencies. Each plot also shows red and green dotted lines representing a $t^{-3/2}$ and a $t^{-11/10}$ relationship, respectively, the explanation for which are detailed below.

The $t^{-11/10}$ dependency is the expected variation when the energy containing length scale is not limited by the size of the channel, and assuming that the early

time turbulence is *Saffman turbulence* - the small wavenumber part of the energy spectrum goes as $E(k) = Ak^2$. By integrating the total energy spectrum in 3D, and using the relationship $\epsilon = \nu\omega^2$, shown explicitly in Skrbek & Stalp [2000], it is possible to derive the expected vorticity decay at early times as a function of time, t:

$$\omega_<(t) = \left(\frac{11}{5}\right)^{11/10} \frac{C^{9/10}A^{1/5}}{\sqrt{\nu'}}(t+t_0)^{-11/10} \tag{5.2}$$

where D is the width of the channel, ν' is the kinematic effective viscosity, C is the Kolmogorov constant (=1.5), and t^* is the time needed for the decaying vorticity to reach saturation (Stalp [1998] and Chagovets *et al.* [2007]). The reader is reminded that saturation is assumed to be the point when the energy containing length scale is fixed at the size of the channel, i.e. $l \propto D$.

Once the energy containing vortices reach saturation, at the size of the channel, the vorticity decay as a function of time changes. This also assumes that there is a finite wavenumber for which the energy will be completely dissipated.

$$\omega = \kappa L = \frac{D}{2\pi\sqrt{\nu'}}(3C)^{3/2}(t+t^*)^{-3/2} \tag{5.3}$$

The effective kinematic viscosity arises from the difference between a classical turbulent system and a *quasi-classical* turbulent system. Liquid helium-II in the temperature range $1K < T < T_\lambda$ follows the two fluid model, described in chapter 2. On length scales larger than inter-vortex spacing, l, the normal fluid and superfluid components can act as a single fluid with a Kolmogorov spectrum; thus a temperature-dependent *effective* kinematic viscosity is allowed (Vinen & Donnelly [2007]).

It is also argued in Skrbek *et al.* [2000] that there are two other possibly observable regimes in the vorticity decay. However it was felt that the data obtained by the experiments discussed in this chapter were not clean enough to attempt an analysis to investigate these other two regimes.

5.3.1 Mesh 1 - 'Stalp Grid'

The design for this grid is the same as the grid described in Stalp [1998], though it was originally published by Smith *et al.* [1993]. As the goal of this set of experiments was to investigate the effects of different grid meshes on the line density of decaying turbulence, it made sense to at first try to reproduce results previously published (Skrbek *et al.* [2000], Stalp & Niemela [2002], and Stalp [1998]).

Figure 5.14 shows the vorticity as a function of time for Mesh 1 at a temperature of 2.0 K. The data acquisition rate for these data was 24 pts/s, though those points were collected in 6 equally timed *packets* of 4 pts. The reason for this was an unfortunate problem encountered while programming the data acquisition software; the problem was rectified during experiments with Mesh 2. Due to time constraints this data for Mesh 1 was not re-taken after the appropriate programming solution was implemented.

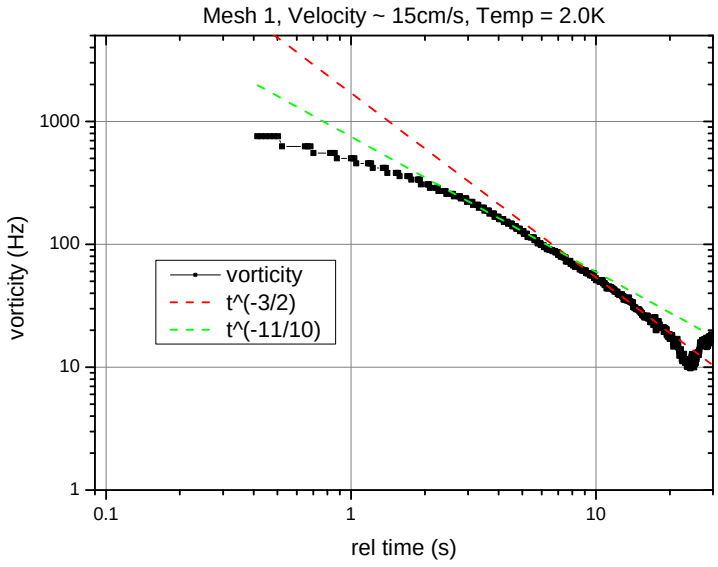

Figure 5.14: A plot showing the best vorticity data obtained with Mesh 1, as a function of time.

The wait time, the time the motor rested before sweeping back down past the transducers, was 5 minutes for this data set, though after 30 seconds the vorticity

becomes just noise, as the turbulence has completely decayed and the SS attenuation has returned to its initial value. A comparison of this data, along with similar plots from Mesh 2 and Mesh 3, with a plot from Stalp *et al.* [1999] is shown in figure 5.33, section 5.3.4.

As previously discussed, t_0 was determined from the time that the grid was at the bottom of the transducers, as deduced from the motor position sensor signal, discussed in section 4.2.2. It took approximately 60 ms for the grid to pass the transducers, this small amount of time would have no effect on the shape of the vorticity curve, a shift of 0.5 s would be needed to see a significant difference.

The data presented in this section, with Mesh 1, are very preliminary data and therefore only one sample is presented. It was decided that the vorticity curves calculated from grid motions using Mesh 1 are not entirely accurate and cannot be characterised, and therefore no conclusions drawn from them.

5.3.2 Mesh 2 - '8x8 Grid'

Mesh 2, shown in figure 5.13(b), has the same transparency as Mesh 1: 67%. The data acquisition was 100 points per second, the experimental procedure used for each of these plots in this section was as described previously.

Figure 5.15(a) shows the temperature dependence for vorticity decay as a function of time, using Mesh 2 to produce the turbulence. The motor was held in position for one minute before it was swept back down past the transducers. This plot shows that there is no discernible temperature dependence.

The highest velocity, occurs as the motor passes the transducers and is approximately 15 cm/s. Figure 5.15(b) shows the velocity of the grid versus position. The data shows that while the grid is passing through the transducers, the velocity is approximately constant. Figure 5.15(b) also shows that there is no temperature dependence of the velocity of the grid.

Unfortunately, the velocity of the motor motion is not as uniform as would be ideal. This may be due to the *extension rod* used to connect the Nb actuator to the grid. It slightly sticks to parts of the hole through the channel cap, as it passes

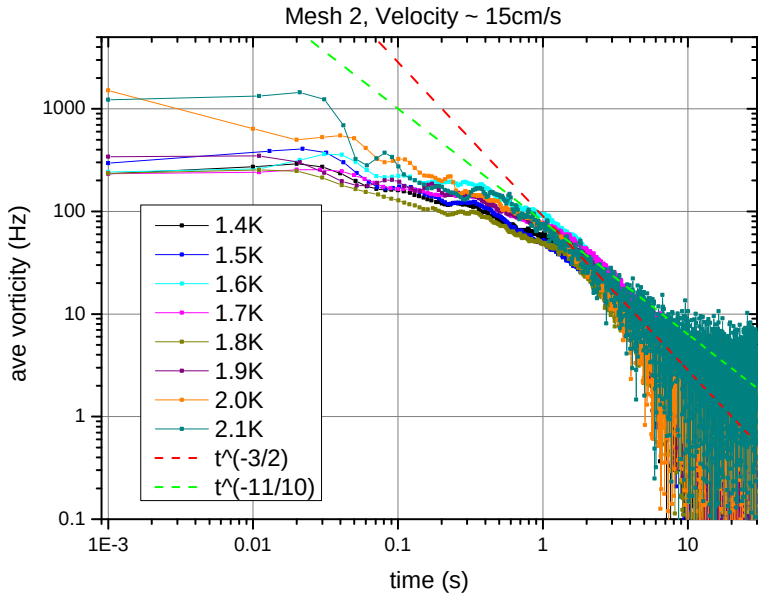

(a) Vorticity Plot

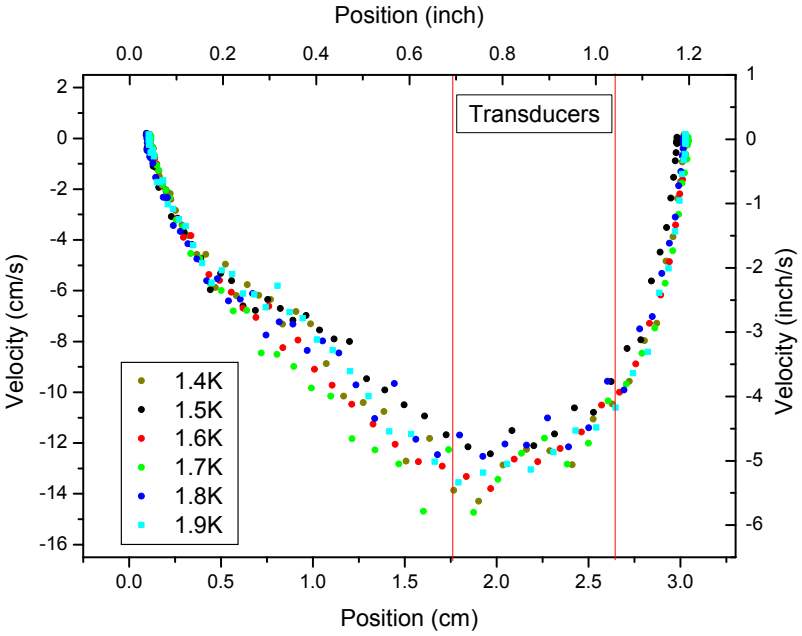

(b) Velocity vrs Position (JY)

Figure 5.15: Temperature comparison plot of the vorticity curves as a function of time, and the corresponding velocity as a function of position, for 1 minute wait times. Mesh 2, fastest velocity.

back and forth. It is believed that this is also the reason for slower speeds than the initial tests on the motor demonstrated.

When the motor itself was being first tested, the extension rod was cylindrical in shape. However, the grid membranes were consistently being torn by the corners of the grid, as the grid rotated around the z-axis. Therefore a rod with a cross-shaped cross sectional area (a photograph of which can be found in the appendix) was used. A cross-shape was chosen to try to reduce the volume of the extension rod as much as possible, whilst blocking a smaller amount of the mesh.

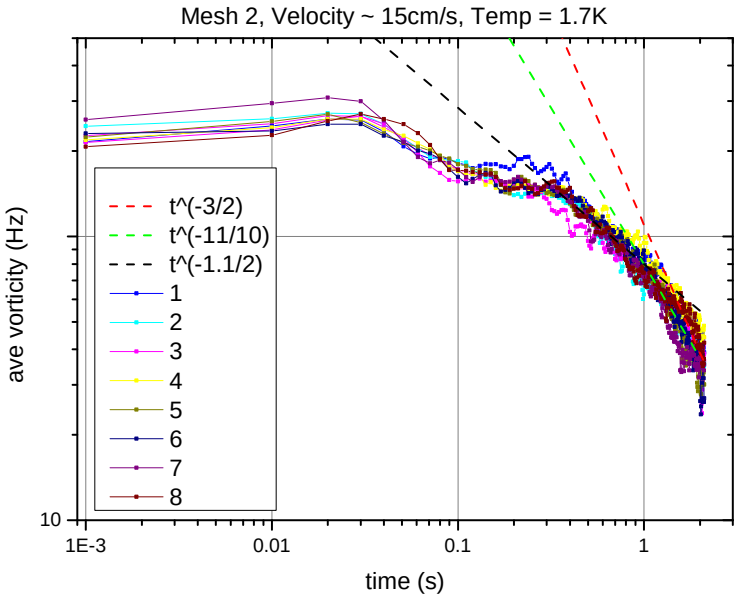

Figure 5.16: A plot of the vorticity as a function of time for 2 second wait times, taken sequentially with mesh 2, with the fastest motion. This plot shows the reproducibility of the vorticity curve, even with such a short wait time.

Figure 5.16 shows the vorticity decay as a function of time for Mesh 2 at 1.7 K when the motor was only allowed to rest for two seconds, before it was swept back past the transducers. In addition to the red and green dotted lines representing $t^{-3/2}$ and $t^{-11/10}$, respectively, a black dotted line representing $t^{-1.1/2}$ has been included. As two seconds is considered not enough time for all of the turbulence to be saturated, shown by figure 5.16, a relationship was determined which fit the earlier time; this was done by trial and error.

Figure 5.16 shows individual, sequential runs. This plot shows that, even though the grid was only allowed to rest for two seconds, any remnant vortices had sufficiently dissipated, and subsequently had no noticeable affect on the turbulence

caused by the following sweep.

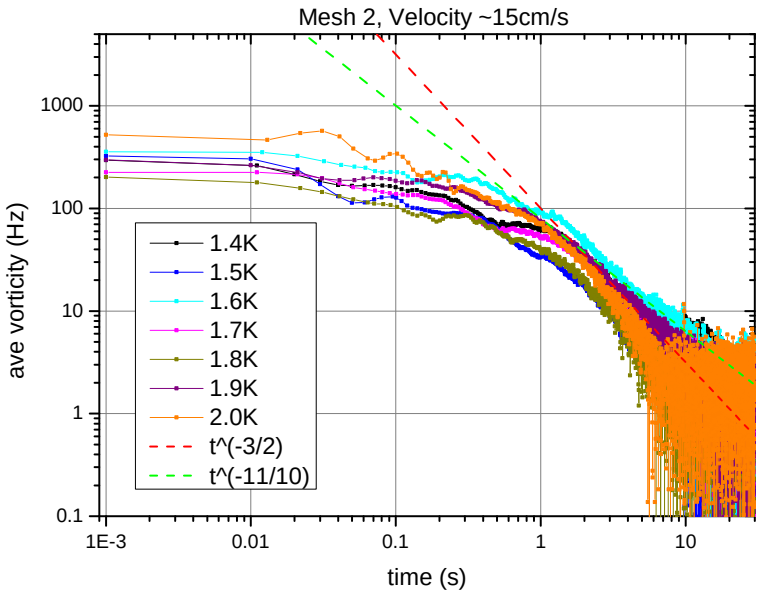

Figure 5.17: A temperature comparison plot of the vorticity decays as a function of time, with mesh 2, for the fastest motion at various temperatures

The vorticity plot as a function of time shown in figure 5.17 was calculated from the second-sound attenuation using Mesh 2, with a thirty second wait time after moving the motor up, and then ten minutes after sweeping down. The final wait time was used to see if there was any long lived vorticity produced, which would be seen as any secondary attenuation after the initial decay: there was no sign of this. Figure 5.17 also shows that there is no temperature dependency for the decay of vorticity, just as was reported in Stalp [1998] (figure 26, page 96), also stated in Skrbek *et al.* [2000]. Comparing figures 5.15(a), 5.16, and 5.17 shows that the wait time of the grid has no affect on the vorticity curves.

Some other groups (Chagovets *et al.* [2007]) work with much lower SS resonant frequencies than the 25 kHz which were used for the data presented in this chapter. Figure 5.18 shows vorticity as a function of time using a much lower (12 kHz) resonant peak frequency, using Mesh 2 and still with a velocity of approximately 15 cm/s. The plot shows the same temperature independence as the previous plots in this section.

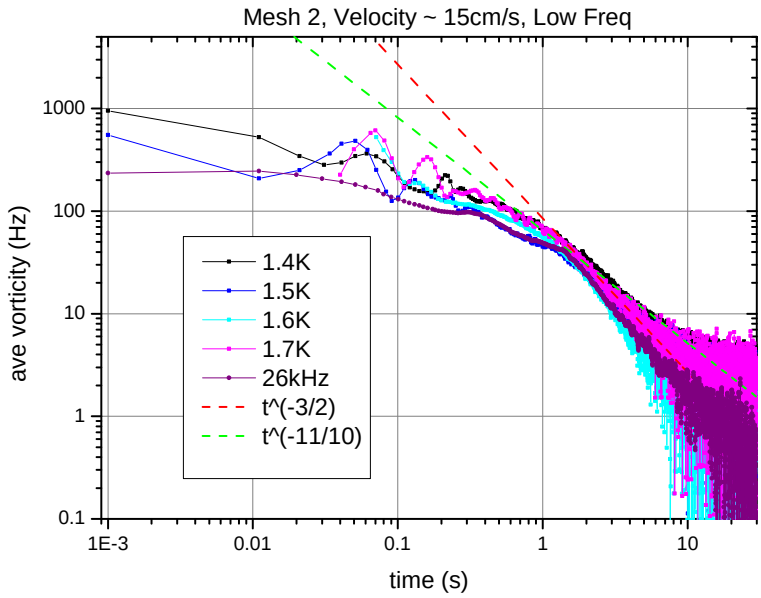

Figure 5.18: A temperature comparison plot of the vorticity with mesh 2, using a lower frequency SS resonance (≈12 kHz as opposed to 25 kHz), for the fastest motion. A curve taken using 25 kHz is also included.

Also included in figure 5.18 is the vorticity curve taken from a motion using a SS peak of 26 kHz, for comparison. This shows that the vorticity curve does not depend on SS frequency; this is as expected.

Figure 5.19(a) shows the vorticity decay as a function of time, for different temperatures, using Mesh 2 at a much slower speed. This plot shows that at this velocity the inertial ($t^{-3/2}$) range is much less discernible. This may be due to an insufficient amount of energy at M^{-1} wavenumber, for the turbulence to reach saturation before it decays. Figure 5.19(b) shows the velocity as a function of position for the much slower motions. The velocity is much more constant, which agrees with the hypothesis that the extension rod is sticking as it moves. A comparison of the two separate velocities is presented for Mesh 3 in the next section, figure 5.27.

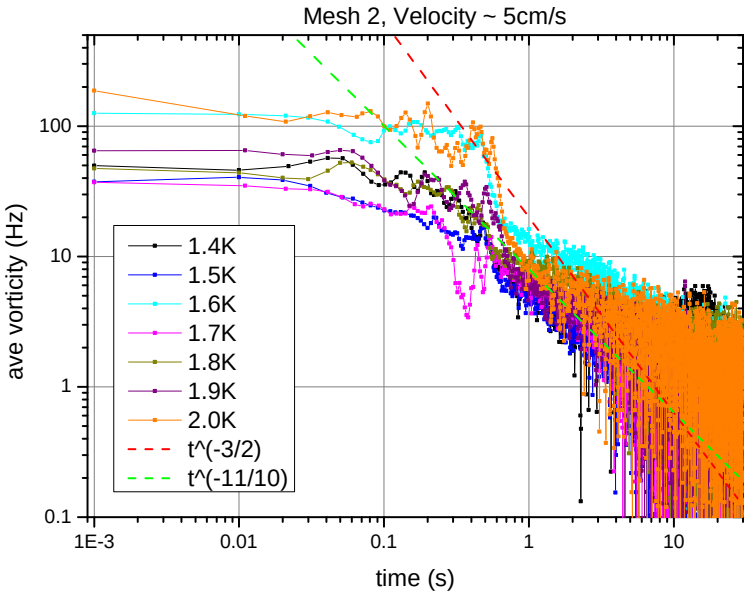

(a) Vorticity as a function of time at a lower velocity, with Mesh 2

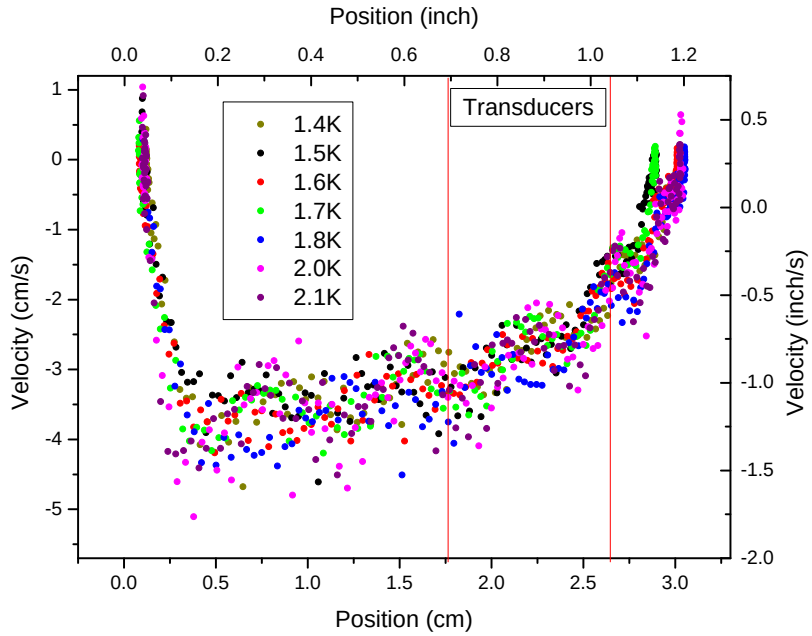

(b) Velocity as a function of position for lower velocity, with Mesh 2 (JY)

Figure 5.19: Temperature comparison plot of the vorticity as a function of time, and the corresponding velocity as a function of position; Mesh 2, with a much slower velocity.

5.3.3 Mesh 3 - 'Lancaster Grid'

Mesh 3 was chosen as a dramatic mesh hole size difference compared to Meshes 1 and 2, the transparency for this mesh is just a little different at 55%. Figure 5.20 depicts the small mesh attached, using small amounts of Stycast 1266, to the frame (as shown in figure 5.13(c)) compared to the 8 x 8 grid. Mesh 3 is approximately 1 μm thick, the holes are 23 μm wide and are separated by 11 μm copper strips; it is the same mesh as was used in the experiments described in chapter 3. Great care was taken to ensure that the Stycast used to attach the mesh to the frame was only between the two, and no mesh holes were blocked by the epoxy.

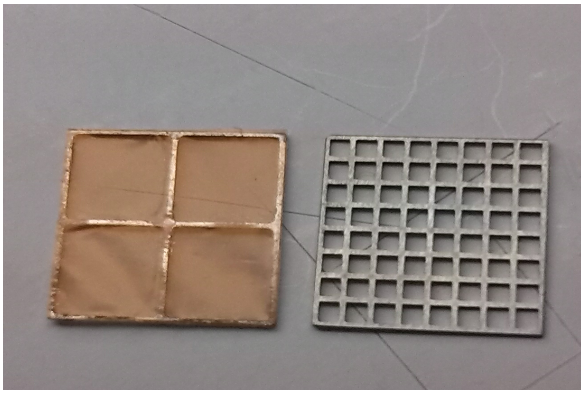

Figure 5.20: A photograph of the Mesh 3 grid (left) next to the 8x8 grid, Mesh 2 (right)

All of the vorticity plots presented in this chapter are averaged over at least five motor motions. To demonstrate the standard deviation, figure 5.21 shows all five motions, and the average overlaid. The data are typical of all plots and it proves the reproducibility of SS attenuation data.

Figure 5.22(a) shows the vorticity decay plot for Mesh 3 for the fastest motions, for various temperatures. There seems to be slightly more variation in both the vorticity level, and the transition time to the inertial range. It is unclear as to why this is so, it is not a temperature dependence as the vorticity curves do not fall sequentially throughout the temperatures. One explanation for this would be the SS feedback circuit not running in the linear regime, resulting in a slight offset in the SS signal. However as the equation is dependent on A/A_0, any offset should have

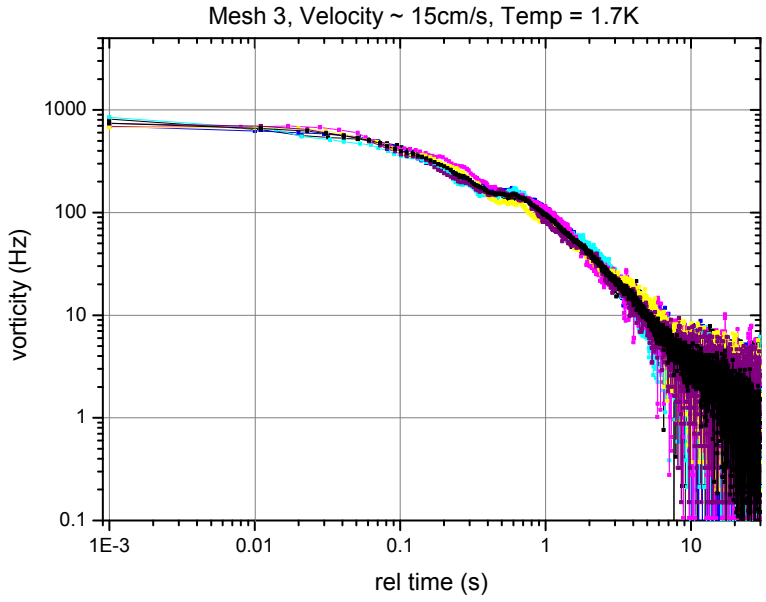

Figure 5.21: The average vorticity shown with the 5 single, sequential data sets for each motor motion, with mesh 3 - showing reproducibility.

been accounted for. Another explanation for this could be an unexplained offset on the National Instruments current box, which is used to convert analogue signals from the circuit to digital signals to be interpreted by the computer software.

A possible cause for the discrepancy to investigate could be the time of the day the data were taken. For the temperatures of 1.6 K, 1.8 K, and 2.0 K the data were taken in the afternoon, just after lunch-time. On the other hand, the temperatures of 1.5 K, 1.7 K, and 1.9 K the data were taken either in the morning, or late at night. The busiest part of the day, both for amount of people and other experiments working, is mid-afternoon; therefore there may have been external interference which was otherwise undetected during the runs.

Figure 5.22(b) shows the velocity as a function of position, for different temperatures, corresponding to figure 5.22(a). As for Mesh 2, it is clear that as the grid is passing the transducers the motor is moving at its highest velocity, the velocity is also approximately constant in this region. However, also as before, the velocity was not constant throughout. It is thought that this inconsistency could also be a contribution to the slight variation in the vorticity curves shown in figure 5.22(a),

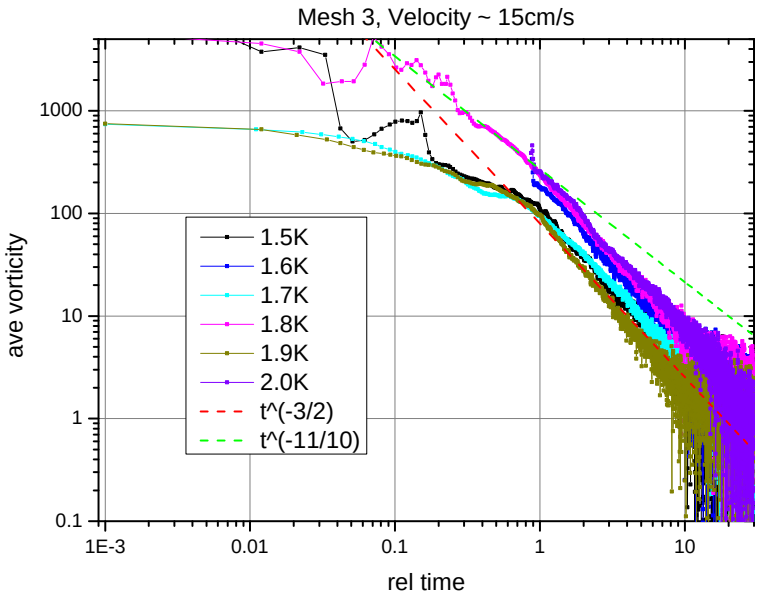

(a) Vorticity Plot

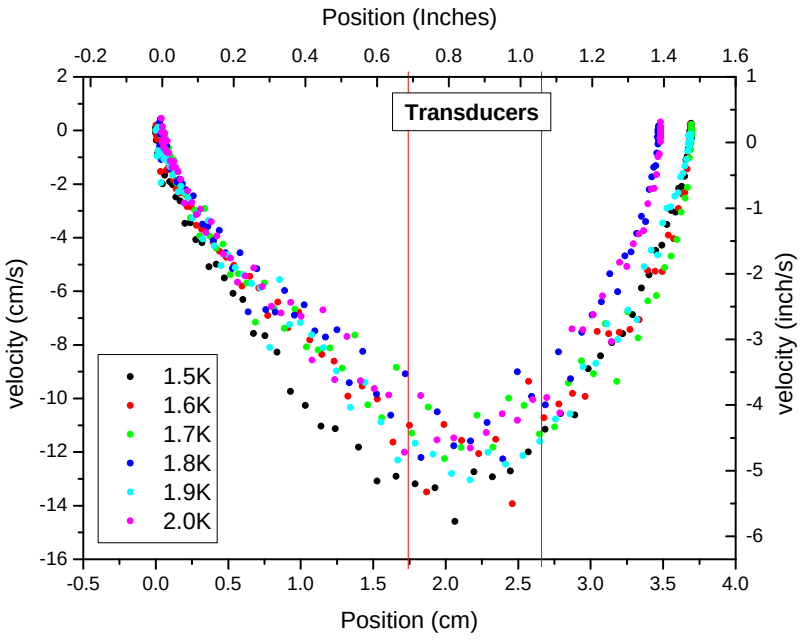

(b) Velocity vrs Position (JY)

Figure 5.22: Temperature comparison plot of the vorticity as a function of time, and the corresponding velocity as a function of position, at the highest velocity.

although the velocity curve is the same for all temperatures. A comparison of all three meshes, with the same wait time and temperature can be found in the next section, figure 5.32.

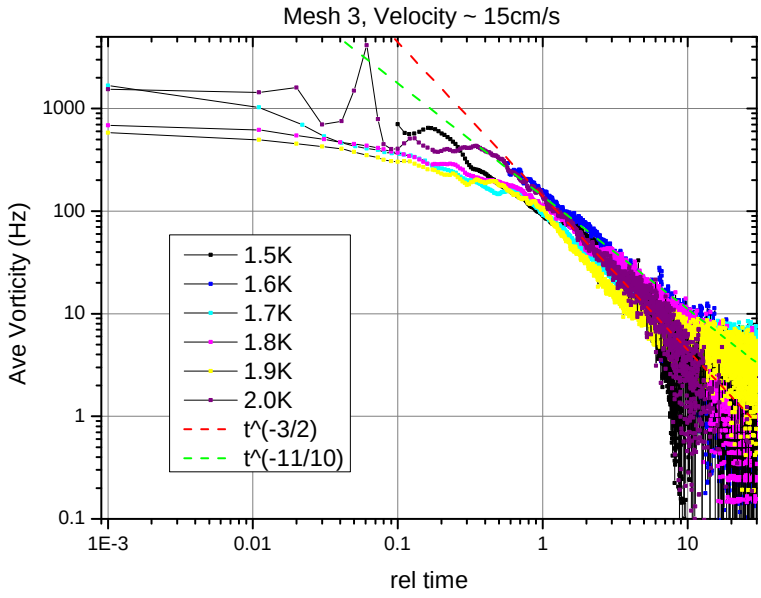

Figure 5.23: A temperature comparison plot of vorticity as a function of time, with mesh 3 and the fastest motion.

The vorticity plot shown in figure 5.23 was produced from motor motions using Mesh 3, with 30 s wait after moving up (to ensure all turbulence has dissipated from that movement) and 10 min wait time after. As for Mesh 2, no large scale turbulence was observed. Figure 5.23 also shows no temperature dependence for the vorticity curve.

To continue on from figure 5.18, showing no temperature dependence for motor motions using Mesh 2 with using a much lower SS peak frequency, figure 5.24 is presented. This plot shows a comparison between motor motions using 26 kHz and 12 kHz, both curves were measured with a motor velocity of approximately 15 cm/s. The two curves on this plot clearly show the same time for saturation, proving again that there is no dependence on the SS resonance peak.

Figures 5.25(a) and 5.25(b) show the vorticity as a function of time and the velocity as a function of position, respectively, for Mesh 3 motions at a much lower velocity. Again, there is no temperature dependence, and the grid velocity through the transducers is fairly constant. As opposed to the slower motions with Mesh 2, shown in figure 5.19(a), there is a discernible time at which the turbulence reaches

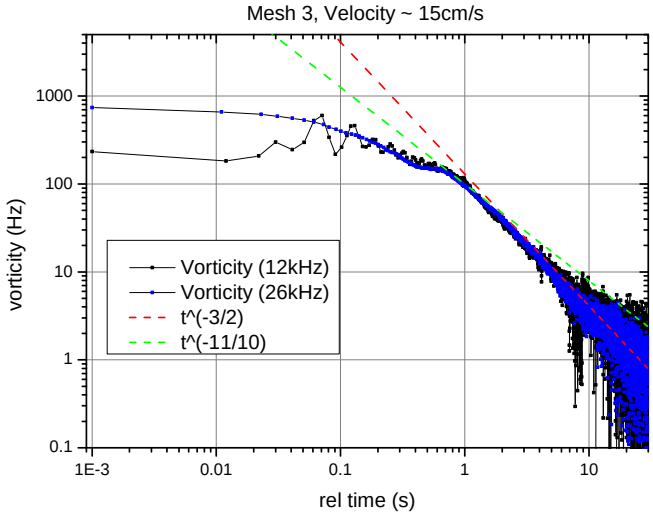

Figure 5.24: A plot showing the averaged vorticity with a transducer driving frequency of 12 kHz and 26 kHz, with mesh 3

saturation. This is better illustrated in figure 5.26, which shows vorticity curves for motor motions using Meshes 2 and 3, at 1.9 K. It is thought that this is because there are more vortices at the energy injection scale, M^{-1}, at t_0. With more vortices produced, there are more re-connections possible, and so the turbulence can grow more quickly. This is supported by the values for t^*, shown in figure 5.38 in the next section.

This is the opposite of what would be expected considering the energy spectrum described in section 2.2.1 and depicted in figure 2.8. The energy spectrum shows that the smaller the energy containing vortices (or eddies), the longer it should take before these vortices reach the size of the channel, D. This is further discussed in the next section.

Figure 5.27 shows a comparison of vorticity curves for the two different velocities discussed in this chapter. This plot shows that both curves reach the $t^{-3/2}$ regime, but the turbulence produced from the lower velocity reaches the saturation point about three seconds later than the faster motion turbulence. It should also be noted that there is no discernible $t^{-11/10}$ region.

The vorticity curve comparison presented in figure 5.27 is an important verification for the model stated earlier. It is to be expected for all decaying turbulence

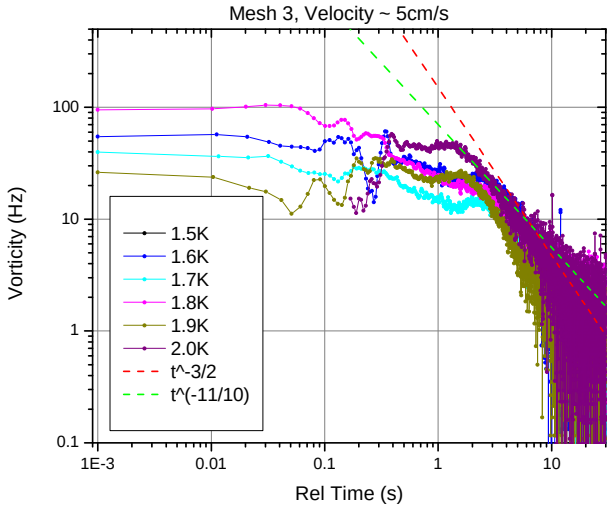

(a) Vorticity Plot

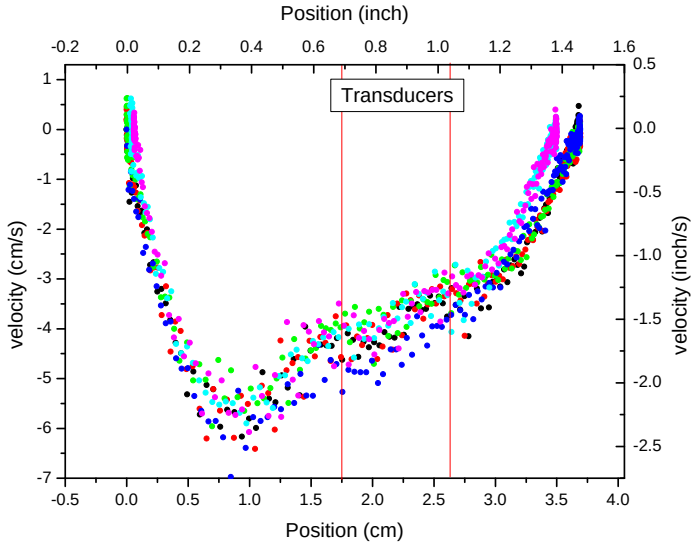

(b) Velocity vrs Position (JY)

Figure 5.25: Temperature comparison plot of the vorticity, and the corresponding velocity vrs position plot, for 1 minute wait times. Mesh 3, much slower velocity.

to reach saturation and exhibit a $t^{-3/2}$ power law dependency, regardless of initial vorticity. or vortex line density.

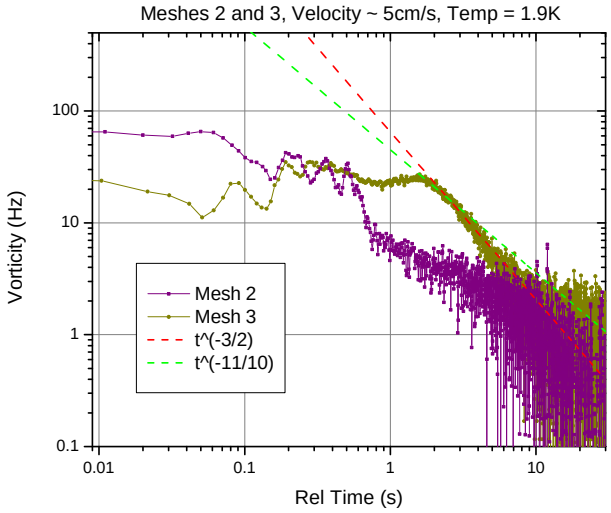

Figure 5.26: A plot showing the averaged vorticity for the two separate meshes achieved by the motor, at a slower velocity

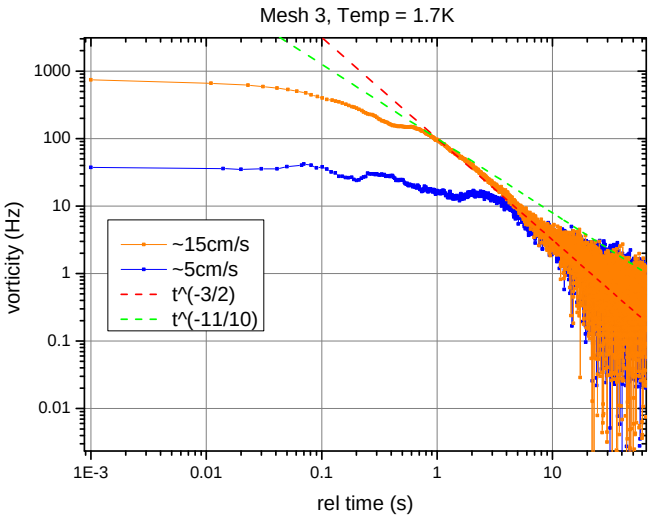

Figure 5.27: A plot showing the averaged vorticity for the two different speeds achieved by the motor, with mesh 3

5.3.3.1 Oscillations of Mesh 3

Other quantum grid turbulence experimental groups (Bradley [2011], Bradley *et al.* [2012], Nichol *et al.* [2004]) have used oscillating grids as opposed to 'single stroke' grids as presented in this dissertation. To determine if there is any difference in these two methods, a series of data sets were taken using an oscillating motion of the motor and grid. The grid (Mesh 3) was bought up to a certain position and oscillated, either just above, directly in-between, or just below the transducers, before being bought back down to the initial resting position. The peak to peak of these oscillations were the same for each set of data, and therefore so was the velocity.

Figure 5.28 shows a typical motor motion plot of position as a function of time, the grid oscillated around the centre of the transducers twice for this test.

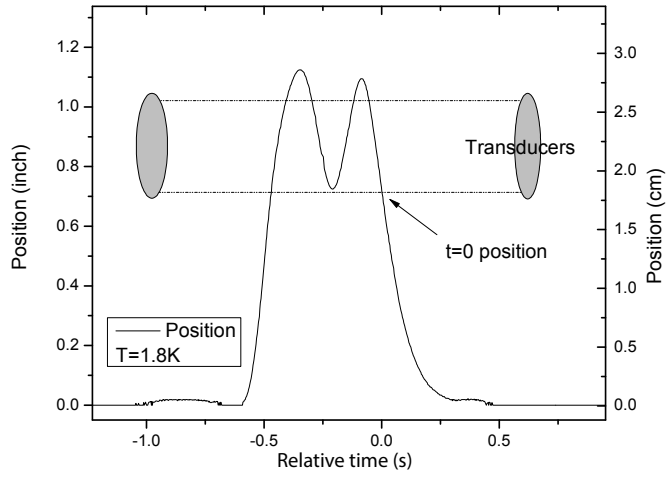

Figure 5.28: A typical position plot of '4 strokes' with transducer placement, with mesh 3. (JY)

Figure 5.29 shows three vorticity curves; 2, 4, and 6 strokes refer to the number of times the grid was swept past the centre of the transducers. This plot shows that an increased amount of oscillation does not change the vorticity, and therefore the vortex line density decay. Figure 5.30 compares three separate *4 stroke* oscillations, the oscillations were just above, centred around, and just below the transducers.

It is clear that oscillating just above and in-between the transducers does not have an effect on the vorticity curves. However the transition to the inertial range is observed at a later time from the turbulence produced by oscillating the grid beneath the transducers, as there was less observable turbulence at early times. These results show that there is a measurable small amount of turbulence being produced from the oscillations.

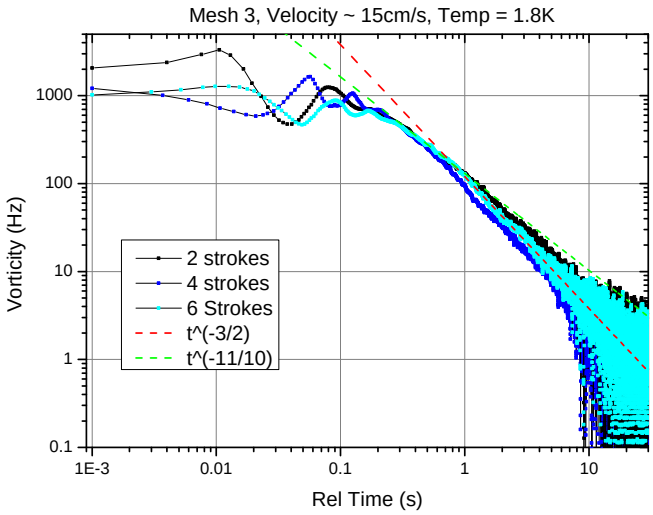

Figure 5.29: Comparison plot of vorticity for different numbers or motor strokes, with mesh 3. (JY)

It was observed that there is a slight difference between the turbulence produced from oscillations and the turbulence produced from single sweeps, as shown in figure 5.31. The saturation time is later, meaning that there is less turbulence initially produced in the single stroke data. Another interesting point to note from figures 5.29 and 5.30 are the oscillations in the vorticity before the saturation point. As the curves presented are averages, it goes without saying that the oscillations observed are measured in each separate data set.

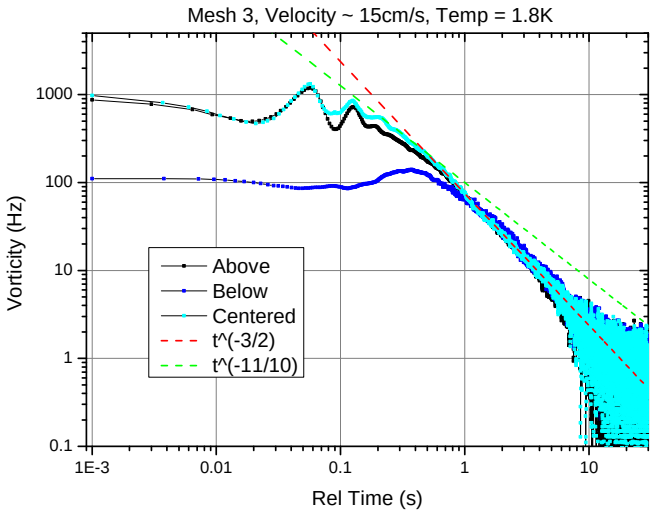

Figure 5.30: A plot comparing 2 stroke motor motions with different start positions, with mesh 3

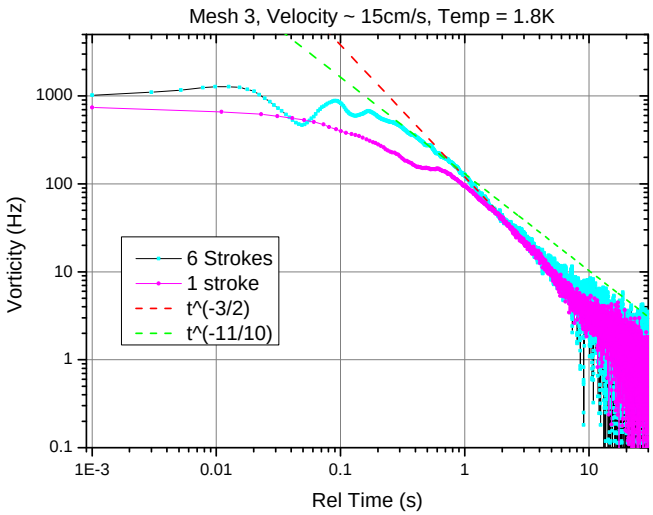

Figure 5.31: A plot comparing an oscillating motor motion with 1 sweep of the motor, with mesh 3. (LM+JY)

5.3.4 Discussion of all Grids

A direct comparison of all three meshes discussed in this chapter are presented in figure 5.32, this data was taken at 1.7 K with a motor velocity of approximately 15 cm/s. This plot shows all three meshes have the expected $t^{-3/2}$ power law dependency at late times; this agrees with the data published in Stalp [1998] for a similar (stated as 10 cm/s in the thesis) velocity.

Due to the inadequate data acquisition technique for any and all of the data recorded while using Mesh 1, no conclusions are made from the higher vortex line density at $t < t_{sat}$, seen in the top, black curve in figure 5.32 representing Mesh 1. The discernible difference between Mesh 2 and Mesh 3 is the amount of turbulence produced; Mesh 3 produced more turbulence at early times, and therefore the turbulence reached saturation more quickly than the turbulence produced from Mesh 2.

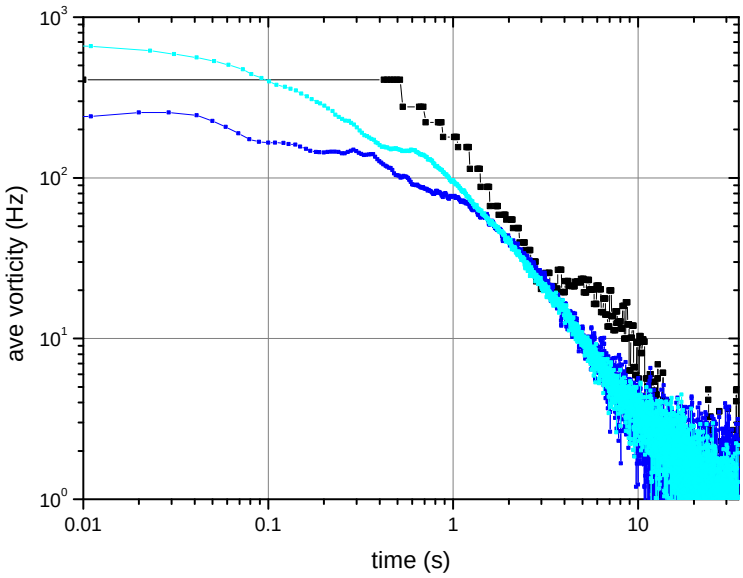

Figure 5.32: A plot comparing the three different grids used, taken at 1.7K and an average velocity of approximately 15cm/s

A classical grid turbulence experiment, Mohsen [1990], states a difference in the energy dissipation rate, $\epsilon = \nu\omega^2$, between mesh sizes. This publication shows

a smaller mesh size ($M = 2.54\,\text{cm}$ as opposed to $5.08\,\text{cm}$) has a higher energy dissipation rate. This agrees with the results presented in figure 5.32 as Mesh 3, the smaller mesh, has a higher initial vorticity.

Figure 5.33 shows a direct comparison between figure 5.32 and the data presented in Stalp [1998] and Stalp *et al.* [1999]. The black line (representing vorticity produced from a motion with a velocity of $10\,\text{cm/s}$), from the published paper, agrees with the data obtained form Mesh 2 vorticity, showing the exact same saturation time. Another noticeable, and important point is the earlier saturation time for Mesh 3.

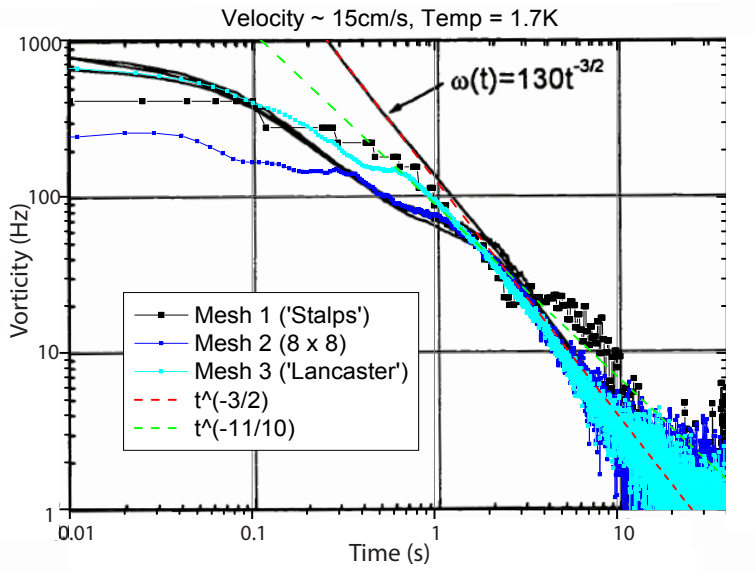

Figure 5.33: A plot comparing results from Stalp [1998] with all three meshes (shown in figure 5.32)Black lines are data from Stalp paper, square points are Mesh one, green small dots are Mesh 2, and blue small dots are Mesh 3.

The difference in the time duration for which the vorticity curves follow either power law dependencies is better illustrated in figures 5.34 and 5.35, representing Mesh 2 and Mesh 3, respectively. These plots have been drawn from rearranging equations 5.3 and 5.2, so that a straight line equation in the form $y = mx + c$:

$$\omega^{-2/3} = \omega_0^{-2/3} t + \omega_0^{-2/3} t^* \tag{5.4}$$

where $\omega_0 = \frac{D}{2\pi\sqrt{\nu'}}$, and similarly for $\omega^{-10/11}$.

Figures 5.34 and 5.35 do not show any real evidence for the $t^{-11/10}$ power law

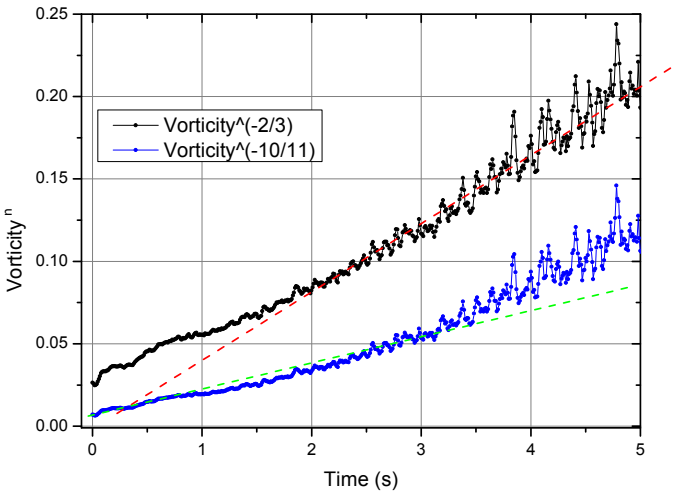

Figure 5.34: A plot showing the power law dependencies, taken at 1.7 K and an average velocity of approximately 15 cm/s, for Mesh 2.

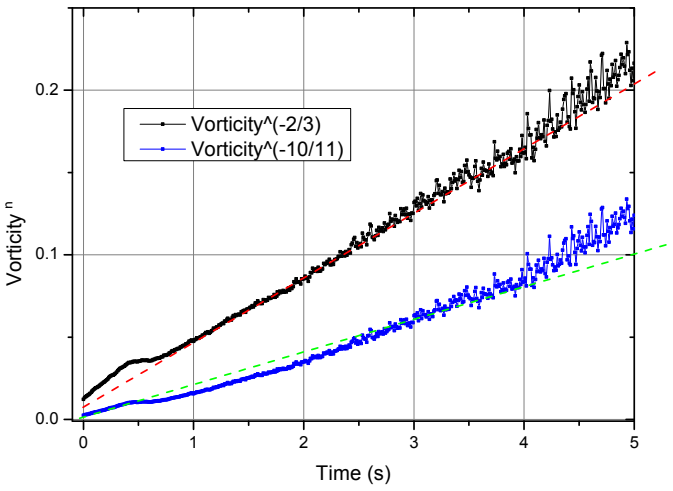

Figure 5.35: A plot showing the power law dependences, taken at 1.7K and an average velocity of approximately 15cm/s, for Mesh 3.

dependence.

The line density as a function of time can be written as:

$$L(t) = \omega/\kappa = \frac{D}{2\pi\kappa\sqrt{\nu'}}(3C)^{-3/2}(t+t^*)^{-3/2} \tag{5.5}$$

Figure 5.36 shows a typical vorticity curve (presented as line density), the pink curve fitted is the theoretical curve calculated from equation 5.5. From the parameters used for an appropriate fit to the late time region (the inertial region), the effective kinematic viscosity is recorded. The parameters are found through trial and error.

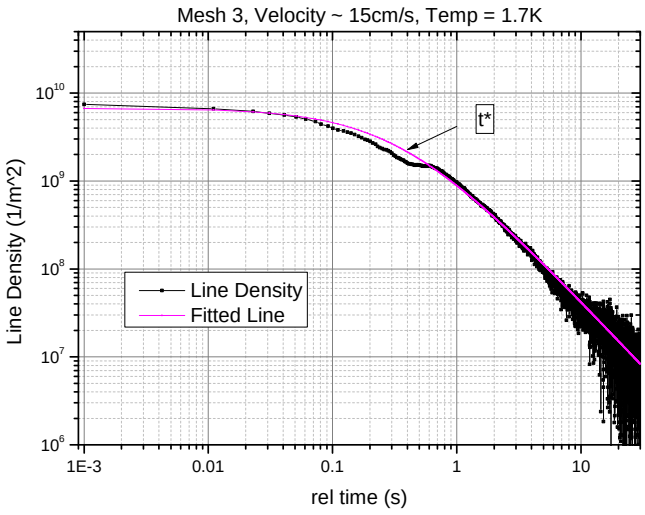

Figure 5.36: A plot showing a typical fitted line density curve to the data.

The effective kinematic viscosities, deduced from fitting the expected line density curve to each late time region of the vorticity curve presented in this chapter, are presented in figure 5.37. The black diamonds connected by straight black lines represent a model calculation for ν', Vinen & Niemela [2002]. The orange spheres represent values presented in Stalp & Niemela [2002]. The values obtained from the turbulence produced by Mesh 3 are lower than the effective kinematic viscosity values obtained from Mesh 2. This agrees with Niemela *et al.* [2005], who show that the values for ν', as a function of temperature, from a smaller mesh are slightly lower. Data presented in Chagovets *et al.* [2007] show similar results, with

a data range of a factor of 10; this agrees with the data range seen in figure 5.37.

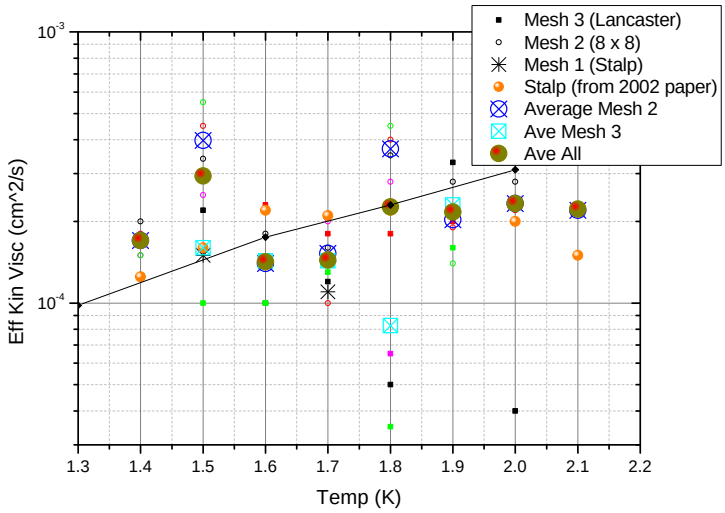

Figure 5.37: A plot comparing the effective kinematic viscosity, for all the three different grids used

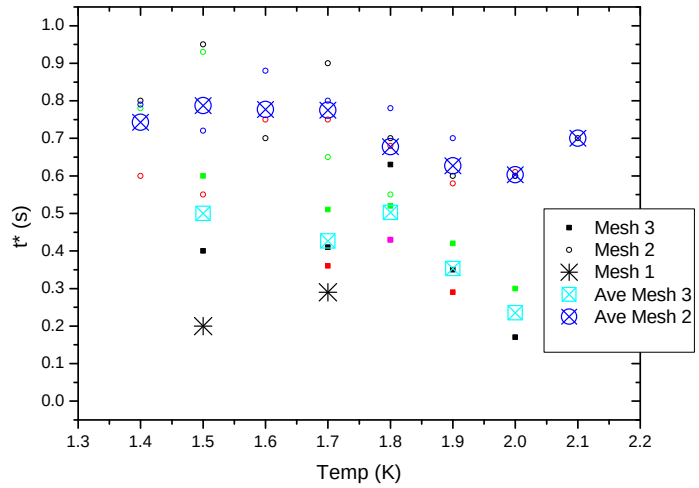

Figure 5.38: A plot comparing the saturation time, for all the three different grids used

Figure 5.38 shows the values of t^*. This data is deduced from the point in time when the vorticity curve veers from the expected late-time $t^{-3/2}$, by a factor of two. The value for the saturation time is not calculated from the fitted line, as shown in figure 5.36, as not all vorticity curves allowed for it, due to the inherent

error in the data. The reader is reminded that t^* represents the time taken needed for the turbulence to reach saturation at the size of the channel. As previously discussed, the results presented here are contrary to what would be expected from the Kolmogorov energy spectrum. This result may show that the growth of the energy containing length scale is quicker with a smaller mesh, and therefore more vortices at t_0.

Chapter 6

Summary

6.1 Low Frequency Turbulent Drag

Presented in chapter 3 are results from the use of an oscillating device Bradley *et al.* [2011], which are also presented in Bradley *et al.* [2012]. An oscillating grid, the 'floppy grid', was used investigate the velocity of a wire with respect to the fluid turbulent drag. The device was also used to investigate the dependence of oscillation frequency of the wire, on the resulting velocity.

It was found that there is no frequency dependence on the response of the floppy grid, over the range 9 to 100 Hz. This contradicts the relationship between critical velocity and frequency presented in Hänninen & Schoepe [2008]. The fact that there is no discernible dependence on frequency means that this device can be used to investigate quasi-static motion through superfluids at very low temperatures.

The drag coefficient, for oscillations within normal fluid and superfluid, as a function of grid velocity are also presented. It has been shown that, for the normal fluid, the fluid drag coefficient tends towards a constant of approximately 1.6. This value agrees with other work, using an oscillating cylinder, carried out in classical turbulence, for example Obasaju *et al.* [1988]; although no published work has been found which reports the use of an oscillating grid in a classical fluid.

Comparing the curves for drag coefficients, at high velocities, for quantum turbulence and classical turbulence shows that they are very similar. This indicates that the two types of turbulence are very similar, agreeing with work published by

Blazková *et al.* [2009], who used tuning fork resonators.

The measured critical velocity for the transition into the turbulent regime in superfluid at very low temperatures was found to be much smaller (3 mm/s) than the calculated value (17 mm/s). This is assumed to be due to the local superfluid flow around the edges of the grid, reducing the observed critical velocity, Bradley *et al.* [2012]. It would therefore be suggested to repeat these measurements in a more confined experimental cell, where the edges of the grid are constantly close to the cell walls.

The critical velocity is suggested to be frequency dependent, $v_c \approx \sqrt{8\kappa\omega}$, and the floppy wire and floppy grid both have very low resonant frequencies compared to most previous work (with wires with resonant frequencies of kHz order, Yano [2009] is one example). This may be a contributing factor to the apparent discrepancy in critical velocity. However, it has been presented in chapter 3 that, at low frequencies, the drag force is independent of frequency; this indicates that the relationship described in Hänninen & Schoepe [2008] is only appropriate at higher frequencies. It would therefore be very interesting to investigate the frequency regime between 100 and 1000 Hz, to determine when the critical velocity does indeed become frequency dependent.

Previous work using vibrating wires, for example Hashimoto & H. Yano [2007], have shown a jump from the laminar to turbulent regime in the velocity curve as a function of drag force. This jump was observed after warming, and subsequently cooling through the lambda transition. It has been attributed to vortices pinned to the vibrating wire caused by the transition into superfluid. It would therefore be interesting to investigate this phenomena with the floppy grid device; there may or may not be a dependence on whether or not a grid is present, as opposed to just a single wire. As there is more of a surface area for the vortices to be pinned to, it can be suggested that the jump from one regime to the other would be expected to be seen at a lower velocity. It would also be interesting to see if this effect is dependent on the frequency of the oscillating object.

6.2 Control Motor

Chapter 4 discusses a new design for a superconducting linear motor, for the purpose of producing homogeneous grid turbulence at very low temperatures. The inspiration for the control motor, the design process, and construction details are reported, along with test results shown in figures 4.14 and 4.15.

The linear motor is comprised of a drive coil, three control coils, two sets of quadrupole bearings, a position sensor, and a base plate: this is depicted in figure 4.1. The actuator, on which the motor acts, is constructed from two sections of niobium and a G-10 spacer; when the motor is not in operation the actuator rests on the base plate. The two sets of quadrupole bearing magnets are connected in series and are supplied with a constant current. The control coils are also connected in series and are supplied with a constant current; these were designed specifically to produce a constant gradient in the magnetic field over a set distance. A linear current profile is supplied to the drive coil, this results in the armature moving in the z-direction. The inductive position sensor is also detailed, which records the position of the motor with a 0.5 mm precision, once calibrated.

The test results show that the motor produces smooth motions, with little to no oscillations. The motor is reported to be able to travel with a peak velocity of approximately 30 cm/s. However, the velocity is not constant throughout the motion. This means that the turbulence produced is not likely to be homogeneous. To fix this problem, a current profile needs to be devised which takes into account the slow acceleration and deceleration periods. Zmeev [2014] show a unique method of deriving a current profile which compensates for these periods, hopefully resulting in quasi-constant velocity.

The motor was originally designed to be able to work at very low temperatures. Therefore the next stage for this equipment should be for it to be placed in a dilution refrigerator. For this to occur an attachment will have to be designed so that all of the coils are thermally isolated from the actuator, and more importantly the experimental cell.

6.3 Second-sound Attenuation

Presented in Chapter 5 are results of decaying turbulence as a function of time. The turbulence is intended to be approximately homogeneous and isotropic grid turbulence, and is produced by the linear control motor discussed in Chapter 4. The decay of the vorticity, or vortex line density, is recorded using the attenuation of second-sound. Similar experiments, focusing on the dependence of grid velocity, have been done before using a pulley driven linear motor: Stalp [1998], Smith *et al.* [1993], and Skrbek & Stalp [2000]. One of the main discussion points of this thesis is to determine if there is a dependence on the grid mesh used to produce the turbulence. Temperature dependence above 1.4 K has also been investigated.

It was expected that the smaller grid mesh will produce turbulence which will take a longer amount of time to reach saturation, as the energy containing vortices at zero time will be at a larger wavenumber. It is suggested by the results presented in this thesis, however, that the smaller grid mesh, Mesh 3, actually took a smaller amount of time to reach saturation, the $t^{-3/2}$ regime, than the larger grid meshes.

Figures 5.34 and 5.35 are presented to show how well the vorticity data fits to the power laws $t^{-3/2}$ and $t^{-11/10}$. It is clear from these plots that there is no evidence for the latter power law. The $t^{-3/2}$ regime is observed for both meshes, and as previously discussed, it is reached at an earlier time for Mesh 3. The representative temperature of the presented vorticity curves, 1.7 K, show the saturation time difference to be of the order of one second.

Mesh 1 was expected to produce approximately the same results as those presented in Stalp [1998], as the same grid mesh design and channel width were used, as well as similar speeds. The vorticity curve presented for Mesh 1 data, is representative of very preliminary data, and therefore not as accurate as the other meshes. It is unfortunate that no conclusions can be drawn from this data, it would be interesting to determine whether or not the difference between the design of the grid meshes 1 and 2 make a difference to the vorticity decay curve. The

classical turbulence experiments discussed in Mohsen [1990] show that there is no difference between turbulence produced by grids with different rod shapes as the mesh; though this data was taken in a wind tunnel.

The data taken using Mesh 1 should be re-taken, with the improvements made to the experimental set-up and procedure used for meshes 2 and 3. It would also be interesting to determine if other designs of a grid, but with the same mesh size, would result in a different line density decay. Mesh 2 is similar in mesh size, so a simple comparison with accurate data would yield some conclusions to this effect.

The vorticity decay plots presenting various temperatures from the turbulence produced by Mesh 2, as well as the similar plots shown for data achieved from the use of Mesh 3, all show that there is no temperature dependence of the vorticity decay curves. This agrees with data presented in Stalp [1998] and Chagovets *et al.* [2007]. This is to be expected while the fluid is still in the 2-fluid model regime, $1K < T < T_\lambda$. However below 1 K, the fluid is (almost) completely superfluid, and therefore the result may differ. Data presented in Walmsley *et al.* [2007] shows a clearer and more defined inertial regime at lower temperatures; Ahlstrom *et al.* [2013] presents data showing the transition from laminar to turbulent flow at different temperatures, depicting a drastic difference at temperatures below 0.5 K. However, these other experiments were done using tuning forks (Ahlstrom *et al.* [2013]) and turbulence produced from a spin down in a rotating cryostat (Walmsley *et al.* [2007]).

There are many other processes in which to observe the decay of turbulence at the zero temperature limit, where the use of second-sound is no longer an option (for example - Fisher *et al.* [2001], Guo *et al.* [2010]). Therefore, an investigation into the temperature dependence over a larger range should be performed, with particular interest on the temperature where the fluid becomes pure superfluid.

It was also found that the SS resonance peak chosen, the peak to peak voltage of which is continuously recorded to determine the attenuation, does not have an affect on the vorticity decay curve. This is as expected, as the vorticity equation

is dependant on Δ_0, not the frequency of the SS.

There is an unexplained spread in the data presented in chapter 5. There are a number of possible reasons for this: the non-constant velocity of the grid, the feedback circuit being operated in the non-linear region, variations in the electrical circuitry and home-made electrical boxes, interference from outside which differs depending on the time of the day, or another reason which has not yet been considered. More precisely, unknown initial conditions can, and will, cause differences in the turbulence generating processes. All of these possible problems need to be investigated and either eliminated or solved before any further tests are carried out.

To better study these inconsistencies, it is imperative that the velocity of the motor, and grid, be constant. The inconstant nature of the velocity means that the turbulence produced is not necessarily homogeneous and isotropic. It is unclear as to how this will effect the decay of the turbulence. Though the late-time decay should still follow a $t^{-3/2}$ dependence, the saturation time may be affected. This is evident in the spread of t^* values presented in figure 5.38.

The spread in the vorticity data may, of course, be real and a physical aspect of the turbulence or fluid. It is assumed that the $t^{-3/2}$ regime begins once the energy containing vortices reach saturation, at the size of the channel. However, this assumption may not be right; it is very possible that there are other, unknown mechanisms in play in the fluid that are, as of yet, not understood. A way of testing this is to change the channel size. If there were a large channel, and very small mesh holes, then the turbulence may never, theoretically, reach saturation; in which case a $t^{-3/2}$ regime should not be observed. An experiment to test this theory is, at the time of print, being designed at the University of Florida.

At early times in almost all vorticity plots, for all three meshes, an inconsistent oscillation can be seen. One explanation for this would be the fluctuations in temperature immediately following a motor movement. As the motor coils are submerged in the same fluid as the experimental cell, when current is passed

through them there is a heat leak; this heat rise is then compensated for by the temperature regulation circuit. This compensation, however, is not instantaneous. Another possible explanation is the feedback circuit not running at the optimum settings. At the time of print, the feedback circuit described in this thesis is being investigated and improved, and so future experiments will show if this is the case.

At time t_0 it is believed that the energy containing vortices are at the size of the mesh holes, and the energy containing scale shifts towards the larger length scales over time, saturating at the size of the channel. This suggests that if the injection scale is small (the mesh size is small), then it would take longer for the energy containing vortices to reach saturation, resulting in a longer period of time for the decaying vorticity to reach the $t^{-3/2}$ regime. The opposite is observed in the measurements presented, as shown in the comparison plot including all three meshes and the saturation time plot.

The reason for this apparent contradiction could be due to a number of things, one of which is the possible errors in the experiment suggested earlier. One other problem, which could cause this, is large scale turbulence being produced around the outside of the grid, between the grid and the inside of the channel walls. The large scale turbulence may contain the energy containing vortices, and therefore would take less time to saturate at the size of the channel. However, the gap between the grid mesh and the channel walls was the same for both Mesh 2 and Mesh 3, so this may not be the solution otherwise it would have the same effect on both meshes, which is does not. Therefore if this is a problem, it is clear it is not the only one.

Another possibility for the disparity observed, however, is the fact that there are unknown factors which cause the saturation of turbulence other than the size of the channel. This would also explain the spread in the effective kinematic viscosity values, presented in figure 5.37. These unknown factors cannot be initial conditions that have been unchanged in the experiments discussed in chapter 5, like the mesh size, the channel wall roughness, or the consistency of the velocity.

Appdx A

Technical Drawings Found below are the technical drawings for the channel (figures 2(a) and 2(b)), channel caps (figure 1) and the extension rod (figure 3). Also presented is the technical design for the Teflon holder which was used to hold the extension rod and grid in the right positions for construction (figure 4).

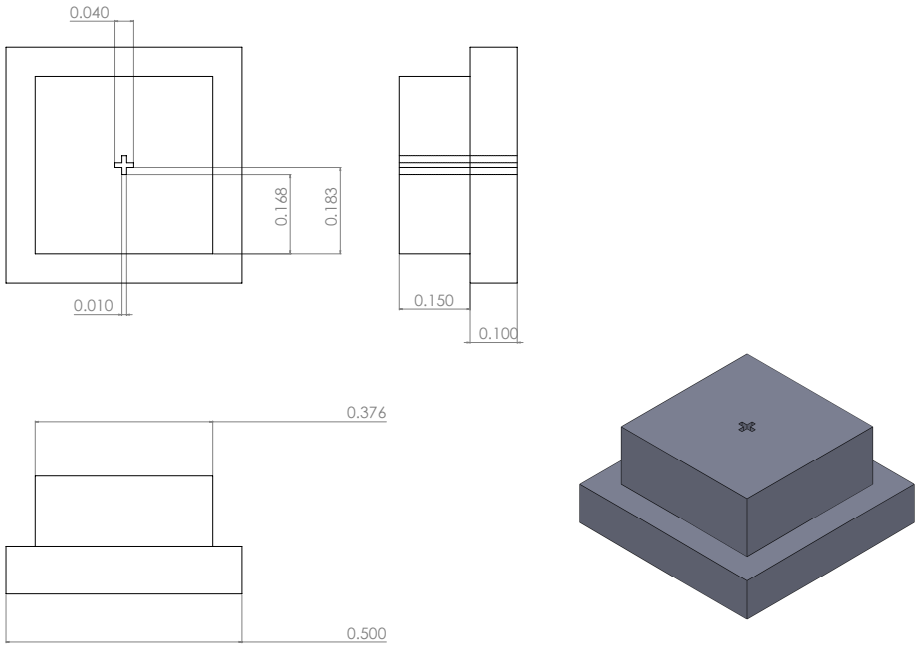

Figure 1: SolidWorks drawing for the bottom cap with a cross-shaped hole for the latest extension rod.

All dimensions are in inches.

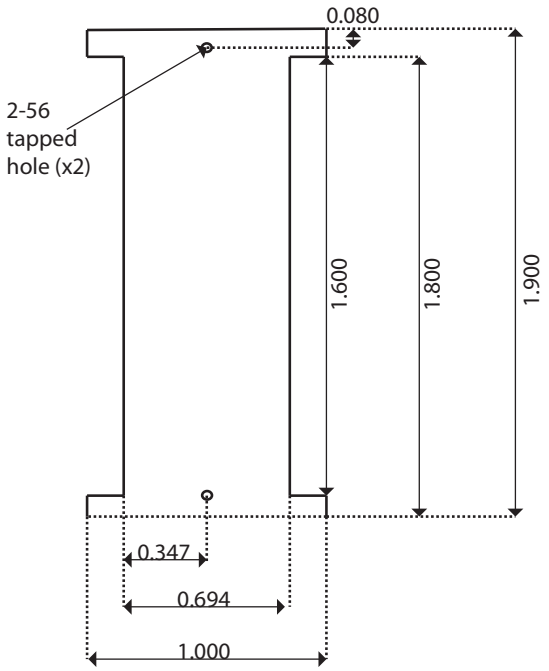

(a) Side view of the Channel

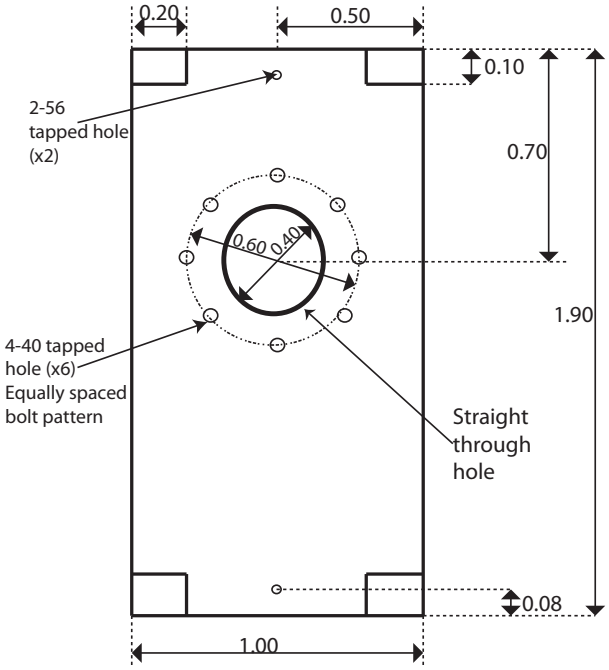

(b) Front/Back view of the Channel

Figure 2: Schematic drawings for the channel
There is a 1cm cross-sectional hole through the centre, from top to bottom; this is the experimental volume. All dimensions are in inches.

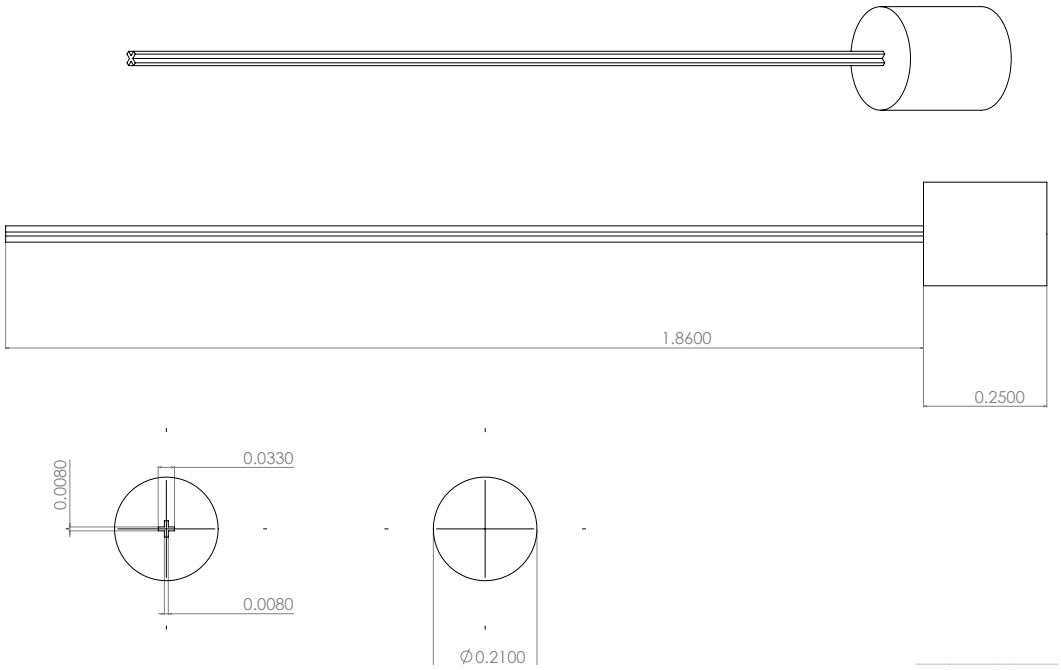

Figure 3: SolidWorks drawing for the cross shaped extension rod. All dimensions are in inches.

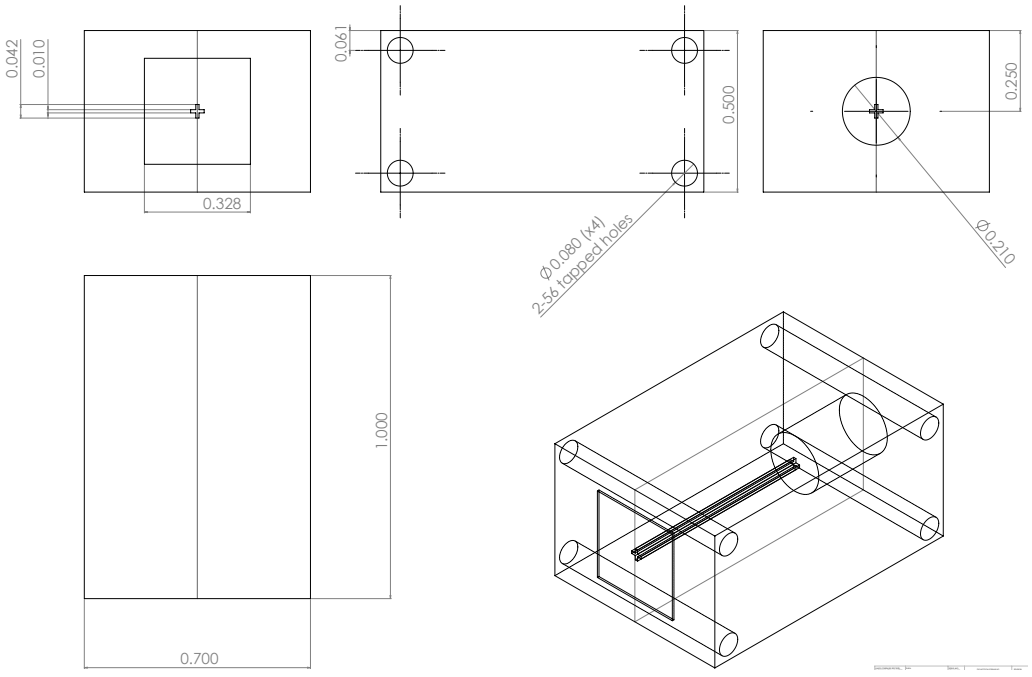

Figure 4: SolidWorks drawing for the Teflon aligning and levelling device. This was made and used to ensure the extension rod was perfectly in line with the actuator, and the grid was perpendicular to the extension rod. All dimensions are in inches.

References

Ahlstrom, S., Bradley, D.I., Človečko, M., Fisher, S.N., Guise, E., Haley, R.P., Kolosov, O., McClintock, P., Pickett, G.R., Poole, M., Tsepelin, V. & Woods, A. (2013). Frequency dependent drag from quantum turbulence produced by quartz tuning forks in superfluid ^{4}He. *Phys Rev Lett B*, **111**, 111. 26, 104

Bardeen, J., Cooper, L.N. & Schrieffer, J.R. (1957). Theory of superconductivity. *Phys. Rev.*, **108**, 1175–1204. 19

Batchelor, G.K. (1953). *The Theory of Homogeneous Turbulence*. Cambridge university press. 12

Batchelor, G.K. & Proudman, I. (1956). The large-scale structure of homogeneous turbulence. *Philosophical Transactions of the Royal Society of London. Series A, Mathematical and Physical Sciences*, **248**, 369–405. 13

Bennemann, K. & Ketterson, J. (2013). *Novel Superfluids*. Oxford Science Publications. 14

Berent, I. & Polturak, E. (1998). Critical behavior of the shear resistance of solid helium near a structural phase transition. *Phys. Rev. Lett.*, **81**, 846–849. 26

Blažková, M., Schmoranzer, D. & Skrbek, L. (2007). Transition from laminar to turbulent drag in flow due to a vibrating quartz fork. *Phys. Rev. E*, **75**, 025302. 26

Blazková, M., Schmoranzer, D., Skrbek, L. & Vinen, W. (2009). Generation of turbulence by vibrating forks and other structures in superfluid ^{4}He. *Physical Review B*, **79**, 54522. 101

Bradley, D., Fisher, S., Guenault, A., Haley, R., Kumar, M., Lawson, C., Schanen, R., McClintock, P., Munday, L., Pickett, G., Poole, M., Tseplin, V. & Williams, P. (2012). Turbulent drag on a low-frequency vibrating grid in superfluid ^{4}He at very low temperatures. *Phys Rev Lett*, **85**, 1–10. 29, 33, 37, 41, 91, 100, 101

Bradley, D.e.a. (2011). Direct measurement of the energy dissipated by quantum turbulence. *Nature Physics Letters*, **7**, 473–476. 91

Bradley, D.I., Clubb, D.O., Fisher, S.N., Guénault, A.M., Haley, R.P., Matthews, C.J., Pickett, G.R. & Zaki, K.L. (2005). Turbulence generated by vibrating wire resonators in superfluid ^{4}He at low temperatures. *J. Low Temp. Phys.*, **138**, 493–498. 2, 26

Bradley, D.I., Fear, M.J., Fisher, S.N., Guénault, A.M., Haley, R.P., Lawson, C.R., McClintock, P.V.E., Pickett, G.R., Schanen, R., Tsepelin, V. & Wheatland, L.A. (2009). Transition to turbulence for a quartz tuning fork in superfluid ^{4}He. *J. Low. Temp. Phys.*, **156**, 116–131. 36

Bradley, D.I., Človečko, M., Fear, M.J., Fisher, S.N., Guénault, A.M., Haley, R.P., Lawson, C.R., Pickett, G.R., Schanen, R., Tsepelin, V. & Williams, P. (2011). A new device for studying low or zero frequency mechanical motion at very low temperatures. *J. Low Temp. Phys.*, **165**, 114. 2, 26, 41, 100

Chagovets, T., Gordeev, A. & Skrbek, L. (2007). Effective kinematic viscosity of turbulent He II. *Phys Rev Lett*, **76**, 1–4. 25, 76, 81, 97, 104

Charalambous, D., Skrbek, L., Hendry, P.C., McClintock, P.V.E. & Vinen, W.F. (2006). Experimental investigation of the dynamics of a vibrating

grid in superfluid ^{4}He over a range of temperatures and pressures. *Phys. Rev. E*, **74**, 036307. 2

Cooper, L.N. (1956). Bound electron pairs in a degenerate fermi gas. *Phys. Rev.*, **104**, 1189–1190. 19

Couder, Y. (1984). Two-dimensional grid turbulence in a thin liquid film. *Journal de Physique Lettres*, **45**, 353–360. 2

Donnelly, R. & Barenghi, C. (1998). The observed properties of liquid helium at the saturated vapor pressure. Internet Web Page. 75

Elmegreen, B.G. & Scalo, J. (2004). Interstellar turbulence I: Observations and processes. *arXiv preprint astro-ph/0404451*. 1

Enss, C. & Hunklinger, S. (2005). *Low Temperature Physics*. Springer US. 4, 5, 10, 21

Feynman, R.P. (1955). Application of quantum mechanics to liquid helium. *Progress in Low Temperature Physics*, **I**, Chapter 2. 8

Fisher, S.N., Hale, A.J., Guénault, A.M. & Pickett, G.R. (2001). Generation and detection of quantum turbulence in superfluid. *Phys. Rev. Lett.*, **86**, 244–247. 104

Giltrow, M., Charalambous, D. & McClintock, P. (2009). Initial studies of a linear motor for generating quantum turbulence in He-II with a drawn grid. In *Journal of Physics: Conference Series*, vol. 150, 012014, IOP Publishing. 43

Guo, W., Cahn, S.B., Nikkel, J.A., Vinen, W.F. & McKinsey, D.N. (2010). Visualization study of counterflow in superfluid. *Phys. Rev. Lett.*, **105**, 045301. 104

Hall, H.E. & Vinen, W.F. (1956). The rotation of liquid helium II. 1. experiments on the propagation of second sound in uniformly rotating helium II. *Proc. Roy. Soc. (Lond.) A*, **238**, 204–214. 25

Hänninen, R. & Schoepe, W. (2008). Frequency dependence of the critical velocity of a sphere oscillating in superfluid helium-4. *arXiv:0801.2521 [cond-mat.other]*. 38, 100, 101

Hanson, W. & Pellam, J. (1954). Second sound attenuation in liquid helium II. *Phys Rev Lett*, **95**, 321–327. 22, 23

Hashimoto, N. & H. Yano, e.a. (2007). Control of turbulence in boundary layers of superfluid ^{4}He by filtering out remnant vortices. *Physical Review B*, **76**, 1–4. 101

Heikkila, W. & Hallet, A.H. (1955). The viscosity of liquid helium II. *Can. J. Phys.*, **33**, 420–435. 7

Hideharu, M. (1991). Realization of a large-scale turbulence field in a small wind tunnel. *Fluid Dynamics Research*, **8**, 53. 41

Hook, J. & Hall, H. (1991). *Solid State Physics*. John Wiley and Sons, 2nd edn. 20

Ihas, G.G., Labbe, G., Liu, S.C. & Thompson, K.J. (2008). Preliminary measurement on grid turbulence in liquid ^{4}He. *J. Low Temp. Phys.*, **150**, 384–393. 3

Kapitza, P. (1938). Viscosity of liquid helium below the λ-point. *Nature*, **141**, 74. 6

Koplik, J. & Levine, H. (1993). Vortex reconnection in superfluid helium. *Physical review letters*, **71**, 1375. 14

Kozik, E. & Svistunov, B. (2004). Kelvin-wave cascade and decay of superfluid turbulence. *Phys. Rev. Lett.*, **92**, 035301. 15

Krogstad, P.Å. & Davidson, P. (2009). Is grid turbulence saffman turbulence? *J. Fluid Mech.*, **642**, 373–394. 13

Leadbeater, M., Winiecki, T., Samuels, D., Barenghi, C. & Adams, C. (2001). Sound emission due to superfluid vortex reconnections. *Phys. Rev. Lett.*, **86**, 1410. 15

Liu, S., Labbe, G. & Ihas, G.G. (2006). Shiegrid superconducting linear motor for towed-grid studies of quantum turbulence. *J. Low Temp .Phys.*, **145**, 165–185. 43, 59

Liu, S., Labbe, G. & Ihas, G. (2007). Producing towed grid quantum turbulence in liquid ^{4}He. *J. Low Temp. Phys.*, **148**, 281–285. 3

London, H., Clarke, G. & Mendoza, E. (1962). Osmotic pressure of ^{3}He in liquid ^{4}He, with proposals for a refrigerator to work below 1K. *Phys Rev Lett*, **128**, 1992–2003. 16

Lounasmaa, O. (1974). *Experimental Principles and Methods Below* 1 K. Academic Press London and New York. 17, 18

Luzuriaga, J. (1997). Measurements in the laminar and turbulent regime of superfluid ^{4}He by means of an oscillating sphere. *J. Low Temp. Phys*, **108**, 267–277. 2

Millman, J. & Halkias, C.C. (1972). *Integrated Electronics: Analog and Digital Circuits and Systems*. Tata McGraw-Hill Education. 69

Mohsen, S. (1990). The decay power law in grid-generated turbulence. *J. Fluid Mech*, **219**, 195–214. 94, 104

Morison, J., Johnson, J., Schaaf, S. *et al.* (1950). The force exerted by surface waves on piles. *Journal of Petroleum Technology*, **2**, 149–154. 30

Mydlarski, L. & Warhaft, Z. (1996). On the onset of high-reynolds-number grid-generated wind tunnel turbulence. *J. Fluid Mech.*, **320**, 331–368. 2

Nichol, H.A., Skrbek, L., Hendry, P.C. & McClintock, P.V.E. (2004). Flow of He II due to an oscillating grid in the low-temperature limit. *Phys. Rev. Lett.*, **92**, 244501. 2, 91

Niemela, J.J., Sreenivasan, K.R. & R.J.Donnelly (2005). Grid generated turbulence in Helium II. *J. Low Temp. Phys.*, **138**, 537–542. 3, 97

Obasaju, E., Bearman, P. & Graham, J. (1988). A study of forces, circulation and vortex patterns around a circular cylinder in oscillating flow. *J. Fluid Mech.*, **196**, 467–494. 100

Roach, P. (1986). The generation of nearly isotropic turbulence by means of grids. *Heat and Fluid Flow*, 82–92. 2, 41

Saffman, P. (1967). The large-scale structure of homogeneous turbulence. *J. Fluid Mech.*, **27**, 581–593. 13

Schoepe, W. (2004). Fluctuations and stability of superfluid turbulence at mk temperatures. *Phys. Rev. Lett.*, **92**, 095301. 34

Sherlock, R. & Edwards, D. (2003). Oscillating superleak second sound transducers. *Rev. Sci. Instrum.*, **41**, 1603–1609. 60

Skrbek, L. & Stalp, S.R. (2000). On the decay of homogeneous isotropic turbulence. *Phys. Fluids*, **12**, 1997–2019. 76, 103

Skrbek, L., Niemela, J.J. & Donnelly, R.J. (2000). Four regimes of decaying grid turbulence in a finite channel. *Phys. Rev. Lett.*, **85**, 2973–2976. 76, 77, 81

Smith, M.R., Donnelly, R.J., Goldenfeld, N. & Vinen, W.F. (1993). Decay of vorticity in homogeneous turbulence. *Phys. Rev. Lett.*, **71**, 2583–2586. 3, 77, 103

Sreenivasan, K.R. (1995). On the universality of the kolmogorov constant. *Phys. Fluids*, **7**, 2778–2784. 13

Sreenivasan, K.R. (1999). Fluid turbulence. *Reviews of Modern Physics*, **71**, S383. 1

Stalp, S. (1998). *Decay of Grid Turbulence in Superfluid Helium*. Ph.D. thesis, University of Oregon. xiv, 3, 23, 42, 62, 76, 77, 81, 94, 95, 103, 104

Stalp, S. & Niemela, J.J. (2002). Dissipation of grid turbulence in helium II. *Phys. Fluids*, **14**, 1377–1379. 77, 97

Stalp, S.R., Skrbek, L. & Donnelly, R.J. (1999). Decay of grid turbulence in a finite channel. *Phys. Rev. Lett.*, **82**, 4831–4834. 3, 78, 95

Thompson, K.J. (2012). *Energy Decay in Superfluid Helium 4*. Ph.D. thesis, University of Florida. xi, 43, 45, 47, 55, 59

Tilley, D. & Tilley, J. (1974). *Superfluidity and Superconductivity*. Van Nostrand Reinhold Company. 19, 22

Vinen, W. (1961). The detection of single quanta of circulation in liquid helium II. *Proc. Roy. Soc. (Lond.) A*, **260**, 218–236. 9

Vinen, W. & Donnelly, R. (2007). Quantum turbulence. *Physics Today*, 43–48. 76

Vinen, W. & Niemela, J.J. (2002). Quantum turbulence. *J. Low Temp. Phys.*, **128**, 167–231. 11, 97

Walmsley, P., Golov, A., Hall, H., Levchenko, A. & Vinen, W. (2007). Dissipation of quantum turbulence in the zero temperature limit. *Phys. Rev. Lett.*, **99**, 265302. 104

Yang, J., Ekdahl, D., Munday, L. & Ihas, G. (2014). Heater for safe warming in low temperature experiments. 67

Yano, H.e.a. (2005). Observation of laminar and turbulent flow in superfluid ^{4}He using a vibrating wire. *J. Low Temp. Phys.*, **138**, 561–566. 41

Yano, H.e.a. (2009). Transition to quantum turbulence by thin vibrating wires in superfluid ^{4}He. *J. Low Temp. Phys.*, **156**, 132–144. 26, 101

Zmeev, D. (2014). A method for driving an oscillator at a quasi-uniform velocity. *Journal of Low Temperature Physics*, **175**, 480–485. 102